Local to Global: Galaxy Evolution across Spatial Scales

By

Cressida Cleland

A thesis submitted to
the University of Birmingham
for the degree of
DOCTOR OF PHILOSOPHY



Astronomy and Space Research group
School of Physics and Astronomy
College of Engineering and Physical Sciences
University of Birmingham
June 2023

UNIVERSITY OF
BIRMINGHAM

University of Birmingham Research Archive

e-theses repository

This unpublished thesis/dissertation is copyright of the author and/or third parties. The intellectual property rights of the author or third parties in respect of this work are as defined by The Copyright Designs and Patents Act 1988 or as modified by any successor legislation.

Any use made of information contained in this thesis/dissertation must be in accordance with that legislation and must be properly acknowledged. Further distribution or reproduction in any format is prohibited without the permission of the copyright holder.

ABSTRACT

It has been the aim of astronomers for the past century to understand the workings and evolution of galaxies. In particular, the transformative processes that take place in order to turn a galaxy from 'alive' to 'dead' have been an exciting topic of active research. It is now understood that galaxies are broadly split into two classes, blue spirals and red ellipticals (and lenticulars), featuring great differences in their properties. The mechanisms that move galaxies from blue to red (or spiral to elliptical) are referred to as quenching mechanisms. The region of parameter space through which a galaxy moves as it quenches is sometimes referred to as the 'green valley'. This thesis summarises the state of the field and then presents three novel studies on topics related to quenching mechanisms and galaxy evolution: environmental quenching, active galactic nucleus feedback, and superluminous supernova host galaxies.

These studies each find interesting and compelling results, and evidence of galaxies in the green valley. In the first, I found that the star-forming/quenched status of a satellite galaxy depends significantly on its stellar mass, the mass of its group halo, and its position within the group halo. The second study found evidence of young active galactic nuclei within star-forming galaxies and illustrated a scenario where variability of the active galactic nucleus has a profound effect on the lifecycle of the galaxy. In the third study, I investigated the environments of host galaxies of superluminous supernovae. I used simulations to explore the metallicities and star-formation rates, and environments, of similar galaxies and found that low metallicity is more important for the production of these explosive transients.

ACKNOWLEDGMENTS

This thesis is the product of nearly four years of learning, hard work, and growth. I have not achieved this on my own; I have many people to thank. They say 'it takes a village', and truly, I have found myself in an incredibly kind and supportive community. My supervisor, Dr. Sean McGee, has not only been a source of knowledge, guidance, and encouragement, but also friendship. Dr. Matteo Bianconi and Dr. Matt Nicholl have been great mentors and have helped foster the beginnings of my career. Dr. Ben Gompertz, Dr. Sam Oates, Dr. Graham Smith and Dr. Clément Bonnerot have taught me a lot about their respective fields of extragalactic astronomy, while providing me with their thoughts and advice at the weekly EG (pronounced 'egg') meeting. For all this and more, I thank all the above.

I will surely miss the postgraduate offices, G26 and G27, and everyone in them. For the years of friendship and memories, pub trips, parties, board game nights, brunch trips, barbecues, dinner parties, coffee breaks, 'fun' lunches, pub quizzes – you get the idea – I thank, Daria, Evan, Shola, Xinyue, Paige, Diganta, Eliot, Matt, Natalie, Roo, Alice. Special shout out to Aysha, Alex, Lucy S and Tom. You guys never fail to make me cry laughing, and I can't wait to see where the future brings you all. I must thank Dan and Luce, for being my rocks since the very beginning. This whole process has been made easier with these guys by my side, keeping me sane. I look forward to Paris - Portsmouth - Pasadena round trips! I particularly thank Dan, for always being there for me, and for being my biggest cheerleader in this final stretch. Onto the next chapter!

For always encouraging me in my interests, and believing in me, I thank my family: my mam, Laura, my step-dad, Morgan, my Granny and Michael, and all my aunts, uncles, and cousins. Thank you also to all my friends back in Dublin.

Tomorrow when the farm boys find this
freak of nature, they will wrap his body
in newspaper and carry him to the museum.
But tonight he is alive and in the north
field with his mother. It is a perfect
summer evening: the moon rising over
the orchard, the wind in the grass. And
as he stares into the sky, there are
twice as many stars as usual.

Two-Headed Calf, by Laura Gilpin

Contents

Page

1 Introduction **1**

1.1 Characteristics of galaxies 3

1.1.1 Morphology 3

1.1.2 Gas and star-formation in star-forming galaxies 5

1.2 Late-stage evolution: quenching 10

1.2.1 Internal mechanisms: Supernova feedback 14

1.2.2 Internal mechanisms: AGN feedback 15

1.2.3 External mechanisms: In-falling galaxies 18

1.2.4 External mechanisms: Mergers 22

1.3 Superluminous supernovae 27

1.3.1 Classification 27

1.3.2 Possible energy sources 28

1.3.3 Rates of SLSNe 30

1.3.4 Host galaxy properties 30

1.3.5 Links with gamma-ray bursts 31

1.4 Outline of thesis 32

2 Environmental galaxy quenching **33**

2.1 Introduction 34

2.2 Data 38

2.3 Results . . . 41
2.3.1 Quenched galaxies . . . 41
2.3.2 RQ galaxies . . . 44
2.3.3 Group and satellite properties . . . 50
2.3.4 Rejuvenating galaxies . . . 53
2.4 Discussion . . . 58
2.5 Conclusions . . . 63

Appendices **65**

2.A Dust Attenuation . . . 65

3 AGN variability **72**

3.1 Introduction . . . 73
3.2 Data . . . 74
3.3 Analysis and Results . . . 77
3.3.1 Calculating variability . . . 77
3.3.2 Variability and galaxy properties . . . 82
3.4 Discussion . . . 84
3.4.1 Source of the variability . . . 89
3.4.2 Implications for galaxy formation if variability is from AGN . . . 91
3.5 Conclusions . . . 93

Appendices **95**

3.A Simulations of recovered variability . . . 95

4 Superluminous supernova host galaxies **99**

4.1 Introduction . . . 100
4.2 Data . . . 104
4.2.1 Matched sample generation . . . 105

4.3 Results and discussion 107
4.3.1 Observations 107
4.3.2 Simulations 111
4.3.3 IllustrisTNG 111
4.4 Conclusions 115

Appendices **117**

4.A List of SLSNe 117

5 Conclusions **120**

References **123**

List of Figures

1.1 Some examples of the morphologies of galaxies. 2

1.2 Distribution of galaxies on the SFR-M_* plane, showing how the HI fraction changes along the MS. The MS is plotted as a dashed line, with dotted lines showing the 0.4 dex scatter about the MS. Shaded contours show the entire SDSS sample at $0.02 < z < 0.05$; black dots are galaxies with gas fractions below the xCOLD GASS detection limit; coloured circles show the HI gas fractions of galaxies colour-coded on a logscale. Figure adapted from Saintonge et al. (2017). 9

1.3 The distribution of SDSS galaxies at $z < 0.2$ with $u - r$ colour against stellar mass. The red sequence is shown, with redder colour and higher stellar mass. The blue cloud, however, is populated by bluer galaxies and galaxies with lower stellar mass. The green valley is the less densely populated region between the red sequence and the blue cloud. Contours connect bins that contain the same number of galaxies, as indicated by the z-axis. Outside the lowest contour level, grey dots show individual galaxies. 11

1.4 A histogram of the specific star-formation rate, sSFR, of SDSS galaxies. Two peaks are clearly visible, corresponding to the star-forming population and the quenched population. The region between the two peaks corresponds to a transitionary phase of galaxy evolution, sometimes referred to as the 'green valley'. 13

1.5 Some examples of merging galaxies. 24

2.1 Stellar mass (M_*) versus specific star-formation rate [a) $\mathrm{sSFR}_{\mathrm{H}\alpha}$; b) $\mathrm{sSFR}_{\mathrm{UV}}$] distributions for all galaxies. Note the bimodality of the population: star-forming in the top portion of each panel and quenched in the bottom portion of each panel. The z-axis denotes number of galaxies in each bin, with contour lines indicating regions of equal numbers. The light purple regions signify no data. 41

2.2 Stellar mass ($M*$) versus specific star-formation rate ($\mathrm{sSFR}_{\mathrm{H}\alpha}$) distributions for a) central galaxies and b) satellite galaxies. The grey dashed line signifies a) $\mathrm{sSFR}_{\mathrm{H}\alpha} = 10^{-11.7}$ yr^{-1} and b) $\mathrm{sSFR}_{\mathrm{UV}} = 10^{-11.1}$ yr^{-1}. The z-axis denotes number of galaxies in each bin, with contour lines indicating regions of equal numbers. The light purple regions signify no data. 43

2.3 Fraction of quenched galaxies, $f_{\mathrm{q}} = N_{\mathrm{q}}/N$, where N_{q} is the number of quenched central(satellite) galaxies and N is the total number of central(satellite) galaxies. The star-formation rate is drawn from Hα. 45

2.4 Distribution of equivalent widths of Hα measurements in angstroms. The black dashed line denotes EW(Hα) = 3Å. 46

2.5 Fraction of RQ galaxies, $f_{\mathrm{t}} = N_{\mathrm{t}}/N$, where N_{t} is the number of RQ central(satellite) galaxies and N is the total number of central(satellite) galaxies. RQ galaxies are those with no detectable Hα and UV emission from star-formation. 48

2.6 Colour magnitude diagram, $u - r$ against M_r. Contour plots indicate abundances of quenched and star-forming populations defined as above using $\mathrm{sSFR}_{\mathrm{H}\alpha}$. A marginalised distribution shows that RQ galaxies as defined in this paper lie between red and blue galaxies on a colour magnitude diagram. 49

2.7 Phase space histogram showing r/r_{180} and $\Delta v/\sigma$ for all galaxies, with marginalised distributions on each axis for star-forming, quenched and RQ galaxies. Note the similarity in distributions between RQ, quenched, and star-forming galaxies. The z-axis denotes number of galaxies in each bin. 51

2.8 Fractions of RQ galaxies with respect to star-forming galaxies (top) and quenched galaxies (bottom) for different group halo mass bins. There is a clear downward trend for the fraction of RQ galaxies with respect to star-forming galaxies as r/r_{180} increases at high halo mass. 52

2.9 BPT diagram with the Kauffmann et al. (2003b) demarcation line. Two-thirds of the galaxies identified by our rejuvenating candidate selection are shown here to not have truly star-forming emission. 56

2.10 Fraction of candidate rejuvenating galaxies after removal of AGN-dominated galaxies, $f_{\rm r} = N_{\rm r}/N$, where $N_{\rm r}$ is the number of candidate rejuvenating central(satellite) galaxies and N is the total number of central(satellite) galaxies. The data is binned by stellar-mass, with low stellar-mass on the left and high stellar-mass on the right. . 57

2.11 Histograms of stellar mass binned RQ and star-forming galaxies with respect to r/r_{180}. Here, low stellar mass (top panel) refers to galaxies with stellar mass $10^6 < M_* \leq 10^{10}$ $\mathrm{M}_\odot$ and high stellar mass (bottom panel) refers to galaxies with stellar mass $10^{10} < M_* \leq 10^{13}$ $\mathrm{M}_\odot$. The mean distribution of each plot is shown for ease of comparison. Errors are computed using the normalised count in each bin. 60

2.12 Histograms of halo mass binned RQ and star-forming galaxies with respect to $\Delta v/\sigma$. Here, low halo mass (top panel) refers to groups with halo mass $10^{11} < M_h \leq 10^{13.5}$ $\mathrm{M}_\odot$ and high halo mass (bottom panel) refers to groups with halo mass $10^{13.5} < M_h \leq 10^{16}$ $\mathrm{M}_\odot$. The mean distribution of each plot is shown for ease of comparison. Errors are computed using the normalised count in each bin. 62

2.13 Distributions of flux ratios Hα/Hβ in three stellar mass (M_*) bins as labeled in each panel. We see the flux ratio distribution is the same for central galaxies and satellite galaxies with respect to stellar mass. 67

2.14 Distributions of flux ratios Hα/Hβ in three absolute normalised velocity offset ($|\Delta v/\sigma|$) bins. We see the flux ratio distribution is the same regardless of velocity offset. 68

2.15 Distributions of flux ratios Hα/Hβ in three halomass (M_h) bins. We see the flux ratio distribution is the same regardless of halomass. 69

2.16 Distributions of flux ratios Hα/Hβ in three group-centric radius (r/r_{180}) bins. We see the flux ratio distribution is the same regardless of group-centric radius. 70

2.17 Distributions of flux ratios Hα/Hβ for star-forming ($\log(\mathrm{sSFR_{UV}}[\mathrm{yr}^{-1}]) > -11.1$) and quenched ($\log(\mathrm{sSFR_{UV}}[\mathrm{yr}^{-1}]) \leq -11.1$) galaxies. We see the quenched population is not unduly biased by high flux ratios (i.e. dust attenuation coefficients). . 71

3.1 Two examples of galaxy lightcurves, with variability = 0.46 on the left and variability = 1.53 on the right as measured using Equation 3.1. r-band magnitudes are plotted as red circles, with g-band magnitudes plotted as green triangles, for illustrative purposes. Here, the dashed line represents the constant line of best fit through the photometric datapoints. These galaxies were chosen to have similar mean r magnitudes, similar number of photometric observations, and similar observation time periods. 75

3.2 BPT diagram with demarcation lines from Kauffmann et al. (2003b) (dashed) and Kewley et al. (2006) (solid). The colourbar indicates number of galaxies found at each point in a contour region. 79

3.3 Variability distributions of AGN, star-forming galaxies, and composite galaxies. Here, distributions are normalised so that the area under each curve is 1. 81

3.4 Mean variability binned by stellar mass, separated by emission type. Shaded regions indicate the standard deviation of the mean in that bin. Bins with fewer than 3 galaxies are omitted for clarity. 83

3.5 The relation between sSFR and M_* of galaxies, separated by emission type (AGN [circle] and star-forming [star], composite galaxies are omitted for clarity), and colour-coded by variability. 85

3.6 Mean variability binned by different quantities, separated by emission type. Shaded regions indicate the standard deviation of the mean in that bin. Bins with fewer than 3 galaxies are omitted for clarity. Left: mean variability against bulge-to-total ratio. Centre: mean variability against half-light radius. Right: mean variability against $\log(\mathrm{sSFR}/\mathrm{yr}^{-1})$. 86

3.7 Three hypothetical scenarios that could possibly describe the behaviour of variability in sSFR-M_* space. Scenario A) describes a situation where the BPT identifies all the AGN, and so variability is tightly linked to stellar mass and lack of star-formation. Scenario B) illustrates the idea of variability being dependent on gas content in a galaxy, so higher gas content implies higher SFR implies higher variability. Scenario C) is the situation we see in Figure 3.5, where a galaxy funnels gas into the centre after some time forming stars, exhibits variability, consumes the gas and quenches. 87

3.8 Scenario C) illustrated further; see text for full details. The colourbar is as in Figure 3.7, where pink denoted low variability and purple denotes high variability. The symbols refer to different stages of a galaxy's evolution, as explained in the text. . . 88

3.9 Magnitude against magnitude uncertainty for each epoch in the ZTF dataset. For plotting purposes, the number of datapoints has been reduced from 10^5 to 10^4. . . . 96

3.10 Example plots of the relation between the true variability and the reco variability, in various magnitude bins. The purple points are the simulated datapoints; the black points are the best fit line through the datapoints; the teal shaded region shows the 1σ area around the best fit; the black dashed line shows the $y = x$ line for illustrative purposes. 97

4.1 PanSTARRS i-band cut-out images (Flewelling et al., 2020) of SLSN sources and of a SN Type Ia host. Panel a) shows object ZTF21aaarmti, panel b) shows object ZTF22aalzjdc and panel c) shows object ZTF18aangpkx. The magenta circle in each panel depicts the location of the source. In panel b), no host galaxy was found for the source. The host galaxy in panel c) is in a higher-density environment than the SLSN hosts; see Section 4.3.1 for details. The absolute magnitude of the host galaxy in panel a) is $M_i = -21.36$ and its redshift is $z = 0.193$. The absolute magnitude of the host galaxy in panel c) is $M_i = -22.67$ and its redshift is $z = 0.070$. The redshift of the SLSN source in panel b) is $z = 0.200$. The size of each of the images is $62.50''$. 102

4.2 Histograms of the colours, absolute magnitudes, and redshifts of galaxies in SLSN-g with reliable photometry compared to the matched SDSS sample. KS-tests result in p-values of 0.46, 0.36, and 0.75 respectively, validating that the SLSN-g and SDSS-m samples match each other. 104

4.3 A scatter plot of the number of bright Spec-z galaxies within 2 Mpc of a target galaxy against absolute magnitude, compared to a 2d histogram of the same distribution for Type Ia SNe host galaxies. SLSN-g is shown as dark purple circles and the matched sample, SDSS-m, is shown as light purple triangles. Normalised histograms are included on the $x-$ and $y-$axes and show the absolute magnitude and N_2 distributions for SN-Ia, SDSS-m and SDSS-g. 108

4.4 A colour-magnitude diagram comparing SLSN-g and SDSS-m to SN-Ia. Low-density SLSN-g galaxies are plotted in purple circles, high-density SLSN-g galaxies are plotted in orange pluses, low-density SDSS-m galaxies are plotted in purple crosses, high-density SDSS-m are plotted in orange triangles, and the distributions for low- and high-density SN-Ia galaxies are plotted as purple filled in contours and orange contour lines respectively. Open purple circles represent the SLSN-g sources with unreliable host photometry. Purple and orange points shown individual SN-Ia galaxies when they are not captured by the contours. 109

4.5 Histograms of metallicity (left) and sSFR (right) in IllustrisTNG for all blue low-mass (BLM) galaxies (black), BLM field galaxies (purple) and BLM group galaxies (orange). 110

4.6 Fractions of BLM-f (purple) and BLM-g (orange) of the total BLM sample with respect to metallicity. The gray dashed line shows the metallicity at which group galaxies account for 3 per cent of the entire BLM sample, in accordance with observations, with upper and lower limits shaded in gray. 113

List of Tables

4.1 Descriptions of each of the samples used. The columns are the name of the sample, the number of objects in the sample, the minimum and maximum of the redshift, the median of the redshift, the minimum and maximum of the absolute magnitude, the median of of absolute magnitude, and the description of the sample. 101

4.2 Table of ZTF IDs of the transient events that were obtained on the BTS, the group that classified them as SLSNe, and the relevant citation. 117

Chapter One

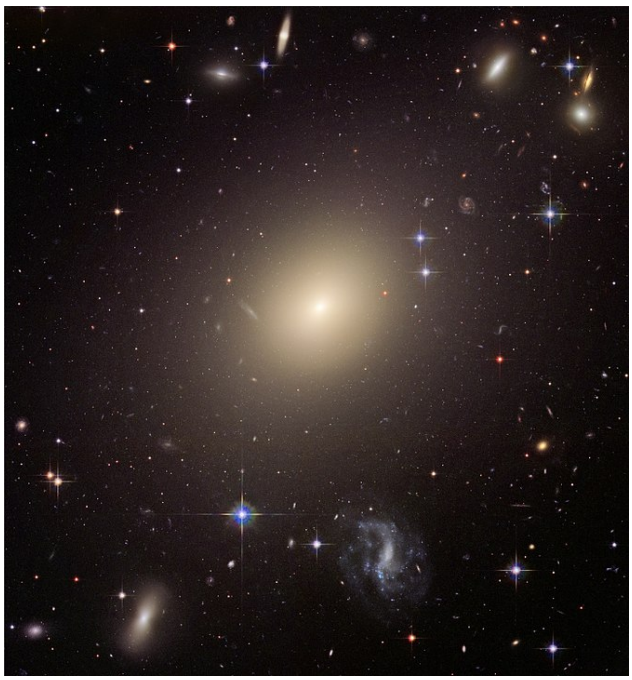
Introduction

Humans have long looked up to the sky and studied what we see. Astronomy is a discipline that is millennia old, with civilisations around the world each trying to explain the cosmos. The topics covered in this thesis, however, were unknown of until extremely recently (relatively speaking). Just 100 years ago, there was no notion of anything existing beyond the Milky Way. It was in 1924 that Edwin Hubble discovered that the nebulous objects seen in the sky were in fact far too distant to be part of the Milky Way, and must be galaxies in their own right. In the century since, the field of extragalactic astronomy has rapidly expanded with new insights into the formation and evolution of galaxies, the large-scale structure of the Universe, and our place within it all.

We now know that galaxies fall broadly into two classes, spiral and lenticular/elliptical (sometimes referred to as late-type and early-type, respectively), with each class being further subdivided based on the morphology of the galaxy. Figure 1.1 shows some examples of different galaxies, and illustrates the main differences between them. Spiral galaxies (Figure 1.1a) are typically blue in colour, due to their active star-formation. Contrastingly, elliptical galaxies (Figure 1.1b) are much redder in colour, and have usually completely ceased forming new stars. In terms of their morphology, spiral galaxies consist of a disk component and a central bulge. The disk is where the majority of the star-formation occurs. Spiral arms in the disk work to funnel gas towards



(a) An example of a spiral galaxy, the Pinwheel Galaxy (M101). The blue spiral arm structure is very clear, while the bulge in the centre is red in colour. By ESA/Hubble.



(b) An example of an elliptical galaxy, ESO 325-G004. There is less defined structure, and the entire galaxy is red in colour. By NASA, ESA, and The Hubble Heritage Team (STScI/AURA); J. Blakeslee (Washington State University).

Figure 1.1: Some examples of the morphologies of galaxies.

the center, which is a possible method by which the bulge grows (Kormendy and Kennicutt, 2004; Athanassoula et al., 2013); the bulge may also grow by galaxy mergers (Aguerri et al., 2001). The bulge of a spiral galaxy often has reduced star-formation, and houses a black hole in the very center. On the other hand, elliptical galaxies are much less defined in their structure. Consisting of older stellar populations, ellipticals are lacking in the interstellar materials which fuel star-formation such as gas and dust found in spirals. A supermassive black hole can be found at the center of an elliptical galaxy, with many of them being active (i.e. an active galactic nucleus).

It naturally follows to ask, what is the connection between these two very different types of galaxies? It has been established that late-type galaxies eventually evolve into early-type (Toomre and Toomre, 1972), but the exact processes at work are not yet fully understood. The main driver (or, alternatively, consequence) of this evolution is the reduction or cessation of star-formation. The term 'quenching' is used to refer to any process or processes which result in a reduced star-formation rate. There are many mechanisms that may contribute to quenching of star-formation; these will be discussed in more detail in this Chapter.

This introductory chapter aims to provide the required background and context for the subsequent chapters. First, I will discuss the main relevant differences between types of galaxies. I will then outline the main quenching mechanisms. Finally, I will give a brief overview of luminous stellar transients and their role in the study of galaxy evolution.

1.1 Characteristics of galaxies

1.1.1 Morphology

Let's first describe in more detail the defining characteristics of the main two classes of galaxy (Binney and Tremaine, 2008). Elliptical galaxies are spheroidal structures, with little to no cool

interstellar gas. As their name suggests, they follow an elliptical surface brightness profile, with semi-major axis a and semi-minor axis b. The surface brightness profile may be modelled by the Sérsic law:

$$I_m(R) = I_e \exp\left(-b_m\left[(R/R_e)^{1/m} - 1\right]\right), \tag{1.1}$$

where m is the Sérsic index and I_e is the surface brightness at the effective radius R_e. The parameter b_m is a function of Sérsic index, and can be well-described by $b_m = 2m - 0.324$ over the range $1 < m < 10$. The Sérsic index $m = 4$ defines the de Vaucouleurs law (de Vaucouleurs, 1948), which is used to describe the surface brightness profile of elliptical galaxies and bulges. At $m = 1$, the result is an exponential profile which fits a disk, which is often appropriate for spiral galaxies.

The dimmest elliptical galaxies are known as diffuse dwarf galaxies, or dwarf spheroidals. These typically have larger effective radii and lower surface brightnesses than other ellipticals at the same luminosity (Mateo, 1998). Dark matter is thought to contribute ~ 90 per cent of the mass of a dwarf spheroidal, thus these galaxies offer unique probes into the effects of dark matter.

Spiral galaxies differ from elliptical galaxies in just about every way. Their most defining features are the disk and constituent spiral arms which facilitate the vast majority of the star-formation. Spiral galaxies are relatively abundant in low-density environments, however make up only about 10 per cent of galaxies in higher-density environments (Dressler, 1980). The circular rotation speeds (v_c) of interstellar neutral hydrogen can be measured using the 21cm line; v_c flattens out at large radii, providing some of the first evidence for the existence of dark matter (Rubin et al., 1980). Spiral galaxies also contain a bulge at the centre, not dissimilar to a small elliptical structure. The bulge is relatively distinct from the spiral arms, and houses older, redder stars. The luminosity of the bulge is correlated to other properties of the galaxy such as the gas fraction, colour, and how tightly the spiral arms are wound (Binney and Tremaine, 2008). In the local Universe, about 65 per cent of spirals have a bar, which is like an extension of the bulge along a third axis (Sheth et al., 2008).

Lenticular galaxies are somewhat of a transitional galaxy between spirals and ellipticals. They typically have a rotating disk and a bulge, but have little to no gas and thus little to no recent or ongoing star-formation. Such galaxies are rare in the field, but common in high-density environments. This gives rise to the idea that lenticular galaxies come from spiral galaxies that have had their star-formation shut off by interactions with the intergalactic medium upon infall to a group or cluster (van den Bergh, 1976; Binney and Tremaine, 2008).

1.1.2 Gas and star-formation in star-forming galaxies

The gas found in galaxies, often referred to as the interstellar medium (ISM), is made up of many different chemical elements and molecules. As each element and molecule has distinct observation requirements, advantages, and snags, astronomers can exploit various techniques to probe the ISM and glean different information about these tracers. The most abundant of these is neutral atomic hydrogen (HI), which has an emission line at 21 cm. Due to its long wavelength, obtaining any sort of spatial resolution is typically not possible, except with the use of radio interferometry, such as at the Very Large Array, or the upcoming Square Kilometre Array. Still, measuring the amount of neutral atomic hydrogen in a galaxy is crucial to understanding the journey on which gas goes to be converted into stars.

Of the molecular gas, neutral molecular hydrogen (H_2) is the most common. This molecule has high excitation energies, and so requires very energetic conditions in order to be observable (> 500 K). That said, molecular hydrogen is not the only molecule found in the ISM. McGuire (2018) summarises the molecules that have been detected in the ISM, amounting to over 200 distinct molecules. Besides H_2, the most abundant molecule is carbon monoxide (CO). CO can be easily observed by ground-based telescopes, making it a favourable probe for the ISM. The CO emission flux can be converted to a luminosity $L'_{\rm CO}$, which, in turn, can be converted to a molecular gas mass $M_{\rm H_2}/{\rm M}_\odot$ using a conversion factor $\alpha_{\rm CO}$. For typical Galactic ISM conditions, this conversion

factor is $\alpha_{CO} = 3.2\ M_\odot \left(K\ km\ s^{-1} pc^2\right)^{-1}$. The exact details behind this conversion factor and other details about CO as a tracer for molecular gas can be found in Saintonge and Catinella (2022) and references within.

Dust that is mixed in with gas can also be used to measure the gas content of a galaxy, as the dust absorbs and re-emits light in the infrared. The total gas mass can be estimated by applying the dust-to-gas ratio, which is related to the metallicity of the gas (Groves et al., 2015).

In terms of relations between the gas content of the galaxy and other properties, Schmidt (1959) first proposed that the surface star-formation rate density is proportional to the surface gas density, i.e. $\Sigma_{SFR} \propto {\Sigma_{gas}}^n$, with $n \approx 2$. About 30 years later, Kennicutt (1989) used HI and CO measurements for the gas, combined with Hα measurements for the SFR, and found $n = 1.3 \pm 0.3$. He noted that there seemed to be some critical gas density required before star-formation could take place. This critical density was derived from the idea of gravitational stability in rotating disks (Toomre, 1964): $\Sigma_{crit} = \alpha\sigma\kappa/3.36G$, where α is a dimensionless constant, σ is the velocity dispersion, κ is the epicyclic frequency within the disk, and G is the gravitational constant. We can find α by making some simple assumptions. With a constant velocity dispersion within the disk, the epicyclic frequency can be found directly from the rotation curve V as a function of the radial position R. Taking a reasonable value for σ, an expression for Σ_{crit} in α, V and R is obtained. One can then compare observations of gas densities and the critical density as a function of radius to the observed radius of the outermost HII regions (indicative of star-formation) of a number of galaxies, to constrain the value of α. This approach led Kennicutt (1989) to determine $\alpha = 0.7$.

A decade later, Kennicutt (1998b) returned to this relation (the Kennicutt-Schmidt relation, or KS relation), this time combining normal spiral galaxies with star-burst galaxies. With both the gas surface density and the star-formation rate surface density spanning several orders of magnitude, a very tight relation was found, with $n = 1.4 \pm 0.15$. However, this value remains very sensitive to the data used and the methodology. Boissier et al. (2003) test a variety of possible fits on 16

resolved galaxies, and find $n = 2.06$; Misiriotis et al. (2006) analyse the gas and dust distributions of the Milky Way, and the SFR, and find $n = 2.18 \pm 0.2$; Luna et al. (2006) also study the Milky Way, with CO observations from the southern hemisphere, and find $n = 1.2 \pm 0.2$, and that star-formation also depends on the amount of shear, i.e. effects caused by differential galactic rotations. Spatially-resolved SFR and CO measurements of M51 gave $n = 1.56 \pm 0.04$ (Kennicutt et al., 2007); in M33, which has a small amount of molecular gas, the slope $n = 1.36$ was found for $\Sigma_{\rm SFR}$ against $\Sigma_{\rm H_2}$. A strong correlation between SFR and molecular gas density was also found in M33 (Heyer et al., 2004). In simulations, the slope to the KS relation has been found to be $n \sim 1.4 - 1.5$ (Kravtsov, 2003; Li et al., 2006; Tasker and Bryan, 2006). Harfst et al. (2006) find a slope of $n = 1.7 \pm 0.1$; they also find that at low gas surface density $\left(\Sigma_{\rm gas} \lesssim 10\ {\rm M_\odot\ pc^{-2}}\right)$, the SFR dips $1 - 3$ dex below the relation. They explain this by the fact that below this gas density, it will be difficult for gas to condense and form a thin disk.

Kennicutt and Evans (2012) characterise three roughly distinct regimes of star-formation, governed by the local gas density. Ranging from low $\Sigma_{\rm gas}$ $\left(< 10\ {\rm M_\odot\ pc^{-2}}\right)$, to intermediate $\left(10 - 100{\rm s\ M_\odot\ pc^{-2}}\right)$, and high $\left(> 100{\rm s\ M_\odot\ pc^{-2}}\right)$, star-formation in these regimes is found, for example, respectively, in outer disks, dwarf galaxies, or early-type galaxies; molecular clouds or normal disks; and, starbursts or mergers. The question, then, is how can we quantitatively trace these regimes and relate them to galactic properties such as star-formation?

Scaling relations can give us insights into the important processes that give way to (or hinder) star-formation. Some relations are shown in Figures 4 and 5 of Saintonge and Catinella (2022). Here, they use data from the xGASS (Catinella et al., 2018) and xCOLD GASS (Saintonge et al., 2017) datasets to illustrate the relations. They show that the gas fractions of HI and H_2 ($f_{\rm HI}$ and $f_{\rm H_2}$ respectively) are anti-correlated with stellar mass, due to the existence of high-mass gas-poor galaxies. There is a tight relation between $f_{\rm H_2}$ and sSFR, i.e., the KS relation. On the other hand, $f_{\rm HI}$ more tightly correlates with the NUV-r colour. This is explained by the fact that HI traces star-formation in the outer disks of galaxies, which can be seen for example in M83 (Bigiel

et al., 2010).

In order to put these scaling relations to use, we can consider the star-forming main sequence (SFMS, or MS for short). The MS refers to the tight relation seen between stellar mass and SFR for star-forming galaxies. This relation allows for a galaxy's star-formation activity to be characterised by the distance between the galaxy's position on the stellar mass-SFR plane and the MS, i.e. ΔMS. Galaxies found $\gtrsim 0.5$ dex above the MS are often considered to be undergoing a starburst, while galaxies below the MS are undergoing reduced star-formation, and are considered quenched if ΔMS $\lesssim -1$ dex. This is illustrated in Figure 1.2 (adapted from Saintonge et al. (2017)[1]), which shows the shape of the MS on the SFR-M_* plane, along with how $f_{\rm HI}$ varies throughout this plane. The MS describes a fairly linear relation between SFR and stellar mass, but it flattens after a characteristic mass, which we will denote $M_{\rm char}$. This means that the star-formation efficiency decreases with high mass, even though these are star-forming galaxies. This flat regime may be explained by the fact that as galaxies increase in stellar mass, they become more bulge-dominated, which doesn't necessarily translate to an increase in SFR. Figure 1.2 also illustrates the decrease in $f_{\rm HI}$ at high stellar mass, indicating that gas reservoirs may not grow proportionally with the growth of the galaxy. The stellar mass $M_{\rm char} \sim 10^{10}$ M$_\odot$ corresponds to a halo mass of $\sim 10^{12}$ M$_\odot$, which is shown in simulations (Kereš et al., 2009) to be a threshold halo mass where accreted gas cannot efficiently cool and condense into stars.

The scatter of galaxies about the MS can provide some insights into how the behaviour of gas can affect the SFR. As mentioned earlier, the distance of a galaxy from the MS can give an idea as to whether it is producing more stars than normal, or fewer. In other words, ΔMS gives a simplified view of the recent star-formation history (SFH) of a galaxy. We can see in Figure 1.2 that the galaxies with the smallest values of $f_{\rm HI}$ also lie mostly below the MS, and vice versa. This suggests a strong link between the gas content of a galaxy and its distance from the main sequence. It also provides some insight for the timescales required for galaxies to move either

[1]A similar figure depicting H_2 gas fractions can also be found in Saintonge et al. (2017).

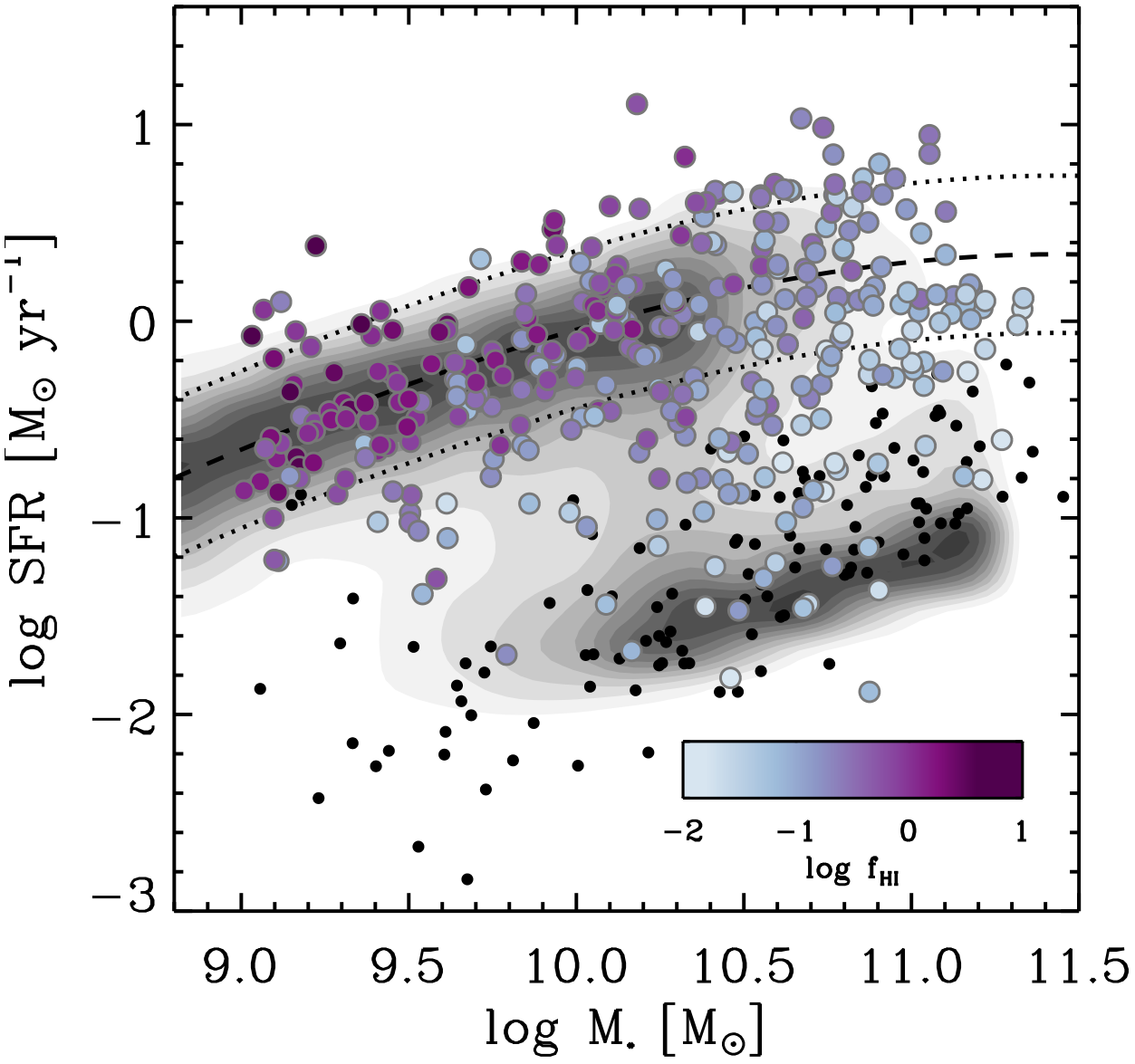


Figure 1.2: Distribution of galaxies on the SFR-M_* plane, showing how the HI fraction changes along the MS. The MS is plotted as a dashed line, with dotted lines showing the 0.4 dex scatter about the MS. Shaded contours show the entire SDSS sample at $0.02 < z < 0.05$; black dots are galaxies with gas fractions below the xCOLD GASS detection limit; coloured circles show the HI gas fractions of galaxies colour-coded on a logscale. Figure adapted from Saintonge et al. (2017).

above or below the MS: since gas consumption timescales are $\gtrsim$ Gyrs, any gas-driven changes to a galaxy's position on the main sequence must operate on a similar timescale.

As Chapters 2 and 3 require the use of BPT (Baldwin, Phillips and Terlevich) diagrams (Baldwin et al., 1981), it is appropriate to introduce them now. A BPT diagram (see Figure 2.9, Figure 3.2, or Figure 1 of Kewley et al. (2006) for an example) depicts ratios of emission lines in order to diagnostically determine whether a galaxy's emission is characteristic of star-formation or AGN activity. For the purposes of this work, the emission line ratios [NII]/Hα and [OIII]/Hβ are used. The BPT diagram consists of 2-3 regions: a region of high ratios of ionised metals to Hα and Hβ, indicative of AGN activity; a region of lower ratios, i.e. higher amounts of star-formation tracers Hα and Hβ, indicative of star-formation; and a region in between referred to as 'composite'. The regions are demarcated by empirically determined lines (Kewley et al., 2001; Kauffmann et al., 2003b; Kewley et al., 2006).

Now that we have established how gas relates to the star-formation activity of the galaxy, we turn our attention to attempting to disentangle the various processes that directly affect the ability of gas to condense into stars.

1.2 Late-stage evolution: quenching

Since the mid-to-late 2000s, it has been understood that 'quenching' is the name given to the process(es) that move a galaxy from the blue cloud to the red sequence on a colour-magnitude diagram (Strateva et al., 2001; Baldry et al., 2004; Faber et al., 2007). The region of parameter space through which the galaxy transitions is referred to as the 'green valley' (Salim, 2014). These regions in colour-magnitude space (in this case, colour-stellar mass space, qualitatively the regions are the same) are illustrated in Figure 1.3. This bimodality persists in many galaxy properties (Kauffmann et al., 2003a), most notably in the specific star-formation rate (the star-formation

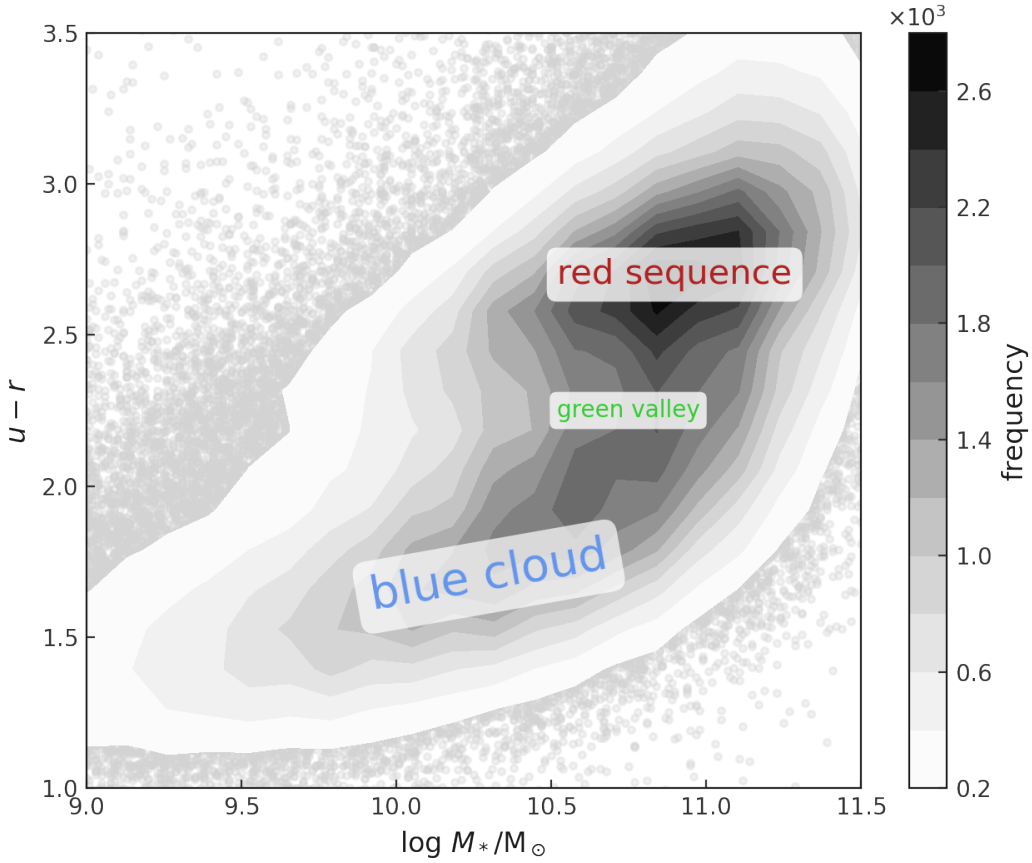


Figure 1.3: The distribution of SDSS galaxies at $z < 0.2$ with $u - r$ colour against stellar mass. The red sequence is shown, with redder colour and higher stellar mass. The blue cloud, however, is populated by bluer galaxies and galaxies with lower stellar mass. The green valley is the less densely populated region between the red sequence and the blue cloud. Contours connect bins that contain the same number of galaxies, as indicated by the z-axis. Outside the lowest contour level, grey dots show individual galaxies.

rate divided by the stellar mass, sSFR) as shown in Figure 1.4. Peng et al. (2010) note that quenching is distinct from the global decline in star-formation rate since $z \sim 2$. In the decade since, there has been an ongoing discussion about 'nature vs nurture', referring to whether quenching depends on the intrinsic properties of the galaxy itself, or the local environment in which it resides. Observationally, correlations have been found between galaxy stellar mass and colour (Baldry et al., 2006) (and thus, star-formation rate), leading Peng et al. (2010, 2012) to define 'mass-quenching' as any quenching that occurs as a function of stellar mass. However, the exact processes are more complex and generally correlated with stellar mass. Alternatively, galaxies found in groups or clusters (as satellites, rather than centrals) are more likely to be quenched than isolated galaxies at the same mass (Peng et al., 2012; Wetzel et al., 2012; Smethurst et al., 2017). This will be discussed further in Chapter 2.

Nevertheless, it has been shown that the effects of mass-quenching and environmental quenching are separable (Peng et al., 2010). However, this assertion may not be as straightforward, as argued in Smethurst et al. (2017), due to the fact that the local environment of galaxies can have profound effects on various galactic properties, including the morphology, which can lead to mass-quenching. In other words, the processes responsible for mass-quenching and environmental quenching are interdependent. Furthermore, the quenching pathways that move a galaxy from the blue cloud, through the green valley, to the red sequence are varied in timescale and method, and may be encoded in the resulting morphology of the galaxy (Schawinski et al., 2014).

In a less direct sense, the large-scale environment also has a profound effect on the star-formation rate of the galaxy, and furthermore on the overall picture of environmental quenching. When it comes to the environment of galaxies, they can either be found in low-density environments (i.e., the field), in high-density environments such as galaxy groups (< 50 galaxies), or in even higher-density environments such as galaxy clusters (100s - 1000s of galaxies). As will be discussed later in this section, galaxies are more likely to be quenched in high-density environments, with virtually all galaxies in massive clusters showing very little or no star-formation. It has been shown

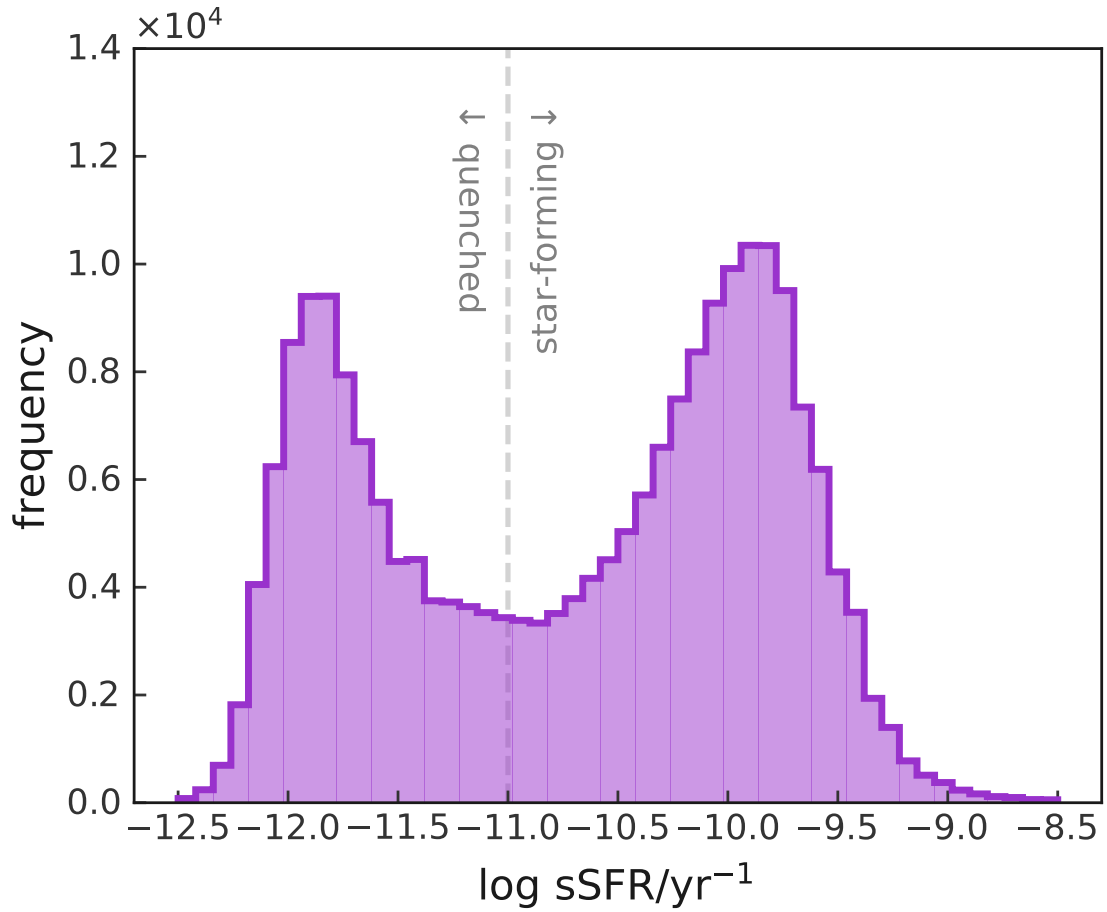


Figure 1.4: A histogram of the specific star-formation rate, sSFR, of SDSS galaxies. Two peaks are clearly visible, corresponding to the star-forming population and the quenched population. The region between the two peaks corresponds to a transitionary phase of galaxy evolution, sometimes referred to as the 'green valley'.

that the group environment is very important for pre-processing galaxies (see McGee et al., 2009), that is, a significant portion of satellite quenching occurs in galaxy groups which, in turn, infall into galaxy clusters.

The following subsections will briefly describe the most commonly investigated quenching mechanisms, separated broadly by internal mechanisms which rely on the intrinsic properties of the galaxy itself, and external mechanisms which rely on the environment in which the galaxy resides.

1.2.1 Internal mechanisms: Supernova feedback

'Supernova' is a general term used to describe the violent and explosive end of a star's life. These events, sometimes visible with the naked eye, have been observed by various civilisations for millenia. Yet, it is only in the last century that their astrophysical origins have begun to be uncovered. Today, thousands of supernovae have been detected, with several distinguishing features. There are a number of main supernova classifications, mostly determined by their spectra.

Type I supernovae show no hydrogen in their spectra. Type Ia supernovae arise when a white dwarf in a binary system reaches its critical mass, by either accreting material from a companion star or merging with its companion star. With enough mass, the star undergoes a runaway nuclear reaction which releases enough energy for the star to explode. Since Type Ias require evolved stars, they occur as a function of galaxy stellar mass (and, consequently, evolutionary stage of the galaxy). Type Ib/c supernovae, on the other hand, occur by the core collapse of massive stars. Thus, the rate of this type of supernova is strongly correlated with the star formation rate of galaxies. Type II also come from the core collapse mechanism, although their spectra do show hydrogen.

Stellar feedback has been shown in simulations to play an important role in the regulation of the galaxy growth (e.g., Schaye et al., 2015; Martizzi et al., 2016; Smith et al., 2018b; Lucas et al., 2020). Due to the vast amounts of energy released by supernovae $\left(\sim 10^{51}\ \mathrm{erg}\right)$, star-formation may

be suppressed by either stellar winds or supernova feedback, although stellar winds only dominate in young ($< 10^7$ yr) starbursts that form high-mass stars (> 60 $M_\odot$). In the case when the mass-loss rate scales with star-formation rate, and with a supernova rate of $\approx 0.02(\mathrm{SFR}/M_\odot\ \mathrm{yr}^{-1})$, the momentum injection due to stellar winds and supernovae may be written as (Veilleux et al., 2005),

$$\dot{p}_* = 5 \times 10^{33}(\mathrm{SFR}/M_\odot \mathrm{yr}^{-1})\ \mathrm{dyne}. \tag{1.2}$$

The efficiency with which a starburst transfers mechanical energy to the ISM to heat surrounding gas is the thermalization efficiency, ξ. This is thought to be only around 10 per cent (see Veilleux et al., 2005), meaning energetic or mechanical feedback from stars is likely not enough to regulate star-formation in a galaxy. Feedback from even more energetic AGN likely also contribute significantly to the regulation of galaxy growth.

1.2.2 Internal mechanisms: AGN feedback

An active galactic nucleus (AGN) refers to the central region of a galaxy that is extremely luminous and energetic, powered by a supermassive black hole. The luminosity is thought to come from material accreting onto the black hole, which, due to the increased friction within the accretion disk, releases enormous amounts of energy into the galaxy surrounding it. It has been shown that there are correlations between AGN and many of their host galaxy properties (Fabian, 2012). For example, generally AGN are more likely to be located in massive, elliptical galaxies (Gültekin et al., 2009; Heckman and Best, 2014), and stronger AGN are found in the most massive galaxies (Hu, 2008; Gültekin et al., 2009). Most notably, there is a very tight correlation between the mass of the supermassive black hole and the velocity dispersion of the host bulge: the $M - \sigma$ relation (Gebhardt et al., 2000; Ferrarese and Merritt, 2000). It has also been shown that the star-formation rate of a galaxy can depend on the activity of the black hole (Page et al., 2012), this will be discussed further in Chapter 3. Although star-formation rate correlates with the stellar mass and morphology of galaxies, AGN are thought to have a more direct effect on regulating star-formation,

and thus the growth of the galaxy. Via AGN feedback, AGN suppress the formation of new stars by either expelling the cold gas required for star-formation, or heating up the gas, preventing it from condensing into stars. These two modes, known as the radiative mode and the kinetic mode respectively, operate on different mechanics in the AGN.

The observational evidence that gives rise to the $M - \sigma$ relation provides some evidence of the radiative mode regulating the growth of the galaxy. This can be shown by assuming the radiation pressure from a black hole at the Eddington luminosity limit is balanced by the gravitational pressure from the gas, where the Eddington luminosity is $L_{\rm Edd} = 4\pi G M_{\rm BH} m_p c/\sigma_{\rm T}$:

$$\frac{L_{\rm Edd}}{c} = \frac{4\pi G M_{\rm BH} m_p}{\sigma_{\rm T}} = \frac{G M_{\rm gal} M_{\rm gas}}{r^2}. \tag{1.3}$$

Let $f = M_{\rm gas}/M_{\rm gal}$ be the fraction of the galaxy mass that is gas. Under the assumption the galaxy is isothermal and spherical, we can write $M_{\rm gal} = 2\sigma^2 r/G$ (Binney and Tremaine, 2008), so the above expression(s) can be written as,

$$\frac{G M_{\rm gal} M_{\rm gas}}{r^2} = \frac{f G M_{\rm gal}^2}{r^2} = \frac{fG}{r^2}\left(\frac{2\sigma^2 r}{G}\right)^2. \tag{1.4}$$

From here we can write

$$\frac{4\pi G M_{\rm BH} m_p}{\sigma_{\rm T}} = f\frac{4\sigma^4}{G}, \tag{1.5}$$

which shows that $M_{\rm BH} \propto \sigma^4$, providing an explanation for the empirical relation already shown. This simple derivation shows how a black hole at or near the Eddington limit can suppress accretion onto the galaxy, and thus quench star-formation.

AGN winds may also be responsible. The kinetic luminosity of a wind is a function of column density, velocity, covering fraction, and radius. It must be greater than the Eddington luminosity in order for the gas to be expelled. It is not clear that AGN winds are sufficient to drive gas, as very high velocities are required. Observations of high-velocity galactic outflows are in general difficult to obtain, because of obscuration of the AGN. That said, outflow rates of

420 $M_{\odot}yr^{-1}$ at 1100 km s^{-1} have been observed at low redshift (Rupke and Veilleux, 2011). Other observations include a region of suppressed star-formation over a $z = 2.4$ quasar, where the outflow velocity is highest (Cano-Díaz et al., 2012), and at the even higher $z = 6.4$, an outflow of velocity 1300km s^{-1}, which ejects the molecular gas of the galaxy in $< 10^7$ yr (Maiolino et al., 2012).

In the most massive galaxies at the centres of groups and clusters, the kinetic mode is more prominent. This mode is involved when the AGN are not as luminous, and are active in the radio. In this mode gas is heated by the energy of the AGN, preventing collapse into stars.

Due to X-ray radiation in the centre of massive clusters, a cooling flow takes place. Observational evidence shows that clusters such as A 1835 (Schmidt et al., 2001; McNamara et al., 2006), A 426 (the Perseus cluster, Fabian et al., 2006) and A 262 (Blanton et al., 2004; Sanders et al., 2010) have a significant temperature drop in the central regions. However, if uninhibited by any heating sources, the predicted mass cooling rates would be indicative of much higher star-formation rates than seen. Therefore, it is thought that the AGN could be supplying heat to the surrounding area (Pedlar et al., 1990; Baum and O'Dea, 1991; Tabor and Binney, 1993; Tucker and David, 1997). Jets from the AGN deposit energy into bubbles suspended in the surrounding hot gas (McNamara et al., 2000). These bubbles of hot plasma have been observed around the nuclei of BCGs (Boehringer et al., 1993). The bubbles then rise buoyantly through the hot interstellar medium (or intergalactic medium), consequently pushing aside the hot gas and making way for new bubbles to form. However, it has been found that the production and dissipation of bubbles is a gentle, continuous process, and that the energy is more likely distributed via shock waves that arise from differences in pressure from jets (Fabian et al., 2003, 2006). Such shock waves have been observed in various clusters such as the Virgo cluster (Forman et al., 2005), the Centaurus cluster (Sanders and Fabian, 2008) and A 2052 (Blanton et al., 2011), although these are only observable in the brightest clusters due to the weak amplitude of the waves (Graham et al., 2008).

While these effects have also been observed in lower X-ray luminosity groups of galaxies

(David et al., 2011; Randall et al., 2011), it is unclear the extent to which they occur in elliptical galaxies (Nulsen et al., 2007; Nulsen et al., 2009), and how the bubbling activity scales with galaxy mass/luminosity, if at all. Attempting to observe these effects in smaller galaxies poses challenges such as lower resolution, low surface brightness and low-mass X-ray binaries contaminating sources (e.g. Humphrey et al., 2011).

1.2.3 External mechanisms: In-falling galaxies

Evidence of a morphology-density relation was shown by Dressler (1980), which found that early-type galaxies are more likely to be found in higher-density environments such as the cores of rich clusters. Furthermore, while the fraction of elliptical galaxies increases to $60-70$ per cent in the cluster core, the fraction of lenticular galaxies increases with decreasing cluster-centric radius, before decreasing significantly in the central region (Whitmore et al., 1993; Boselli and Gavazzi, 2006). Spiral galaxies are much rarer in high-density environments, and are only found in the outskirts of local clusters; although rare passive spirals have been found in high-density environments (Goto et al., 2003a). At high redshift ($z \sim 0.5$), the spiral fraction in rich clusters is higher, and the lenticular fraction is lower (Dressler et al., 1997; Fasano et al., 2000). This suggests that over the last few Gyr, elliptical and lenticular evolve from spiral galaxies (e.g. Peng et al., 2015).

In the Sloan Digital Sky Survey (SDSS), such relations with galaxy density are also seen, with the presence of red bulge-dominated galaxies increasing as a function of cluster-centric radius (Goto et al., 2003b; Balogh et al., 2004). These relations hold in lower-density environments also, with galaxy groups showing increased numbers of elliptical (and quenched) galaxies (Postman and Geller, 1984; Wetzel et al., 2012, 2013).

There is a clear environmental dependence on the star-formation rate, and more generally,

the evolutionary state of the galaxy. The mechanisms at work are less obvious, although several mechanisms have been proposed. For a galaxy to quench, it needs to run out of cool gas for star-formation. In a somewhat analogous way to AGN feedback, this can happen by either preventing the accretion of fresh gas onto the galaxy due to interactions between the cool interstellar medium and hot intergalactic medium ('strangulation', Balogh et al., 2000; Peng et al., 2015), or by the forceful removal of the gas reservoir (ram-pressure stripping, Gunn and Gott, 1972). Increased gravitational forces at play in a high-density environment can lead to increased galaxy-galaxy interactions, in the form of harassment (Moore et al., 1996, 1998) or mergers (Toomre and Toomre, 1972).

There is evidence that strangulation as a quenching mechanism can explain the observed metallicity differences between star-forming galaxies and quenched galaxies in the local Universe (Peng et al., 2015). If a galaxy cannot accrete fresh gas, but its gas reservoir still remains, it can remain forming stars on gas depletion timescales. For a galaxy that does not accrete any new gas, its star-formation rate declines as (Balogh et al., 2000)

$$\dot{M}_* (t) = \dot{M}_*(0) \left(1 + 0.33\frac{t}{t_e}\right)^{-3.5} \ \mathrm{M}_\odot \ \mathrm{yr}^{-1}, \tag{1.6}$$

where t is defined as some time after the final gas accretion, $\dot{M}_*(0)$ is the initial star-formation rate, and t_e is the characteristic gas consumption timescale. This is found in Balogh et al. (2000) to be ≈ 4 Gyr for a typical star-forming galaxy. This supports the evidence in Peng et al. (2015), which models the metallicity differences between star-forming galaxies and quenched galaxies. Consider a galaxy whose gas reservoir is suddenly stripped away. It quickly quenches, thus its metallicity remains similar to its metallicity before the gas reservoir was removed. Alternatively, if a galaxy retains its gas but simply cannot accrete fresh gas, it will continue to form stars but will also build its metallicity. In other words, it will eventually quench in the time it takes to form the remainder of its gas into stars. Using a closed-box model, Peng et al. (2015) found that the metallicity differences between star-forming galaxies and quenched galaxies matched metallicity differences seen ≈ 4 Gyr after strangulation.

In some cases, the pressure of the hot intergalactic gas can be so great that the cool interstellar gas of the infalling galaxy can be stripped away. This is called 'ram-pressure stripping' (Gunn and Gott, 1972), where the ram pressure P_r is proportional to the velocity of the infalling galaxy as,

$$P_r \approx \rho_e v^2, \tag{1.7}$$

where ρ_e is the intracluster density and v is the speed of the infalling galaxy. A typical spiral galaxy is held together by a force of

$$F = 2\pi G \sigma_s \sigma_g, \tag{1.8}$$

where σ_s is the star surface density and σ_g is the gas surface density. For a typical spiral galaxy with stellar mass of 10^{11} $M_\odot$ and radius of $\sim$ 10 kpc, the star surface density is $\sigma_s = 0.06$ g cm^{-2}. If the gas layer is 200 pc thick, with a density of $\sim$ 1 atom cm^{-3}, the gas density is $\sigma_g \sim 10^{-3}$ g cm^{-2}. This means that the restoring force of the galaxy is 2.5×10^{-11} dyn cm^{-2}. For a galaxy moving through the intracluster medium at 1700 km s^{-1}, we can see from Equation 1.7, the ram-pressure would be $5 \times 10^{-8} n$ dyn cm^{-2}, where n is the intracluster number density. This means that if a cluster has 5×10^{-4} atoms cm^{-3}, an infalling galaxy will be stripped of its gas.

In the decades since this theory of ram-pressure stripping was formalised, much work has been done on galaxies with observable extended gaseous emission, often called 'jellyfish' galaxies (Smith et al., 2010; Poggianti et al., 2017). These tails of ionized gas can extend for 10s of kiloparsec from the original galaxy (Bellhouse et al., 2017), and can even facilitate new star-formation (Poggianti et al., 2019). Of course, since up to 50 per cent of the gas can be lost in this catastrophic process, the galaxy quenches soon after stripping (Bellhouse et al., 2017). Furthermore, there is evidence that the ram-pressure of the group or cluster can have a profound effect on the morphology of the galaxy; the gas trails sometimes appear to follow lines along the spiral arms of the galaxy, indicating the forces involved can cause 'unwounding' of the spiral arms (Bellhouse et al., 2021).

Another fate to which galaxies in high-density environments may be subjected is 'harass-

ment'. This is the combination of tidal-forces from the entire group or cluster and high-speed encounters with other group or cluster members (Moore et al., 1996, 1998). In order for galaxies to be sufficiently affected, there are many factors to consider. The efficacy of the harassment depends on the orbital parameters of the galaxy, the properties of the galaxy itself, and the properties of the group or cluster (Bialas et al., 2015). Tidal forces from the cluster are stronger on galaxies with orbits that bring them closer to the cluster core (Smith et al., 2015). This also increases the chance of encounters with other members. Bialas et al. (2015) find in simulations that the stellar mass loss experienced by galaxies increases from ~ 5 per cent for the outermost orbits to $24-50$ per cent for the closest orbits which have apocentre of 0.5 Mpc. The inclination of the galaxy along its orbit can also have a profound effect on the extent of harassment (Villalobos et al., 2012). For galaxies with an inclination of 90° with respect to the orbital plane, the stellar mass loss is halved compared to galaxies with an inclination of 0° (Bialas et al., 2015). Finally, harassment can induce changes to the structure of the galaxy (Bialas et al., 2015). Furthermore, the group environment has been shown to be very effective at causing morphology changes in satellite galaxies (Villalobos et al., 2012).

Several studies have reported on the importance of group pre-processing in building up the current quenched satellite population in massive clusters. van den Bosch et al. (2008) study central and satellite galaxies in groups, and find that ~ 70 per cent of red satellite galaxies at $M_* \sim 10^9$ $\mathrm{M}_\odot$ quenched as satellites in groups, rather than being quenched already at the time of accretion. This fact, however, does not hold in larger haloes such as clusters. In fact, a significant portion of cluster galaxies were accreted via smaller haloes, meaning many $z = 0$ cluster satellites began to quench in a different halo than they one they are currently in. McGee et al. (2009) find that present-day clusters $\left(M_h \gtrsim 10^{14.5}\ \mathrm{M}_\odot\right)$ accrete ~ 40 per cent of galaxies through $M_h \gtrsim 10^{13}$ $\mathrm{M}_\odot$ haloes. Noting the fact that cluster cores at high redshift contain bluer galaxies than at present day (the Butcher-Oemler effect, Butcher and Oemler, 1978), McGee et al. (2009) interpret these results as evidence that the environmental processes that induce quenching in satellites must begin

in $10^{12} - 10^{13}$ $M_\odot$ haloes, and subsequently operate over timescales of > 2 Gyr. Furthermore, Bianconi et al. (2018) show that, binned by cluster-centric radius, there are generally fewer star-forming galaxies in groups which are infalling to clusters compared to the other cluster galaxies. These results are supported by Wetzel et al. (2013) who use N-body simulations to track satellite orbits. They find that current satellites experienced their first infall into any halo around ~ 5 Gyr ago. It is shown that the fraction of satellite galaxies that quenched in their current halo is as high as ~ 70 per cent for group-sized haloes, and as low as ~ 30 per cent for more massive haloes, further indicating the importance of groups in the evolution of satellites. Additionally, it is found that after first infall, satellites remain actively star-forming for $2 - 4$ Gyr, and then quench quickly (< 0.8 Gyr). Similarly, Donnari et al. (2021) find, through the use of the IllustrisTNG suite of hydrodynamical cosmological simulations, that virtually all $z = 0$ satellites that were accreted into their current halo $\gtrsim 4 - 6$ Gyr ago are now quenched. These results are consistent with a 'delayed-then-rapid' model of satellite quenching (Wetzel et al., 2013), with strangulation (Balogh et al., 2000) being a possible mechanism as described earlier. Moreover, the quenched fraction of satellites in massive $\left(M_{200} > 10^{13}\ M_\odot\right)$ haloes decreases as a function of increasing redshift, with > 80 per cent of satellites being quenched at $z = 0$ and as few as ~ 10 per cent of 10^{10} $M_\odot$ satellites being quenched at $z = 3$ (Donnari et al., 2021). These results taken together are a manifestation of a) the time it takes for a galaxy to fall in to a halo, and b) the time it takes to quench (see McGee et al., 2009).

1.2.4 External mechanisms: Mergers

Galaxies, especially when they reside in a high-density environment, can sometimes interact with other galaxies in a violent, disruptive event called a merger. This is when the gravitational forces between two or more galaxies are so strong that the galaxies become structurally deformed, to the point of colliding and forming one galaxy (Toomre and Toomre, 1972). Two examples of merging

systems are shown in Figure 1.5. In the top panel, we see a *Hubble Space Telescope* image of NGC 4676, or the Mice Galaxies. The two galaxies interacting in this system are spiral galaxies, with striking blue colours, particularly in the tails. These galaxies are likely members of the Coma Cluster. The bottom panel shows a *Hubble Space Telescope* image of NGC 4038 and NGC 4039, or the Antennae Galaxies. These galaxies are currently colliding and undergoing a starburst phase. The catastrophic nature of mergers is clearly evident here.

Mergers are typically characterised by the mass ratio μ of the two systems, with a 'major' merger usually referring to one with a mass ratio of between 1:1 and 4:1, and a 'minor' merger referring to anything with a larger mass ratio. Major mergers are, of course, much more disruptive and bring about more significant changes to the galaxy than minor mergers. That said, major mergers are rare, and so don't contribute significantly to the build-up of the present-day quenched population of galaxies (compared to repeated minor mergers, Naab and Ostriker, 2017). Nevertheless, determining the nature and rate of mergers is necessary to disentangle feedback processes and outflows, and understand how the morphology of galaxies can change. Early papers used simple analytical models (Lacey and Cole, 1993) and simulations (Kauffmann et al., 1993) to determine merger rates, and to study the behaviour of gaseous inflows and the subsequent starburst (Mihos and Hernquist, 1996). Today, simulations and observations are more sophisticated, such that mergers can be tracked and analysed more rigorously. The merger rate $\mathcal{R}$ as a function of redshift has been determined to be proportional to $(1+z)^m$, with $m \sim 0.8 - 1.8$ in observations (Mantha et al., 2018; Duncan et al., 2019) and $m \sim 2.4 - 2.8$ in simulatons (Rodriguez-Gomez et al., 2015; Ferreira et al., 2022).

Mergers are known to have profound effects on the gas content, star-formation, and morphology of the galaxy. The merger can result in increased gas densities, inducing a starburst. This appears to be the case in a $z = 1.395$ galaxy, which shows a compact region of star-formation, indicative of a merger, with SFR = 550 ± 10 $M_\odot$ yr^{-1} (Puglisi et al., 2021). A massive outflow of gas was detected from this galaxy, amounting to 46 ± 13 per cent of the molecular gas of the



(a) The Mice Galaxies. Visible are long tidal tails caused by the gravitational forces of the interacting galaxies. By NASA, H. Ford (JHU), G. Illingworth (UCSC/LO), M.Clampin (STScI), G. Hartig (STScI), the ACS Science Team, and ESA.



(b) The Antennae Galaxies. The disruption of stars, gas, and dust are very clear. By ESA/Hubble.

Figure 1.5: Some examples of merging galaxies.

galaxy, or $M_{\rm out} = 2.0 \pm 0.5 \times 10^{10} \mathrm{M}_{\odot}$. Given the luminosity of the AGN in this galaxy, the outflow mass rate is $\sim$ 2 orders of magnitude above what it should be from scaling relations. Similarly, if attributed simply to starburst-fuelled outflows, an outflow of this size would suggest an SFR $\geq 1.4 \times 10^4$ $\mathrm{M}_{\odot}$ yr^{-1} from scaling relations, which is unphysical for a singular galaxy. Thus, the outflow is explained as being driven by tidal flows from the merger. It is clear to see, from the magnitude of the outflow and the SFR, that this galaxy will quench soon.

The galaxy from Puglisi et al. (2021) is an extreme but illustrative example of how a merger can induce a starbust and subsequently quench a galaxy. However, there are conflicting reports in the literature about how efficiently mergers can reduce star-formation. For example, Pearson et al. (2019) uses a convolutional neural network to identify mergers and non-mergers in various imaging surveys, and compares the SFRs of the merging and non-merging galaxies. They find only a minor difference in the SFR between merging galaxies and non-merging galaxies, which seems in tension with the hypothesis that mergers can induce a starburst and then quench a galaxy. However, what is missing from this study is any sense of the timescales involved in the merging process. As merging is a slow process, and the quenching takes place after the starburst, direct observational evidence of merger-induced quenching is difficult to obtain. Simulations focused on merger-based quenching mechanisms, however, find significant links between major mergers and increased SFR (Rodríguez Montero et al., 2019) and are able to successfully reproduce observed quenched populations (Gabor et al., 2010). A favoured explanation of how mergers can cause quenching is by the merger inducing an AGN. Satyapal et al. (2014) study AGN in galaxy pairs, and find an increased fraction of AGN in galaxy pairs compared to a matched control sample of isolated galaxies. Additionally, they find that the fraction of AGN increases as a function of decreasing separation between the galaxies. They also find that the AGN in galaxy pairs exhibit higher luminosities than those in the control sample, with the most luminous AGN being found in post-mergers. A later study of dual and offset AGN (Comerford et al., 2015) agrees with these results; they find that 4 out of 6 confirmed dual/offset AGN (of 12 candidates) are located in galaxies currently experiencing major mergers, and these

AGN are on average 10 times more luminous than the single AGN in their sample.

Despite these convincing results, there are still discrepancies in the literature. Villforth et al. (2014) investigates the morphologies of AGN galaxies at $z \sim 0.7$, in search of merger or post-merger signatures. They find no significant differences between the asymmetries of AGN galaxies and of control galaxies in general, nor as a function of luminosity. Even in the highest luminosity bins, where studies described above find the strongest links between mergers and AGN activity, Villforth et al. (2014) find little significant evidence to connect mergers to AGN. This may, once again, be a manifestation of the timescales at play, where merger signatures remain evident for $\sim$ Myrs to $\sim$ 1 Gyr. This, however, would likely still result in elevated AGN incidence in this study, as the time delay between starburst and AGN activity is $\sim$ 100 Myr (Di Matteo et al., 2005; Hopkins et al., 2006). Another possibility is that this study misses the most obscured AGN which may be related to an early stage in the merger cycle (see Satyapal et al., 2014). Nevertheless, the difficulty lies in capturing a complete sample of AGN at different stages of a merger, and in consistently identifying mergers and their signatures. By implementing more sophisticated techniques such as machine learning with a convolution neural network to identify post-merger systems, it is easier to distinguish between star-forming systems and merging systems, even among asymmetric galaxies. Ferreira et al. (2022) develop a pipeline to achieve this based on the IllustrisTNG suite of simulations, and find evidence that merging systems, compared to star-forming galaxies, exhibit a morphological transition from disk to bulge-dominated.

It is clear from the above that, while mergers do not contribute a significant amount to the global star-formation budget nor to quenched galaxies at $z \sim 0$ (Weigel et al., 2017), their role and connection to AGN must not be neglected. Smethurst et al. (2022) also note that AGN properties between merging galaxies and non-merging galaxies are consistent with each other, implying consistent secular evolution may take place during the long timescales between occurrences of mergers. In any case, the link between the aftermath of mergers and AGN feedback is challenging to disentangle.

1.3 Superluminous supernovae

1.3.1 Classification

A class of supernovae $10-100$ times brighter than typical supernovae was first noted by Richardson et al. (2002), noting such events were rare (fraction < 0.01). Extensive study of so-called 'superluminous' supernovae (SLSNe) followed, and originally culminated in a review (Gal-Yam, 2012) which classified an event as being superluminous if it had an absolute magnitude of $M < -21$. However, over the course of the last decade, it has become clearer that a magnitude/luminosity threshold is not enough to be representative of the SLSNe class (De Cia et al., 2018). Note that SLSNe are split into two groups, Type I and Type II, depending on the lack or presence of hydrogen in their spectra respectively. This is analogous to typical SNe, however there are differences between the mechanisms that power each of these classes of events. That said, the rest of this section will only focus on SLSNe-I (hereafter simply SLSNe), as SLSNe-II are not relevant in this work.

The bolometric lightcurves of SLSNe have unique shapes that make them distinct from other SNe. They have longer rise times and decay times (Nicholl et al., 2015b; De Cia et al., 2018), and sometimes exhibit 'bumps' both pre-peak and post-peak. Nicholl and Smartt (2016) found that early bumps can last for ~days to weeks, and are typically brighter than normal SNe, and sometimes even are comparable to the peak luminosity of the SLSN (Gal-Yam, 2019). Pre-peak bumps are, at least, very prevalent (Nicholl and Smartt, 2016). As for post-peak bumps, Nicholl et al. (2016b) noted bumps in SN 2015bn occurring up to $\sim$ 100 days after the peak. Such bumps have been seen in other events (Inserra et al., 2017), although it is difficult to know conclusively the nature of these bumps without long timescale observations of SLSNe post-explosion.

At peak luminosity, the spectra of SLSNe are very blue, indicating very high temperatures of 20,000 K (e.g. Bose et al., 2018). There are also very notable OII absorption lines (Quimby et al., 2018), which are unique to SLSNe.

After peak, temperatures cool and the spectrum evolves to strongly resemble that of a typical SN Ic (Nicholl, 2021). In fact, there have been several studied events which appear to be similar to both SLSNe and SNe Ic. In the days before SLSNe were even classed as a distinct type of event, Pastorello et al. (2010) noted that SN 2010gx showed a blue continuum and OII absorption lines, which we know now are consistent with SLSN classification. At late-times, the lightcurve resembles more that of a SN Ic. Similarly, (Gomez et al., 2021d) present a study of SN 2019stc, which they classify as a SN Ic. They note that the spectrum of this event lacks the blue continuum found in SLSNe and is consistent with typical SN Ic spectra, but the peak luminosity of SN 2019stc is much brighter than other SNe Ic, although not quite as bright as SLSNe. Furthermore, the lightcurve of this event has two prominent peaks. The authors suggest that a combination of a magnetar, radioactive decay, and circumstellar material (CSM) interaction power this supernova (these possible power sources will be explained in Section 1.3.2), with the first peak being caused by the magnetar and the radioactive decay, and the CSM interaction causing the second peak. Gomez et al. (2021d) call this event a 'transition' object between SNe Ic and SLSNe.

1.3.2 Possible energy sources

SLSNe differ from normal SNe by the fact that they are not powered by radioactive decay of ^{56}Ni (Nicholl et al., 2014). The masses required to reproduce the energy seen in SLSNe are unphysical. Thus, there are two power sources which are favoured; a combination of these is also plausible.

It is thought that a rotating neutron star with a strong magnetic field, known as a magnetar, could provide the energy required for SLSNe (Woosley, 2010). Attempts to model observed lightcurves and spectra using magnetars as a power source have been fairly successful (e.g. Dessart et al., 2012; Inserra et al., 2013; De Cia et al., 2018). However, this model does not fully capture all the features of a SLSN. The magnetar model cannot explain the bumps seen pre-peak and post-peak (Nicholl et al., 2015a, 2016b), thus another mechanism is likely to also contribute to produce these

features.

Interaction with CSM blown away from the star pre-explosion is another process that is considered to be powering SLSNe. Other SNe also show signatures of such interaction, through various absorption lines in their spectra. Interaction with CSM can potentially explain at least some of the bumpiness seen in SLSN lightcurves (although a combination of mechanisms remains plausible, see Nicholl et al., 2016a). Hosseinzadeh et al. (2022) employ a CSM model on a sample of SLSNe exhibiting late bumps, and constrain $M_{\rm CSM}$ to be $\sim 0.1 M_\odot$ at a distance of $\sim 10^5$ $R_\odot$. However, they cannot rule out a magnetar-powered model. Fiore et al. (2022) analyse the photometry and spectroscopy of SN 2018hti. They also attempt to constrain the CSM mass, and the properties of a possible magnetar. They find that 8 $M_\odot$ of ejecta may be interacting with ~ 10 $M_\odot$ of CSM, or, that a magnetar with magnetic field $B \sim 1.3 \times 10^{13}$ G and a period $P \sim 1.8$ ms could be powering the SN.

It is clear that there is a wide diversity of events within this class, with many edge-cases emerging and muddling the picture further. Blanchard et al. (2021) present analysis of the SLSN SN 2016inl. The spectrum of this event is similar to that of PS1-14bj, which appears consistent with a pair-instability supernova (PISN). However, due to the behaviour of the lightcurve at late-times, the authors rule of the possibility of a PISN. Instead, the decline in the lightcurve may be explained by the spin-down of a magnetar, following a power-law: $L \propto t^{-2.8}$. With this model, an unusually large ejecta mass is found (~ 20 $M_\odot$). The event SN 2019stc (Gomez et al., 2021d) was discussed above, and was found to be a 'transition' object between SNe Ic and SLSNe. Nevertheless, the near future will allow for high-cadence observations of SLSNe, via the LSST at Vera Rubin Observatory, which will help uncover the mysterious mechanisms that power these events.

1.3.3 Rates of SLSNe

These explosive events are extremely rare; only $\sim$ 100 classified events have been detected. By simulating SNe and comparing to observations, Frohmaier et al. (2021) compute volumetric rates for core-collapse supernovae (CCSNe), stripped-envelope supernovae (SESNe), and SLSNe. They find that, at a mean redshift of $\langle z \rangle = 0.028$, CCSN occur at a rate of $r_v^{\rm CC} \approx 9 \times 10^{-5}$ yr^{-1} Mpc^{-3} h_{70}^3. For SESNe, they find the volumetric rate $r_v^{\rm SE}$ to be $\lesssim 0.3\ r_v^{\rm CC}$. On the other hand, the inferred rate of SLSNe at $\langle z \rangle = 0.17$ is estimated to be $r_v^{\rm SLSN} \approx 3.5 \times 10^{-8}$ yr^{-1} Mpc^{-3} h_{70}^3. This means that, for 1 SLSN, there should be $\sim$ 3500 CCSN, or $\sim$ 810 SESN. When looking only at the host galaxy stellar mass bins where SLSNe occur, i.e. $\log M_*/{\rm M}_\odot < 9.5$, this ratio increases to approximately 1/1700 and 1/300 for CCSN and SESN, respectively. This further exemplifies the importance of upcoming high-cadence, wide-field surveys such as LSST for understanding the physics of SLSNe.

1.3.4 Host galaxy properties

Direct observations of SLSN host galaxies are challenging, as these events usually occur in faint dwarf galaxies. That said, more and more studies of individual SLSN hosts, and of samples of hosts, are emerging. These studies show that SLSNe are found in galaxies with $\log M_*/{\rm M}_\odot \lesssim 9.5$, high specific star-formation rate, and that SLSNe favour low-metallicity environments with $Z \lesssim 0.4\ Z_\odot$ (Lunnan et al., 2014; Chen et al., 2015; Perley et al., 2016b; Gomez et al., 2021d; Schulze et al., 2021). Still, some outliers remain; for example, SN 2017egm occurred in a spiral galaxy, with a stellar mass of $\log M_*/{\rm M}_\odot \approx 10.5$ (Chen et al., 2017b). The SLSN occurred in an environment with metallicity $Z = 2.6\ Z_\odot$, which is the highest metallicity detected of any SLSN. Such events pose a challenge to the understanding of the mechanisms behind SLSNe.

There is evidence that suggests some SLSNe could arise because of interactions between their host galaxy and other galaxies, leading to a starburst. By examining spatially resolved

observations of the SLSNe PTF 11hrq and PTF 12dam, Cikota et al. (2017) find that both host galaxies are likely interacting with a nearby companion, due to starburst regions within the galaxies and disrupted morphologies. Chen et al. (2017a) perform similar analysis on the SLSN LSQ14mo, and find their results are consistent with an interacting galaxy system, which could explain the increased star-formation in the region of the SLSN. The host galaxy environments of SLSNe will be investigated further in Chapter 4.

1.3.5 Links with gamma-ray bursts

There is an uncertain connection between SLSNe and long GRBs (LGRBs). LGRBs generally occur in galaxies with high star-formation rates, and are associated with CCSNe (Woosley and Bloom, 2006). Similarly, Lunnan et al. (2014) find that LGRBs and SLSNe are found in roughly similar host galaxies. Although, the host galaxies of SLSNe have lower stellar masses than those of LGRBs, and thus lower metallicities (Angus et al., 2016). Schulze et al. (2018) find that the cut-off for metallicity for SLSN hosts is ~ 0.4 dex lower than for LGRBs. SLSNe are found to be less clustered in the brightest regions of galaxies compared to LGRBs, which Lunnan et al. (2015) interpret as evidence for lower-mass progenitors of SLSNe than of LGRBs.

Ultra-long GRBs are rare events, lasting $10^3 - 10^4$ s (Levan et al., 2014). One of the hypothesised mechanisms behind these mysterious events is a magnetar (Ioka et al., 2016), which may be responsible for SLSNe as discussed above. Greiner et al. (2015) reports on SN 2011kl, a normal supernova that exhibits some traits similar to a SLSN, which has an associated ultra-long GRB 111209A. They also hypothesise that a magnetar could explain the behaviour of this event.

1.4 Outline of thesis

This thesis is outlined as follows: Chapter 2 describes a study on environmental quenching; Chapter 3 describes a study on AGN variability; Chapter 4 describes a study on superluminous supernova host galaxies; finally, Chapter 5 summarises and concludes the material covered in this thesis.

Chapter Two

Environmental galaxy quenching

This Chapter contains the paper "The environmental dependence of rapidly-quenching and rejuvenating galaxies" (Cleland and McGee, 2021), published in MNRAS. In the original paper, the terminology ‘transient galaxy’ was used, however in this thesis, the term ‘recently-quenched galaxy’ is adopted to avoid confusion with stellar transients.

By combining Hα flux measurements from the Sloan Digital Sky Survey (SDSS) with UV flux observations from the Galaxy Evolution Explorer (GALEX), we examine the environmental dependence (through central/satellite distinction) of the rapid quenching and rejuvenation of galaxies. Hα emissions trace the most massive stars, thereby indicating star-formation on timescales of $\sim$ 10 Myr, while UV emission traces star-formation on timescales of $\sim$ 100 Myr. These varying timescales are exploited to probe the most recent star-formation histories of galaxies. In this work, we define a class of recently-quenched (RQ) galaxies which have UV emission typical of star-formation but negligible Hα emission. We find that the occurrence of these RQs has a strong stellar mass dependence in both the satellite and central population. However, while at stellar masses greater than $M_* \sim 10^{10}$ M$_\odot$ they occur with equal frequency regardless of environmental class, at lower stellar masses they are more common in satellites only, with an excess of about 1 percentage point across all low stellar mass galaxies. These satellite RQs also have a strong halo

mass and group-centric radial dependence suggesting they are driven by an environmental process. Finally, we select a sample of galaxies with Hα emission but not UV emission which could contain short-timescale rejuvenating galaxies. These rejuvenating candidates are few in number and do not have a strong difference in their occurrence rate in centrals or satellites. These unique probes point to an environmental quenching mechanism which occurs on short timescales after the satellite has been in the group environment for a significant time – consistent with 'delayed-then-rapid' quenching.

2.1 Introduction

It has been established that the distribution of colours of galaxies is bimodal, with star-forming galaxies belonging to the 'blue cloud' and quiescent galaxies belonging to the 'red sequence' (Strateva et al., 2001; Bell et al., 2004). The redshift evolution of galaxy populations suggests that the quenching of star-formation is the likely process which moves a galaxy from the blue cloud to the red sequence (Baldry et al., 2004; Faber et al., 2007). However, there are many separate physical mechanisms that may be contributing to the reduction and cessation of star-formation in a galaxy. These mechanisms are often broadly classed as internal or external processes.

Internal processes refer to those that occur due to the individual galaxy properties, such as morphology or the presence of an AGN. Morphological quenching may either prevent star-formation from taking place, such as with the presence of a bulge which may prevent the collapse of the disc and the formation of stars (Bluck et al., 2014), or accelerate gas consumption, whereby the presence of a bar directs material to the centre of the galaxy (Athanassoula, 1992) where it is depleted more efficiently thus leading to a reduced SFR (Zurita et al., 2004; Sheth et al., 2005). Alternatively, a galaxy with an AGN may experience feedback which provides heat to the surrounding gas, preventing star-formation (Fabian, 2012; Smethurst et al., 2017).

External processes are those where the environment of a galaxy is relevant. These include mergers, which may violently heat and expel gas, and are also often responsible for morphological changes to a galaxy (Gabor et al., 2010). Ram-pressure stripping occurs when a galaxy encounters gas upon infall to a group or cluster, causing its cool gas to be stripped away (Gunn and Gott, 1972). Ram-pressure stripping results in a relatively quick depletion of gas, operating at a fraction of cluster crossing-time timescales ($\sim 10^7$ yrs, Abadi et al., 1999). A galaxy will quench its star-formation on gas consumption timescales if it fails to accrete additional cool gas through either the removal of the gas reservoir (e.g. 'strangulation', Balogh et al., 2000) or the cutting off of cosmological accretion (e.g. 'overconsumption', McGee et al., 2014).

It is not trivial to discern which of these internal or external processes are dominant (if any) for a given galaxy as they are heavily related and dependent on each other. One way to determine if internal or external processes are dominant is by examining the galaxy properties as a function of their environment. If a particular property has no environmental dependence, then it is likely driven by internal mechanisms, and alternatively, a strong environmental dependence is indicative of a strong external mechanism. There is clear evidence that local environment of a galaxy has a prominent effect on its star-formation rate. In addition to a well-documented morphology-environment correlation (Dressler, 1980), it has been shown that satellite galaxies in a group or cluster exhibit an increased fraction of quenching compared to galaxies at the centre of the group or cluster or isolated field galaxies (e.g., McGee et al., 2011; Wetzel et al., 2012; Ziparo et al., 2014). However, evidence for the regimes in which internal or external mechanisms dominate is not yet clear. One promising avenue for further elucidation of this is to examine the locations and abundances of galaxies currently undergoing rapid quenching.

Much of the work on rapidly quenching galaxies has been done using the class of galaxies called E+A or post-starburst galaxies. These were first discovered by Dressler and Gunn (1983) who found three galaxies within a galaxy cluster with very strong Balmer absorption lines. Using stellar population modelling, those authors suggested these galaxies resulted from a burst of star-formation

($\sim$ 20 per cent of the total stellar mass formed within 10^8 yrs), and later became quenched. This early identification and interpretation has led to their synonymous identification as 'post-starburst' galaxies. Later work focused on the occurrence of these galaxies in clusters, and their classification standardized into requiring the non-existence of a current star-formation indicator ([OII] in early studies) along with the strong Hδ absorption. It has been clear since the early days, when the proportion of cluster galaxies classified as E+A's varied from $\sim$ 30 per cent to 2 per cent (Couch and Sharples, 1987; Poggianti et al., 1999; Balogh et al., 1999), that the relatively small sample sizes of E+A's combined with their sensitive dependence on the details of the target selection, spectroscopic reduction and parameter estimation, could have a big impact on the interpretation. These uncertainties have continued, and the literature is unsettled on many of the major questions about E+A environmental dependencies (Zabludoff et al., 1996; Paccagnella et al., 2019; Owers et al., 2019), morphological composition (Pracy et al., 2009; Swinbank et al., 2012; French et al., 2016) and triggering mechanisms (Zabludoff et al., 1996; Bekki, 2014; Yesuf et al., 2014; Pawlik et al., 2019; Vulcani et al., 2020).

In this study, we begin a fresh look at the question of rapidly quenching galaxies by selecting them in a new way – using a combination of UV emission and Hα emission. Although some studies have examined the UV properties of previously selected E+A galaxies (Kaviraj et al., 2007; Melnick and De Propris, 2013), to our knowledge, this is the first time where the primary selection of the rapidly quenching galaxies has been made using UV with spectral diagnostics. Our method has the benefit of being sensitive to shorter timescales of star-formation than the traditional E+A method, and thus may allow a better pinpointing of the quenching driver. We will constrain the timescale of the quenching processes by determining the recent star-formation history (SFH) of each galaxy. To do this, we define a 'recently-quenched' galaxy (RQ) as one that has a star-forming UV component but a lack of Hα. Hα traces young O-type stars, which typically have a lifetime of about 10 Myr, while UV traces O- and B-type stars, where the latter typically lives for $\sim$100 Myr. This disparity means that a lack of Hα measurements implies star-formation has ceased less than $\sim$100 Myr ago.

Due to the sensitivity of these star-formation tracers to stars of different masses, this method allows us to investigate the short timescale differential SFR of galaxies in the process of quenching.

Using this new classification of galaxy, we will attempt to isolate the internal/external mechanisms by examining the differential effects of quenching on the environment of the galaxy and by characterizing the timescale over which the cessation of star-formation occurs. We define 'environment' as the location of the galaxy in its host dark matter halo. Central galaxies are the galaxies that have the most stellar mass in their local potential and are often assumed to be located in the center of the dark matter halo. By this definition, central galaxies contain both the dominant galaxy in a group or cluster as well as an isolated galaxy in the 'field'. Galaxies which appear gravitationally bound to a halo in which they are not the dominant galaxy are called 'satellites'.

Subsequently, the properties of each satellite and how it relates to its group may be investigated to probe the effects of the immediate environment of the satellite. For this work, we consider the group-centric radial position of satellite galaxies, and the relative velocity of the satellite to the central galaxy. Combining all these data, we aim to discern the dependencies of these quenching processes and which, if any, are dominant.

The data used for this work will be described in Section 2.2. The results will be presented and explained in Section 2.3. There will be a discussion of the results in Section 2.4, and finally, our work will be summarised in a conclusion in Section 2.5. Throughout this work we adopt the following cosmological parameters: $H_0 = 72\,\mathrm{km\,s^{-1}\,Mpc^{-1}}$, $\Omega_\Lambda = 0.7$, $\Omega_\mathrm{M} = 0.3$. We assume a Kroupa IMF (Kroupa, 2001).

2.2 Data

Our sample is derived from the set of galaxies with spectroscopic measurements in the Sloan Digital Sky Survey (SDSS) Data Release 7 with $0.01 < z \leq 0.2$ (Abazajian et al., 2009). Although more recent data releases are available from SDSS, this version contains several 'value-added' catalogues which we use. For each galaxy, we use the survey completeness correction given by Blanton et al. (2005) to mimic a complete, flux-limited sample to the depth of the SDSS spectroscopic catalogs. Further, we use the volume corrections calculated by Omand et al. (2014)[1] to ensure selection effects do not significantly bias our results. For each galaxy, we compile the stellar mass ($M_*/\mathrm{M}_\odot$), Hα flux (non-corrected for stellar absorption, [erg s^{-1} cm^{-2}]) and equivalent width (EW [Å]) from the MPA-JHU value added catalogs (Brinchmann et al., 2004)[2].

The UV emission measurements are taken from the GALEX-SDSS-WISE Legacy Catalog Medium-Deep 2 (GSWLC-M2) (Martin et al., 2005; Morrissey et al., 2007; Salim et al., 2016, 2018)[3][4]. For our purposes, this catalogue provides well-matched GALEX photometry to the SDSS spectroscopic galaxy sample. The GALEX satellite provided photometry in both the Near Ultraviolet (NUV; 2300 Å) and Far Ultraviolet (FUV; 1500 Å). Although the FUV is a cleaner probe of the recent star-formation rate in local galaxies, there are many more measurements of galaxies in the NUV due to a failure of the FUV instrument. We will use NUV as our ultraviolet probe in this paper, but we note that we have explored using FUV instead and find no qualitative change in our results except for a reduction in the statistical power. After matching our galaxy sample and its associated stellar mass and Hα measurements to the GSWLC-M2, and removing galaxies with flagged photometry or non-detections (e.g. flux in Hα or UV < 0), we are left with a sample of 227,176 galaxies with Hα and UV coverage. Note that the fraction of removed galaxies

[1] http://cdsarc.u-strasbg.fr/viz-bin/cat/J/MNRAS/440/843

[2] https://wwwmpa.mpa-garching.mpg.de/SDSS/DR7/

[3] http://pages.iu.edu/~salims/gswlc/

[4] http://galex.stsci.edu/GR6/

due to poor NUV observations is about 2 per cent across all stellar mass bins, with a slight increase towards the highest mass bins.

The GALEX observations which go into the GSWLC-M2 catalog have variable exposure times across the different pointings in the range of 650 to 4000 seconds in the NUV band (Salim et al., 2018). Thus the flux limit also varies across these pointings. However, within the footprint of the GALEX observations, essentially all SDSS galaxies with $r < 16$ are detected. For blue galaxies ($u - r < 0.8$), this universal detection remains until past the $r = 17.7$ limit of the SDSS main spectroscopic sample. For red galaxies ($u - r > 0.8$), 75 per cent of them are detected at $r = 17$, while about 50 per cent are detected at 17.7. Thus, our catalog is missing some red SDSS spectroscopic galaxies at the limit of the survey. To overcome this, when we rely on detections of low star-formation rates in UV, we reduce the redshift limit of the sample to $z = 0.1$, where we are nearly complete.

Distances are calculated assuming the redshift is dominated by the Hubble flow, and these distances are used to compute luminosities from the fluxes. Star-formation rates (SFR /$M_\odot$ yr^{-1}) and specific star-formation rates (sSFR /yr^{-1}) are computed using Hα and NUV flux calibrations from Kennicutt (1998a) as in Equations 2.1 and 2.2.

$$\mathrm{SFR}_{\mathrm{H}\alpha} = 7.9 \times 10^{-42} L_{\mathrm{H}\alpha} [\mathrm{erg\ s^{-1}}], \tag{2.1}$$

$$\mathrm{SFR}_{\mathrm{UV}} = 1.4 \times 10^{-28} L_{\nu} [\mathrm{erg\ s^{-1} Hz^{-1}}]. \tag{2.2}$$

Note that these calibrations are for a Salpeter IMF (Salpeter, 1955), but we correct them to a Kroupa IMF (Kroupa, 2001) by multiplying the SFR by 1.5. It should be noted that our results are not sensitive to the exact form of these calibrations as we are principally interested in the differential change between environments and our divisions between 'star-forming' and 'passive' are motivated by empirical divisions in the observed data. For all our results, the galaxies are weighted by the completeness and volume corrections from Blanton et al. (2005) and Omand et al. (2014). The statistical errors are calculated using raw data.

We obtain 221,904 petrosian magnitudes across all SDSS bands u, g, r, i, z (Doi et al., 2010) and match these to emission line data and stellar masses in order to produce a colour magnitude diagram with star-formation information. These magnitudes satisfy a redshift limit $z < 0.2$ and magnitude limit $u < 20$.

Our environmental (central/satellite) classifications come from the Yang et al. (2007) group catalogue (hereafter YGC). In the YGC, galaxies were assigned to groups via the friends-of-friends algorithm and the groups were assigned a total mass by rank-ordering the total luminosity (or stellar mass) of the group members, for a given comoving volume and halo mass function. This rank-ordering ensures that the halo mass function for a given cosmology is consistent with the total masses in the groups. The most luminous or the most massive (in terms of stellar mass) galaxy in a group is considered the central galaxy, while the remaining galaxies are denoted as satellites. Again, note that this means ungrouped, or isolated, galaxies are by definition also central galaxies. For this study, we assume a central galaxy is the one with the most stellar mass.

From the YGC, we obtain the satellite/central classification for each galaxy and the total mass of the halo (M_h) that the galaxy resides in. For the galaxies which have appropriate Hα and UV coverage, we find a sample of 222,304 galaxies within the YGC.

For each group with redshift z_g, we can also calculate the group-centric halo radius r_{180} (Equation 2.3), defined where the dark matter halo has an overdensity of 180,

$$r_{180} = 1.26\ h^{-1}\ \mathrm{Mpc} \left(\frac{M_h}{10^{14}\ h^{-1}\ \mathrm{M}_\odot} \right)^{1/3} (1 + z_g)^{-1}, \tag{2.3}$$

and the effective line-of-sight velocity dispersion σ (Equation 2.4),

$$\sigma = 397.9\ \mathrm{km\ s^{-1}} \left(\frac{M_h}{10^{14} h^{-1}\ \mathrm{M}_\odot} \right)^{0.3214} \tag{2.4}$$

as in Yang et al. (2007). In this manner, we calculate the projected separation between each satellite galaxy and its central galaxy in terms of r_{180} of the group. We can use the redshift offset between

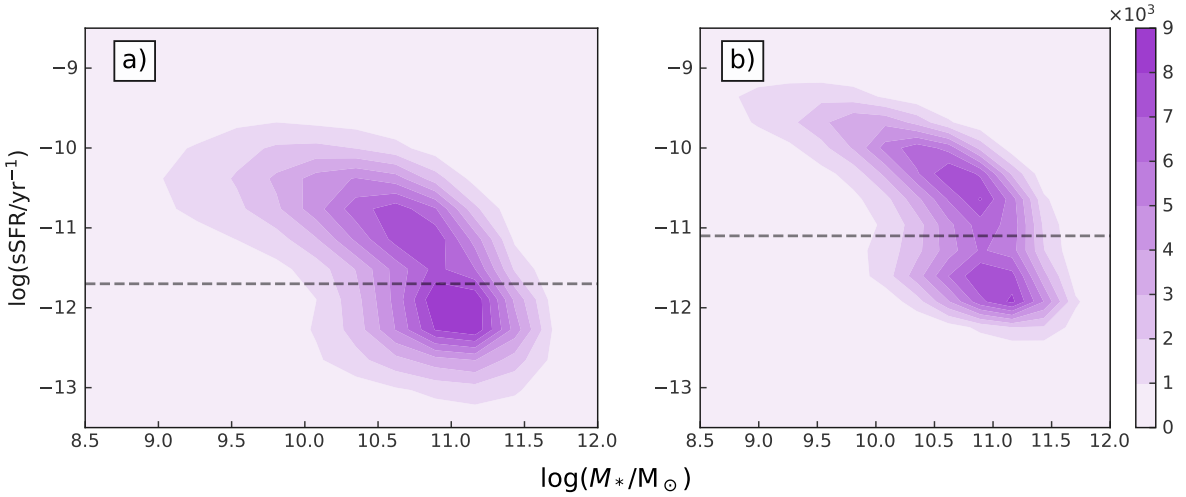


Figure 2.1: Stellar mass (M_*) versus specific star-formation rate [a) $\mathrm{sSFR_{H\alpha}}$; b) $\mathrm{sSFR_{UV}}$] distributions for all galaxies. Note the bimodality of the population: star-forming in the top portion of each panel and quenched in the bottom portion of each panel. The z-axis denotes number of galaxies in each bin, with contour lines indicating regions of equal numbers. The light purple regions signify no data.

the satellite and the group to calculate the relative velocity difference,

$$\Delta v = c(z_g - z_s). \tag{2.5}$$

In analysis, this is normalized as $\Delta v/\sigma$.

2.3 Results

2.3.1 Quenched galaxies

Although it is well established that 'quenched' or passive galaxies are strong functions of stellar mass and environment, we will first examine this same phenomenon in our sample. Our motivation is to establish the main trends, as well as examining their dependence on the star-formation tracer—

in particular Hα and UV. In Figure 2.1, we present the distributions of galaxies with respect to their stellar mass (M_*) and specific star-formation rate (sSFR), with SFR calculated using Hα in the left panel and SFR calculated using UV in the right panel. sSFR is calculated simply by dividing the star-formation rate by the current stellar mass and gives an indication of the star-formation the galaxy has with respect to its integrated past star-formation rate.

There are some obvious differences in the two panels of the figure which show the impact of SFR being calculated via Hα or UV flux which we will discuss after taking each in turn. In the $\mathrm{sSFR}_{\mathrm{H}\alpha}$ panel, there is a clear bimodality leading to two particular over-dense regions, one due to star-forming galaxies, and one due to quenched galaxies. Principally, by visual inspection, a dividing line between the two populations was chosen such that quenched galaxies have $\log(\mathrm{sSFR}/\mathrm{yr}^{-1}) < -11.7$, and star-forming galaxies are those above this cut-off. This cut-off is lower than some sSFR demarcations in the literature, such as Wetzel et al. (2012) who find that the trough in sSFR between star-forming and quenched galaxies in found at sSFR = 10^{-11} yr^{-1} when using Hα-based star-formation rates. However, it is important to remember that our Hα-based SFRs are not corrected for the effects of internal dust extinction.

In Appendix 2.A, we examine the relative effects of dust extinction on central galaxies and satellite galaxies, with respect to several properties of the galaxies (e.g., in stellar mass bins, halo mass bins, radial and velocity offset bins). We conclude that there is no difference in the attenuation effects between centrals and satellites in any of these subsamples. Since applying this attenuation correction would have no appreciable difference on the differential effects of centrals and satellites and thus no effect on our subsequent analysis, we do not apply it. This choice allows us to use Hα measurements for galaxies in which there is no Hβ measured, and maintains a clear connection to the massive stars responsible for Hα emission. We opt to retain a larger sample of galaxies with well-measured (SNR > 3) Hα (153,294 centrals, 37,811 satellites), compared to those with well-measured Hα and Hβ (125,346 centrals, 29,318 satellites). We assert the same line of thinking with regards to dust extinction of the UV, such that, since we are primarily interested in comparisons

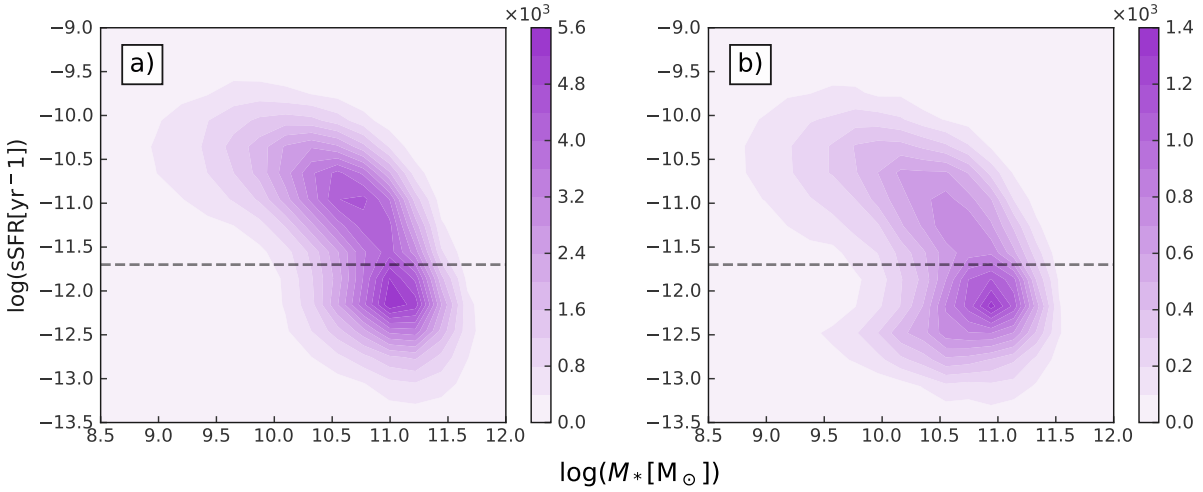


Figure 2.2: Stellar mass ($M*$) versus specific star-formation rate ($\mathrm{sSFR}_{\mathrm{H}\alpha}$) distributions for a) central galaxies and b) satellite galaxies. The grey dashed line signifies a) $\mathrm{sSFR}_{\mathrm{H}\alpha} = 10^{-11.7}$ yr^{-1} and b) $\mathrm{sSFR}_{\mathrm{UV}} = 10^{-11.1}$ yr^{-1}. The z-axis denotes number of galaxies in each bin, with contour lines indicating regions of equal numbers. The light purple regions signify no data.

between populations which should be equally affected by dust, corrections for extinction are not required.

Turning our attention to the right panel of Figure 2.1, we can see the distribution of galaxies in the $\mathrm{sSFR}_{\mathrm{UV}}$–stellar mass plane. It is clear that with this star-formation indicator, the bimodality is still apparent as in the Hα case. However, we note that the division in the bimodality is different to that in $\mathrm{sSFR}_{\mathrm{H}\alpha}$, and still not exactly equal to the common cut-off point in literature. Thus, we demarcate star-forming and quenched galaxies using a cut-off of $\log(\mathrm{sSFR}/\mathrm{yr}^{-1}) < -11.1$, chosen from the local minimum of the $\mathrm{sSFR}_{\mathrm{UV}}$ distribution of the sample. We can now investigate how the sSFR distribution varies with environment. In Figure 2.2, we present the galaxy distribution in the sSFR–stellar mass plane, where we measured the sSFR using Hα, for central galaxies (left panel) and satellite galaxies (right panel). There are interesting, but expected, differences between the environmentally separated populations. It is clear that the quenched population appears more prominent with respect to the star-forming population at all stellar masses in the satellite galaxies

than it does in the central galaxies. It is worth noting the relative lack of quenched galaxies with $M_* \lesssim 10^{10.5}$ M$_\odot$ in the central population, but their prominence in the satellite population. To have a more quantitative view of these distributions, we present Figure 2.3, in which we bin the data in stellar mass, and calculate the fractions of quenched galaxies with respect to the total number of galaxies, $f_q = N_q/N$, for centrals and satellites separately. Error bars are determined using the percent point function of a beta distribution where the input parameters are the number of quenched centrals (satellites) and the total number of centrals (satellites) in each mass bin (Cameron, 2011). At all stellar masses, there is a larger fraction of quenched satellite galaxies than quenched central galaxies, with a sharp increase for both centrals and satellites at around 10^{10} M$_\odot$. This supports the assertion that galaxies in dense environments such as satellites, and particularly high stellar mass galaxies, are more likely to be quenched. This general shape is consistent with many other studies of central/satellite quenched fractions in the literature (Kimm et al., 2009; Bluck et al., 2014; Davies et al., 2019). Note that our procedure of removing undetected NUV galaxies means that these fractions may suffer some incompleteness at the massive end, and thereby underestimate the quenched fraction. This removal of galaxies accounts for up to 8 per cent of quenched galaxies at the high-mass end. We have checked that imposing a redshift constraint of $z \leq 0.1$ does not qualitatively change our results.

2.3.2 RQ galaxies

Now that we have established the clear environmental trends in star-formation properties, and the implied quenching effect on satellite galaxies, we can attempt to pick out those galaxies which have recently undergone the cessation of their star-formation. As discussed in the introduction, Hα and UV measurements are sensitive to star-formation on different timescales (10 Myr and 100 Myr respectively), so a combination of the two measurements can be applied to investigate the differential star-formation rate. Consider a galaxy which has a star-formation rate typical of a star-forming

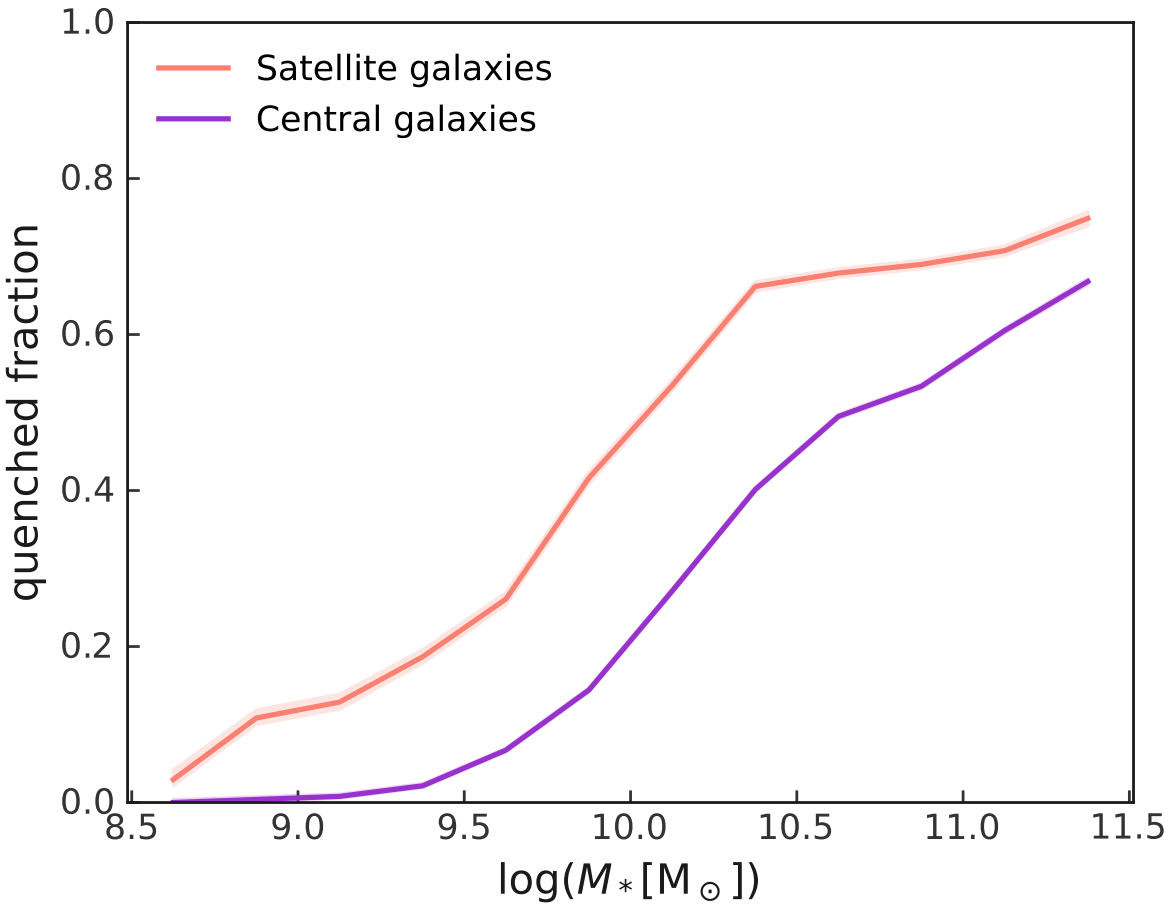


Figure 2.3: Fraction of quenched galaxies, $f_{\rm q} = N_{\rm q}/N$, where $N_{\rm q}$ is the number of quenched central(satellite) galaxies and N is the total number of central(satellite) galaxies. The star-formation rate is drawn from Hα.

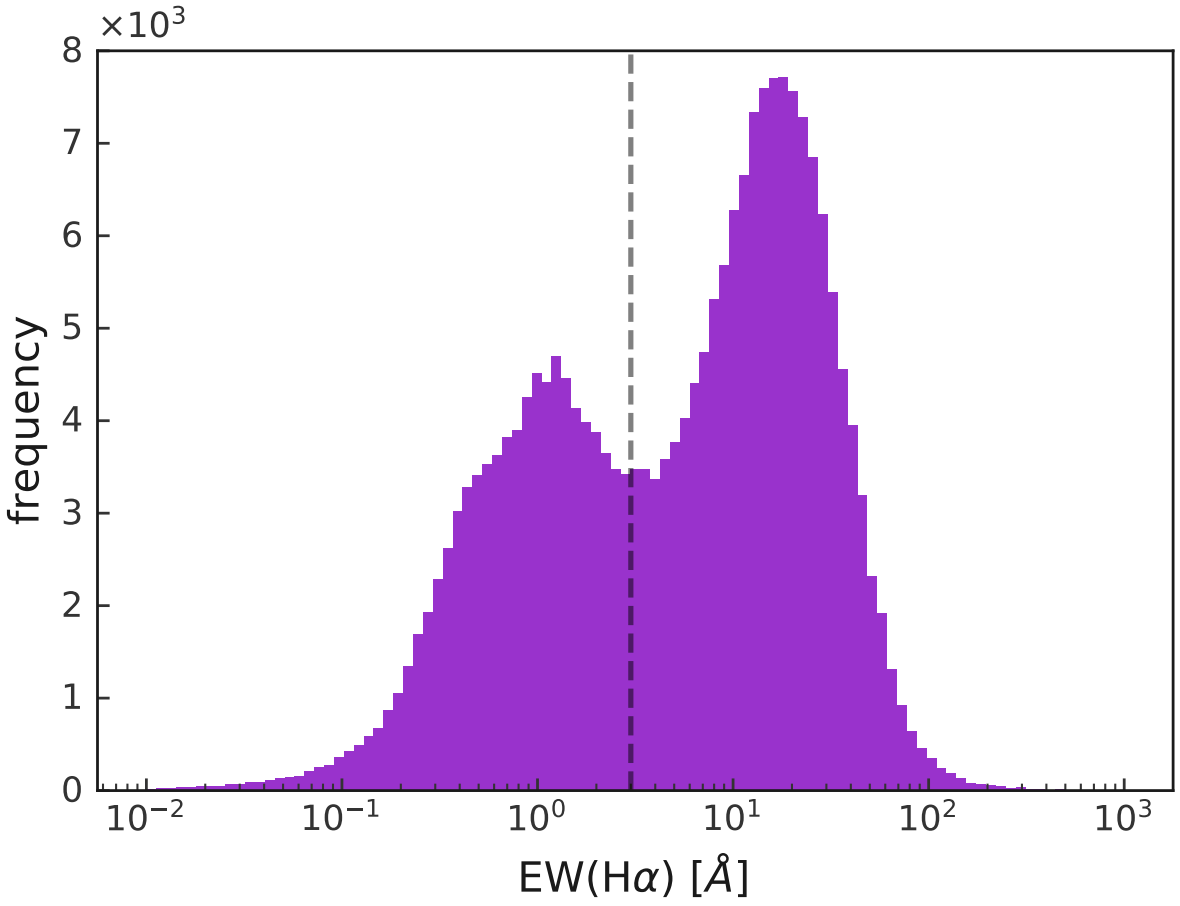


Figure 2.4: Distribution of equivalent widths of Hα measurements in angstroms. The black dashed line denotes EW(Hα) = 3Å.

galaxy. If this star-formation is shut off quickly in a semi-instantaneous event, the O stars giving rise to the Hα emission will die within 10 Myr and the galaxy will cease to appear star-forming in this tracer. However, as the UV emission comes from the less massive stars, the galaxy will appear to have significant UV emission until those stars die $\sim$ 100 Myrs after the extinction event. Thus, we can look for these recently-quenched galaxies by isolating those that have a star-forming UV component, but a negligible Hα component. To define these 'RQ' galaxies we must ensure that they have Hα flux consistent with no star-formation, and that the UV component must be from star-formation and not residual emission from old stars, and that this UV emission is significant.

First, to determine the galaxies with a lack of Hα emission directly, we plot a histogram of the distribution of the equivalent width (EW) of Hα in Figure 2.4. There are two clear populations: galaxies with a significant Hα detection, and galaxies with negligible Hα detection with a clear dividing line at EW(Hα) = 3Å. Galaxies below this cut are assumed to have no significant Hα emission.

Similarly, we want to establish a $\mathrm{sSFR_{UV}}$ cut which is consistent with the UV emission being the normal emission of a star-forming galaxy. For this, we will return to our $\log(\mathrm{sSFR_{UV}}/\mathrm{yr}^{-1}) > -11.1$ cut established in the previous subsection. However, we further require that the galaxy has a NUV $- r$ colour consistent with being a star-forming galaxy. From an analysis of the colour magnitude diagram, and consistent with previous divisions (Salim et al., 2007; Arnouts et al., 2013), we require NUV $- r \leq 4.5$ to be star-forming.

We can now define RQ galaxies as those with $\log(\mathrm{sSFR_{UV}}/\mathrm{yr}^{-1}) > -11.1$, NUV $- r \leq 4.5$ and EW(H_α) < 3Å. In Figure 2.5, the fractions of RQ galaxies with respect to the total number of galaxies ($f_\mathrm{t} = N_\mathrm{t}/N$) for centrals and satellites are plotted for each stellar mass bin. The clearest difference between the two distributions is the excess of RQ fraction in satellites compared to centrals at low M_*, compared to the lack thereof at higher stellar masses. Over the entire low mass bin ($M_* < 10^{10.5}$ $\mathrm{M}_\odot$), there is an average 1 percentage point excess in RQ fraction of satellites compared to centrals at a 6.3σ significance.

Across all stellar mass bins, we count 2,758 RQ satellite galaxies and 12,080 RQ central galaxies. This gives 5.9 per cent and 6.7 per cent fractions of the total satellite/central galaxy count respectively. However, we find further evidence for a mass dependence by looking only at galaxies with $M_* < 10^{10}$ $\mathrm{M}_\odot$, where we find 303 RQ satellite galaxies and 340 RQ central galaxies, giving 2.7 per cent and 1.2 per cent of the total number of satellite/central galaxies with $M_* < 10^{10}$ $\mathrm{M}_\odot$ respectively, which is consistent given the timescale we are searching for and the typical age of a galaxy (100Myr/10Gyr $\sim$ 1per cent). As such, we see a slight increase in the

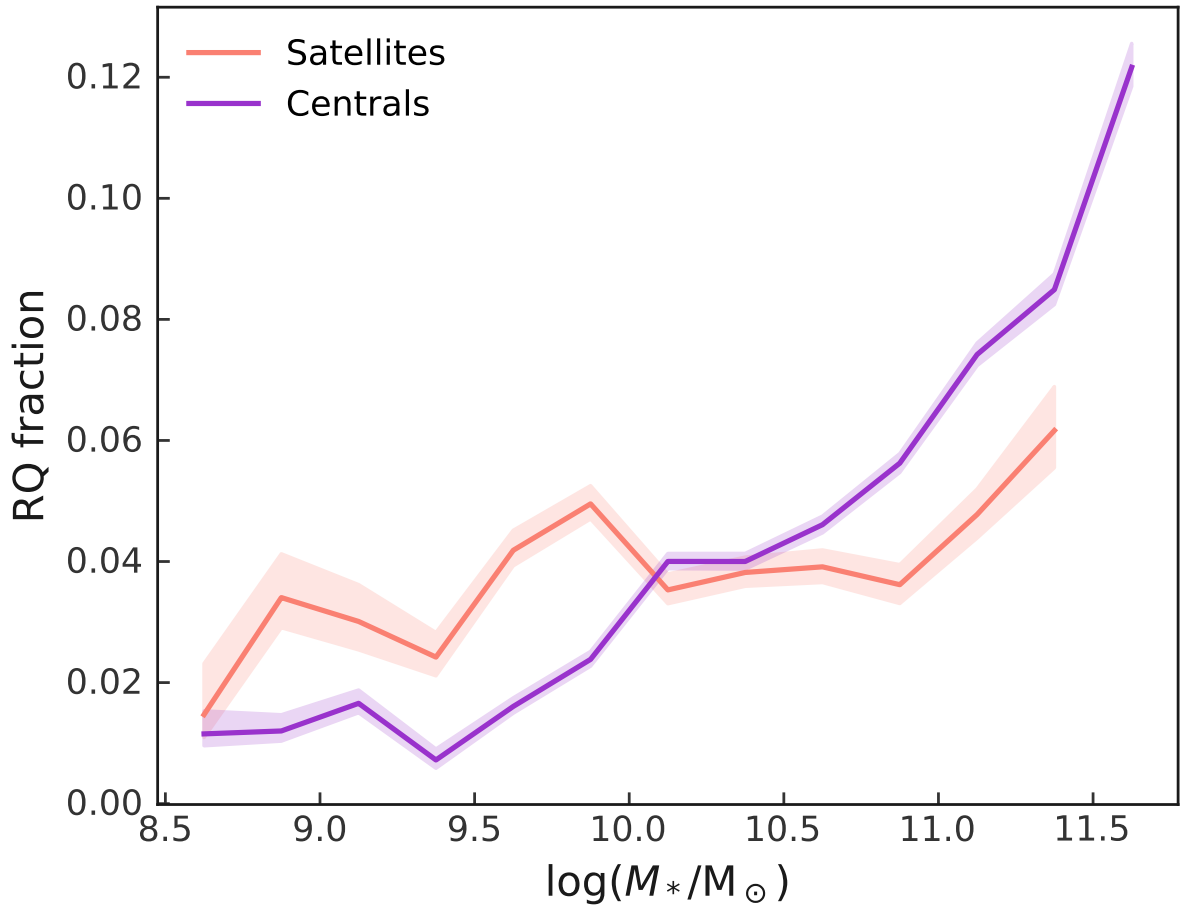


Figure 2.5: Fraction of RQ galaxies, $f_t = N_t/N$, where N_t is the number of RQ central(satellite) galaxies and N is the total number of central(satellite) galaxies. RQ galaxies are those with no detectable Hα and UV emission from star-formation.

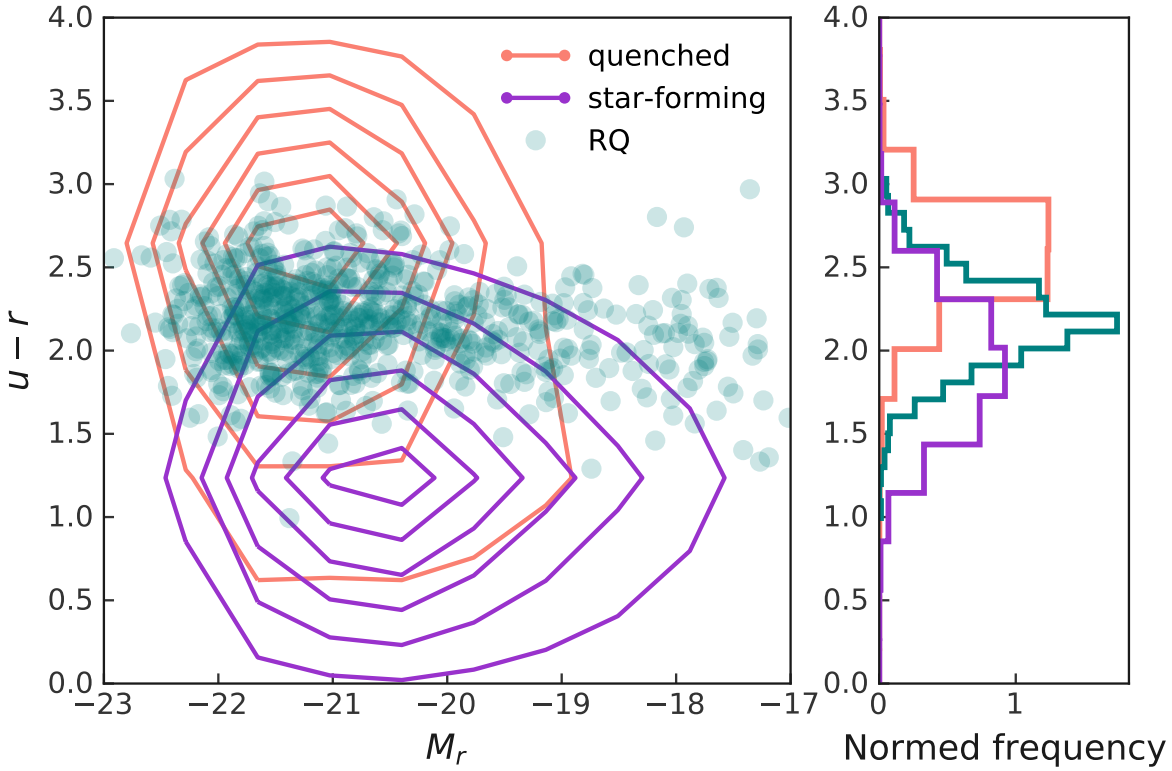


Figure 2.6: Colour magnitude diagram, $u - r$ against M_r. Contour plots indicate abundances of quenched and star-forming populations defined as above using $\mathrm{sSFR}_{\mathrm{H}\alpha}$. A marginalised distribution shows that RQ galaxies as defined in this paper lie between red and blue galaxies on a colour magnitude diagram.

fraction of RQ satellite galaxies at low-mass versus RQ central galaxies. This implies that although high-mass galaxies are more likely to be quenched, satellite RQ galaxies deviate from RQ centrals at low masses, meaning low-mass satellites may be more inclined to begin to quench based on environmental factors. In other words, while there is an excess of central RQ galaxies on the high-mass end, this is to be expected by mass-quenching mechanisms (Peng et al., 2010).

We plot a colour-magnitude diagram (CMD) in Figure 2.6. Contour lines indicate populations of quenched and star-forming galaxies, using definitions established in Section 2.3.1, using $\mathrm{sSFR}_{\mathrm{H}\alpha}$. Individual RQ galaxies are plotted over the contours. A histogram is plotted showing the

distributions of colours of the red and blue galaxies. The CMD and histogram confirm that RQ galaxies, as defined in this paper, lie between red and blue galaxies in terms of colour, and thus in terms of their evolution.

2.3.3 Group and satellite properties

Now that we have identified a population of galaxies with recently quenched star-formation and which are preferentially satellite galaxies, we can investigate the environments of those galaxies in more detail. The phase space distribution of galaxies in groups or clusters, that is, the plane of projected group-centric distance versus the relative velocity offset, has shown to hold important information on the path of a satellite upon entering the system (Muzzin et al., 2014; Jaffé et al., 2018). For each satellite, we calculate their relative velocity (Δv) with respect to the group velocity dispersion (σ) and the projected separation between the satellite and the central (r) with respect to the group halo radius (r_{180}). Figure 2.7 shows a 2d histogram with axes r/r_{180} and $\Delta v/\sigma$, which shows the distribution of the entire sample of satellite galaxies across the phase space with marginalised distributions on each axis for star-forming, quenched, and RQ satellite galaxies. Individual RQ galaxies are indicated on the plot by green circles. Note also that RQ galaxies populate the region of the CMD known as the 'green valley' (Salim, 2014). The distributions appear similar across the three distributions and in both the velocity distribution and radial distribution. There is a slight suggestion that the RQ population has a radial distribution more similar to the quenched population than the star-forming population, however KS-tests on all the distributions show no significant trends. However, this plot includes all satellites regardless of their stellar mass. We will investigate any possible stellar mass dependence further in Section 2.4.

We examine the excess of satellite RQs further by looking at the relative proportions of RQ satellites with respect to star-forming galaxies and quenched galaxies binned by group halo mass. In Figure 2.8, we plot the fraction of RQ galaxies compared to star-forming galaxies against the radial

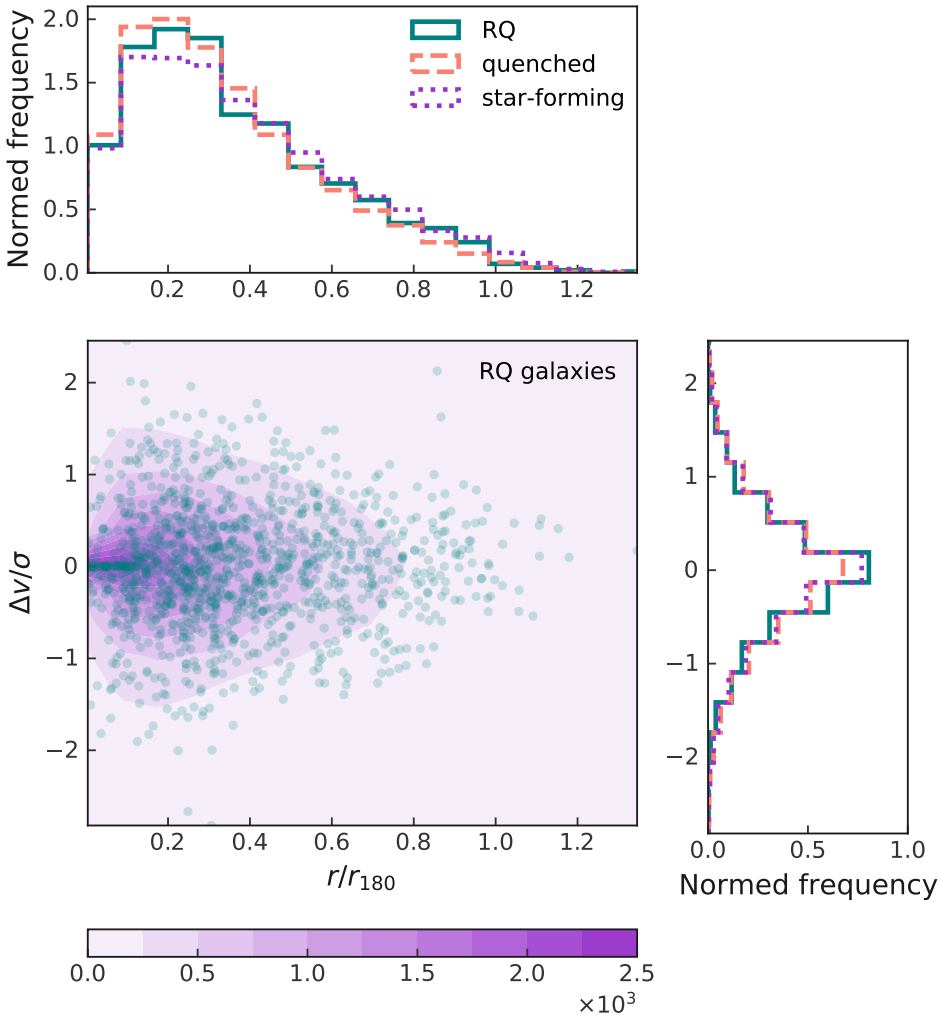


Figure 2.7: Phase space histogram showing r/r_{180} and $\Delta v/\sigma$ for all galaxies, with marginalised distributions on each axis for star-forming, quenched and RQ galaxies. Note the similarity in distributions between RQ, quenched, and star-forming galaxies. The z-axis denotes number of galaxies in each bin.

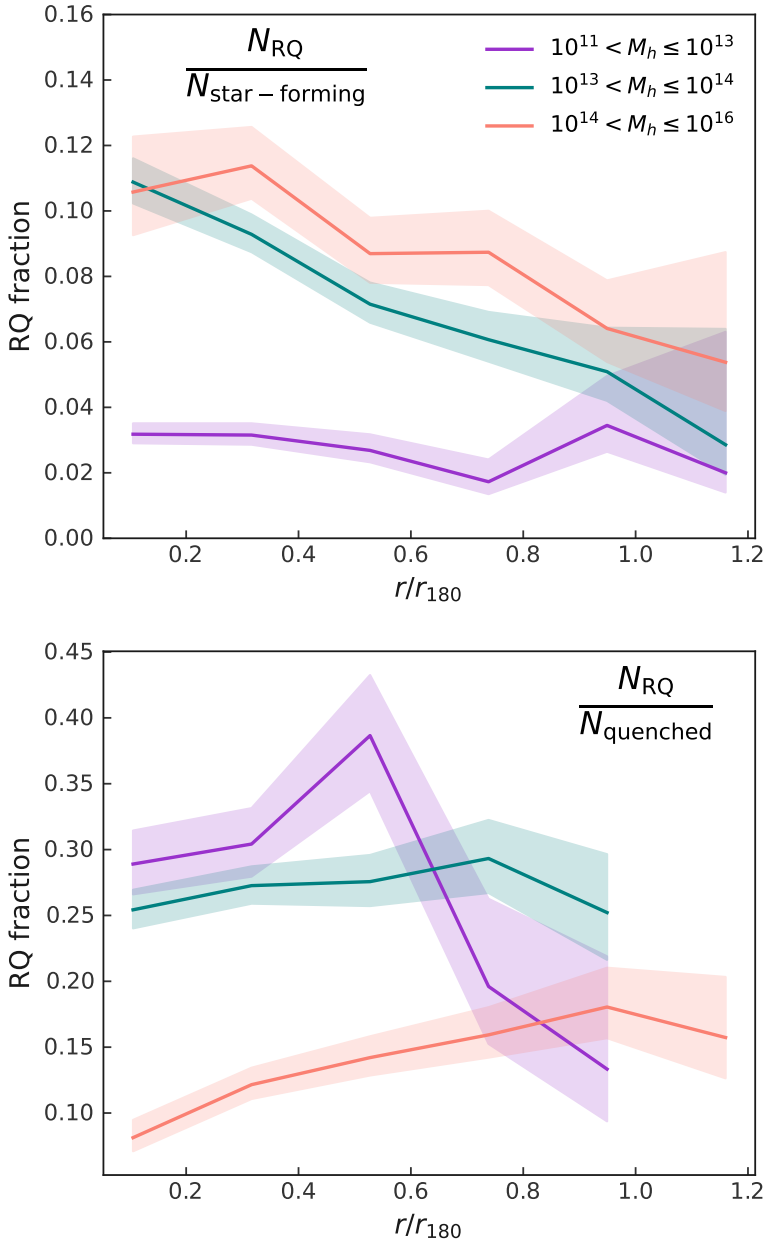


Figure 2.8: Fractions of RQ galaxies with respect to star-forming galaxies (top) and quenched galaxies (bottom) for different group halo mass bins. There is a clear downward trend for the fraction of RQ galaxies with respect to star-forming galaxies as r/r_{180} increases at high halo mass.

position of the satellite galaxy in the group (top panel). We also plot the fraction of RQ galaxy compared to quenched galaxies (bottom panel). First, examining the panel presenting the fraction of RQs with respect to the star-forming galaxies, we see two interesting trends. Firstly, there is a clear radial trend in that this ratio increases towards the center of the halo. This would be expected if satellites become RQs upon infalling into the group, and that their likelihood of quenching increases as they reach the center of the cluster. Secondly, there is a halo mass dependence to the RQ/star-forming ratio. Halo masses greater than 10^{13} $M_{\odot}$ host much higher rates of RQs than do halos less massive. Again, this may indicate that RQs occur in satellites after infalling, and that their rate of going through a RQ stage is related to the densities of gas or size of gravitational potentials they encounter.

In the bottom panel of Figure 2.8 the fraction of RQ to quenched galaxies is shown for the same bins of halo mass and group-centric radius. For massive halos $\left(> 10^{13}\ M_{\odot}\right)$, there is a clear opposite radial trend, in that this ratio is smaller with decreasing radius. Since the quenched galaxies are a larger proportion of all galaxies towards the group centre, this means that the RQ population is anti-correlated with the quenched population. Usefully, this means that RQs are not likely to be a momentary, recurrent phase in the life of quenched galaxies, but rather indicate a once-off event. Interestingly, the halo mass dependence of this ratio is less clear than it was in the RQ/star-forming ratio and may suggest that the past level of quenching is not as closely correlated with current quenching. If quenching in a group occurs on short timescales with respect to the formation of the group, then this relative lack of correlation would be expected.

2.3.4 Rejuvenating galaxies

The anti-correlation between the RQ population and the quenched population suggests that the RQs we are seeing are not a stage in the life of a normal quenched galaxies, but rather a phase indicative of a key quenching event. However, it is worth noting that galaxy-group and galaxy-

galaxy interactions or continued further gas accretion may cause star-formation to begin again in a quenched galaxy, so called 'rejuvenation'. Indeed, models of galaxy formation in which the gas accretion (and subsequent star formation) is closely tied to the dark matter accretion suggest that galaxies should naturally go through periods of quenching and rejuvenation. For instance, a model which ties gas accretion to dark matter accretion finds that between 20 per cent and 80 per cent of galaxies at $z = 0$ (depending on their stellar mass) go through a rejuvenation phase of at least 300 Myr of quiescence, followed by 300 Myr of star formation (Behroozi et al., 2019). This motivates a short-timescale search for galaxies that are just beginning their rejuvenation.

For this reason, in this paper, rejuvenating galaxies are defined as those with significant Hα detection [EW(Hα) $\geq$ 3Å] but negligible UV emission, i.e. $\mathrm{sSFR_{UV}} < 10^{-11.1}$ yr^{-1}. We require small amounts of UV because, when star-formation commences again, it will take time for the UV emission to build up to significant (in terms of defining star-formation/quenched status) amounts. Using similar logic in defining RQ galaxies, this implies that star-formation has recently begun again in these galaxies. Due to requiring sensitivity to low-levels of star-formation from the UV emission, we limit our analysis in this section to galaxies at $z < 0.1$. Note that this is a shorter-timescale rejuvenation selection than previous studies (see, e.g., Thomas et al., 2010; Chauke et al., 2019, for low- and high-redshift analyses respectively) which used spectral features to determine if galaxies had ever gone through a rejuvenation phase. The spectral features are only sensitive to longer timescales (>100 Myr) than ours. Our selection is designed to find those galaxies just in the process of rejuvenating, and are not the integral constraint on the fraction that previous studies are.

We stress, that while our selection of galaxies may include the sought after short-timescale rejuvenating galaxies, it is not exclusive. It will contain contaminants and an independent verification of the true nature of these potentially rejuvenating galaxies is difficult to obtain since most photometric and spectroscopic indicators vary on longer timescales than is relevant. In particular, since UV flux is more affected by dust than Hα, our selection may be contaminated by dust galaxies. This means our selection represents an upper limit on rejuvenating galaxies defined in this way.

Nevertheless, we will remove galaxies from the sample which are not obviously of rejuvenating origin, but it should be cautioned that what is left is not necessarily rejuvenating.

The largest source of contamination will be AGN. Although optical line AGN are relatively rare in galaxies without significant NUV emission (Kauffmann et al., 2007), we will need to take this into account. In Figure 2.9, we show the BPT diagram for the whole sample of galaxies (black dots and grey contours) and for those passing our rejuvenation selection (green dots). We also show the demarcation line of Kauffmann et al. (2003b) which divides purely star-forming galaxies (below the dashed line) from composite or AGN-dominated galaxies (above the line). By this stringent definition, only 1/3 of our rejuvenation candidate galaxies have emission lines caused by pure star formation.

Removing the AGN-dominated galaxies from the sample does not necessarily leave only rejuvenating galaxies, but it is now worth examining the stellar mass and environmental characteristics of these candidates. In Figure 2.10, we show the ratio of the number of rejuvenating galaxy candidates over the total number of galaxies as a function of two stellar mass bins, low stellar mass ($10^{10} \leq M_*/\mathrm{M}_\odot < 10^{11}$) and high stellar mass ($10^{11} \leq M_*/\mathrm{M}_\odot < 10^{12}$) for each of the central and satellite populations. Note the minimum stellar mass of the rejuvenating galaxy candidates does not go below 10^{10} $\mathrm{M}_\odot$. The fraction of rejuvenating galaxy candidates in the low stellar mass bin is about 0.2-0.4 per cent, while it is about 0.4-0.5 per cent in the higher stellar mass bins. This mild stellar mass dependence is at least partially due to the underlying stellar mass dependence of the quenched fractions, as it is not possible to have a rejuvenated galaxy without first quenching it. Interestingly, there is only a mild difference in the fraction of rejuvenated galaxy candidates when divided into central and satellite galaxies. Quantitatively, the slight excesses of rejuvenating candidate centrals seen in the left and right panels of Figure 2.10 have significances of 3.6 σ and 0.6 σ respectively. Thus, the data does not strongly indicate a significant excess of rejuvenating candidate centrals compared to satellites. In terms of bulk numbers, We find 257/59,784 rejuvenating candidates in low stellar mass central galaxies, and 39/7,795 rejuvenating candidates in high stellar mass

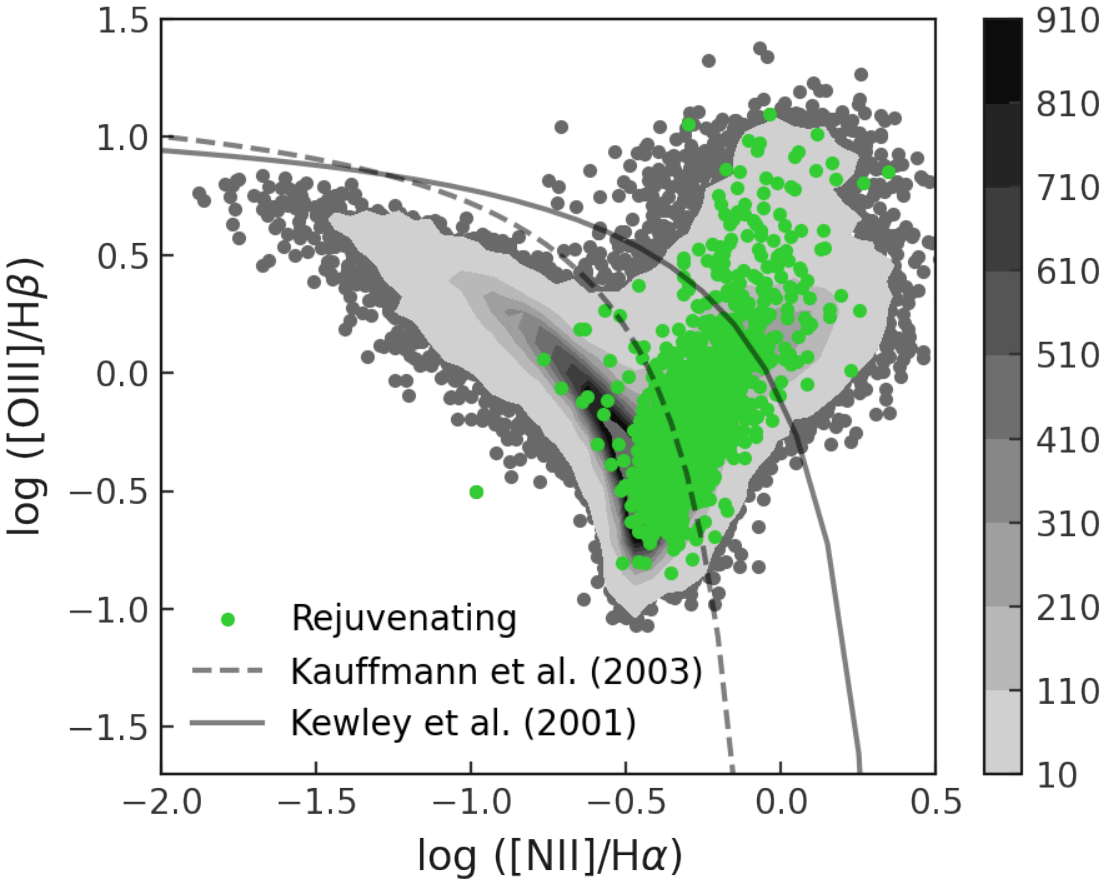


Figure 2.9: BPT diagram with the Kauffmann et al. (2003b) demarcation line. Two-thirds of the galaxies identified by our rejuvenating candidate selection are shown here to not have truly star-forming emission.

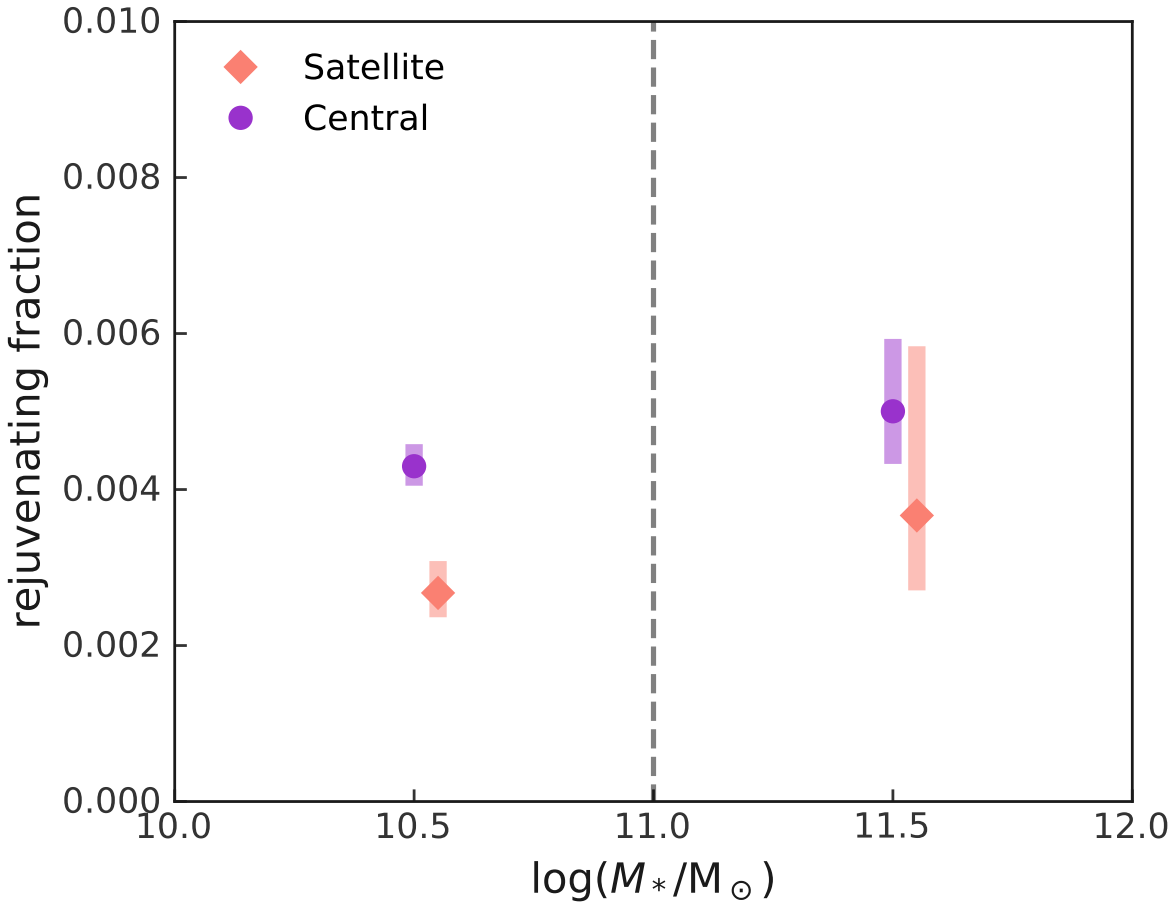


Figure 2.10: Fraction of candidate rejuvenating galaxies after removal of AGN-dominated galaxies, $f_{\rm r} = N_{\rm r}/N$, where $N_{\rm r}$ is the number of candidate rejuvenating central(satellite) galaxies and N is the total number of central(satellite) galaxies. The data is binned by stellar-mass, with low stellar-mass on the left and high stellar-mass on the right.

central galaxies. This compares to 55/20,565 rejuvenating candidates low stellar mass satellite galaxies and 6/1,636 rejuvenating high stellar mass satellite galaxies. The behaviour in this plot is in contrast to the peak in RQ satellite galaxies compared to central galaxies at $M_* \sim 10^{9.5}$ $M_\odot$ in Figure 2.5. While we see clear evidence that the RQs are environmentally effected, the rejuvenated candidate galaxies are not. This gives confidence that our RQ population is a true population of galaxies undergoing a catastrophic quenching event.

For galaxies with stellar mass $M_* > 10^{10}$ $M_\odot$, the fraction of rejuvenating candidate galaxies which have their emission due purely to star formation is 0.5 per cent. If these galaxies are all truly rejuvenating and the timescale with which we would detect them is $\sim$ 50 Myr, then we would expect 10 per cent of galaxies to go through this phase every Gyr. This number is not incompatible with the results from galaxy formation models, or the other methods of measuring longer timescale rejuvenation. It is a matter for future work to make a holistic confrontation of short- and long-timescale rejuvenation with galaxy formation models.

2.4 Discussion

These results show that there are multiple aspects at play which influence the star-formation of galaxies and which depend on various galactic properties. We see enhanced quenching in satellites, likely due to the environmental effects that act on a satellite galaxy as it moves through a group. To get a clearer picture of how the environment effects a satellite galaxy, we can isolate galaxies that are in the process of quenching, and relate the individual galactic properties with those of the group. We note that there is a higher fraction of RQ satellite galaxies at $M_* < 10^{10}$ $M_\odot$ compared to RQ central galaxies. This suggests that low-mass satellite galaxies are quenched more efficiently than low-mass centrals are. This scenario of low-mass satellite quenching is consistent with previous studies using direct stellar ages (Haines et al., 2006; Smith et al., 2009). It also shows similar trends

to studies of spectroscopically selected post-starburst galaxies (Paccagnella et al., 2017), although with a different selection method from ours.

It was found in Section 2.3.3 that RQ galaxies evenly occupy the full range of r/r_{180}, and that there was not a significant difference in the distributions of RQs, star-forming and quenched galaxies. This is, perhaps, inconsistent with Muzzin et al. (2014) who find a particular ring structure in the phase-space location of $z \sim 1$ post-starburst cluster galaxies. Similarly, Owers et al. (2019) found that Hδ strong galaxies are principally found at small (< 0.5 R_{200}) cluster-centric distances. However, it is clear that the exact definition of a 'quenching' galaxy, and the stellar mass limits will make a difference (Paccagnella et al., 2017). Our result was shown for the full range of stellar masses, and we have seen that the most prominent differences may occur at low stellar mass. For this reason, we separate low-mass and high-mass satellites. In Figure 2.11, we show the radial distribution of low-mass and high-mass satellites of both the RQ and star-forming variety. The top panel shows low-mass ($10^8 < M_*/\,\mathrm{M}_\odot \leq 10^{10}$) galaxies, and the bottom panel shows high-mass ($10^{10} < M_*/\,\mathrm{M}_\odot \leq 10^{13}$). The mean distribution of each plot is also shown for ease of comparison.

If quenching were driven primarily by environmental factors, we would see a radial difference in the star-forming and RQ populations. However, for the high-mass bin of Figure 2.11, we find that the RQ and star-forming radial distributions are nearly identical, suggesting that the quenching mechanisms for these galaxies is unlikely to be primarily group-driven. It is a different story for the low-mass galaxies. For these, the RQs are more concentrated towards the center compared to star-forming galaxies, and are consistent with having been in the massive halo for a long time, while the star-forming galaxies have a radial profile more consistent with recent infall (Oman et al., 2013; Jaffé et al., 2018). This supports the idea that low-mass galaxies are more susceptible to the environmental effects, while the quenching of high-mass galaxies is driven by internal effects.

We can support the role of environmental effects further by recalling the clear halo mass

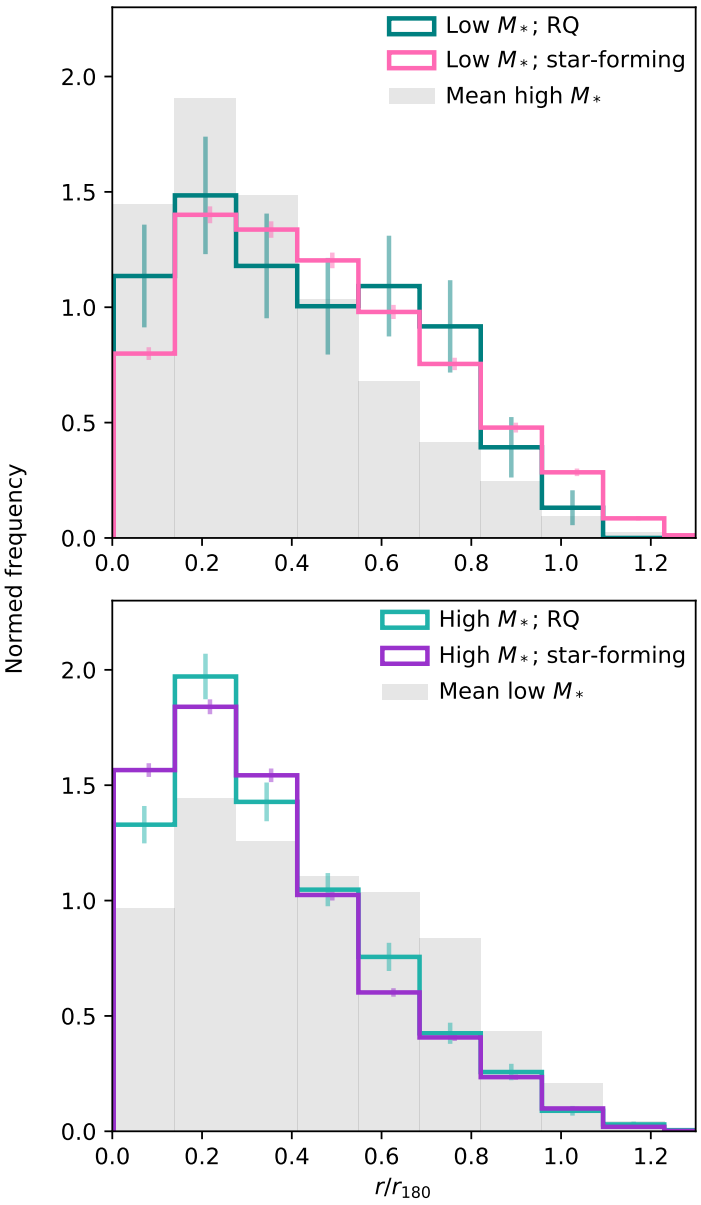


Figure 2.11: Histograms of stellar mass binned RQ and star-forming galaxies with respect to r/r_{180}. Here, low stellar mass (top panel) refers to galaxies with stellar mass $10^6 < M_* \leq 10^{10}$ $M_\odot$ and high stellar mass (bottom panel) refers to galaxies with stellar mass $10^{10} < M_* \leq 10^{13}$ $M_\odot$. The mean distribution of each plot is shown for ease of comparison. Errors are computed using the normalised count in each bin.

dependence in the ratio of RQs to star-forming galaxies seen in Figure 2.8. With increasing halo mass, the proportion of RQ galaxies with respect to star-forming galaxies, across all stellar masses, increases. The opposite is true for RQ fractions with respect to quenched galaxies. The halo mass dependence for the fraction of RQs with respect to star-forming galaxies is further clear evidence that some of the RQs are driven by environmental processes. This halo mass dependence is consistent with the work of Paccagnella et al. (2019) who also showed a strong dependence of the post-starburst fraction with halo mass. This consistent result, with a very different galaxy selection, clearly points to some role for halo mass in the appearance of this quenching.

However, it is important to note, that while there is a strong halo mass dependence for the appearance of RQs, even the lowest halo masses show an increasing fraction of RQs with respect to star-forming as a function of decreasing radius (e.g., the purple line in the top panel of Figure 2.8). This strongly suggests that, while the effectiveness of environment-induced quenching is lower in low-mass halos, it is still a factor. This is an intriguing result, which is also consistent with other previous studies (Zabludoff et al., 1996; Paccagnella et al., 2019; Vulcani et al., 2020). The environmental effect clearly can not be dependent only on halo mass, but perhaps instead some other physical feature which correlates with halo mass, such as relative velocity and intragroup gas density.

We present further evidence for this suggestion in Figure 2.12, which shows the distribution of satellite-central velocity offset with respect to the group velocity dispersion split by low halo mass ($10^{11} < M_h \leq 10^{13.5}$ $M_\odot$; top panel) and high halo mass ($10^{13.5} < M_h \leq 10^{16}$ $M_\odot$; bottom panel). The mean distribution of each plot is also shown for ease of comparison. We find that, for both the low and high halo mass subsets, the RQs appear to have lower velocity offsets than do star-forming galaxies in the same mass halos. A lower velocity offset is expected if these galaxies have been in the group for longer than the typical star-forming galaxy. This is evidence that there is a timescale on the order of the group-crossing time before the galaxy becomes a RQ galaxy. That said, we see a similar pattern as in Figure 2.11, where in each mass bin, the RQ and star-forming populations

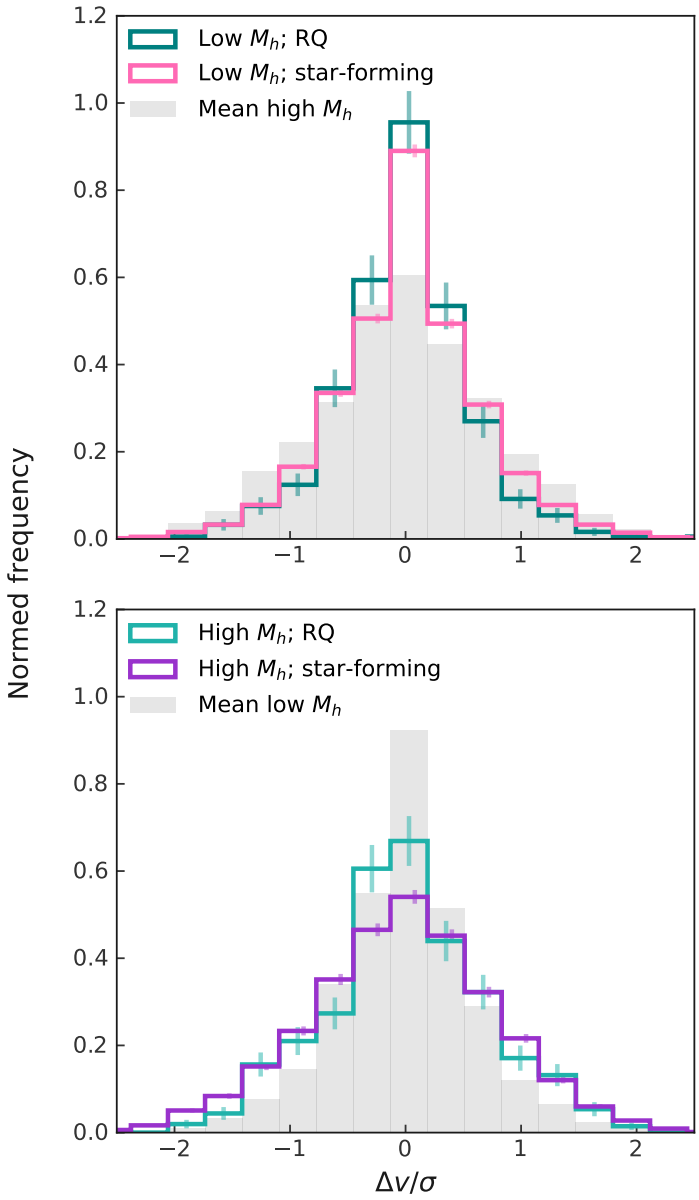


Figure 2.12: Histograms of halo mass binned RQ and star-forming galaxies with respect to $\Delta v/\sigma$. Here, low halo mass (top panel) refers to groups with halo mass $10^{11} < M_h \leq 10^{13.5}$ $M_\odot$ and high halo mass (bottom panel) refers to groups with halo mass $10^{13.5} < M_h \leq 10^{16}$ $M_\odot$. The mean distribution of each plot is shown for ease of comparison. Errors are computed using the normalised count in each bin.

have practically identical distributions. This further implies that, while the environmental effects cannot be neglected, they are not the primary driver of quenching mechanisms.

Overall, these results describe a picture of the state of star-formation in various classes of galaxies and the confluence of factors which drive them. We see that galaxies which have recently truncated their star-formation have a strong stellar mass dependence, which occurs in both central and satellite galaxies. However, at low stellar mass ($M_* \lesssim 10^{10}$ M$_\odot$), these recently-quenched galaxies are much more likely to be satellite galaxies. Further, the occurrence of these RQs shows a strong halo mass and radial dependence, with more star-forming galaxies being transformed into RQs in high mass halos and nearer the group center. We also find that the rejuvenated galaxy candidates do not have an environmental dependence, so will not preferentially revive these RQ satellites. Finally, although we find a clear environmental effect responsible for some RQs, we still find a sizeable population (especially at high stellar mass) which occur in both central and satellite galaxies in equal occurrences.

2.5 Conclusions

By combining Hα and UV measurements, from SDSS and GALEX respectively, we gain a unique insight into the instantaneous star-formation rate of satellite galaxies in galaxy groups. Using properties of the group of each satellite, from the YGC, we examine the environment of the satellite and investigate its significance on quenching. Our main results can be summarised as follows:

- We find a population of recently-quenched galaxies ('RQs') which lack Hα emission but maintain UV emission indicative of star-formation. This is characteristic of a galaxy which has had its star-formation quenched in the last $\sim$ 100 Myrs. The occurrence of these RQs is a strong function of stellar mass, and occur in central and satellites at the same rate in high stellar mass galaxies ($M_* > 10^{10}$ M$_\odot$). However, at low stellar masses, these RQs are more

likely to occur in satellite galaxies than in central galaxies.

- The occurrence of RQ galaxies in the satellite population is a strong function of the total host halo mass and projected group-centric distance. Measured by the ratio of RQ galaxies to star-forming galaxies, RQs are more likely to occur in high mass halos and closer to the group centre. Both of these features are characteristic of environmentally driven processes.

- We examined the population of rejuvenating galaxy candidates which show Hα emission but lack UV mission, suggesting that they could have recently begun their star-formation again after a period of quiescence lasting at least 100 Myrs. This population showed no environmental dependence, which suggests that our 'RQ' satellite galaxies are not simply a normal part of a on-off star-formation cycle in galaxies.

The evidence for an environmental role in the production of RQs that we see in low-mass galaxies, as well as the halo mass and radial dependence, is clear. This suggests that some environmental process is acting over short timescales to quench at least some of these galaxies. Given the signatures in the radial and velocity distributions of these galaxies, this process is likely to occur some time after a galaxy enters the halo. Given the short timescale of the RQ phase, and the long timescale after the entering of the halo, our results agree with the 'delayed-then-rapid' quenching scenario of Wetzel et al. (2012).

However, the clear environmental role should not be overstated. The strong stellar mass dependence of the RQ galaxies is similar in both satellites and centrals, and indeed the highest occurrence rates of RQs occur in high stellar mass galaxies and equally in central and satellites. This suggests that there is a significant additional factor driving the quenching of galaxies besides environment. This, along with a further elucidation of the role of environment, AGN and morphology, will be the subject of future work.

Appendix

2.A Dust Attenuation

As stated in Section 2.3.1, we do not apply dust attenuation corrections to the star-formation rates. This allows us to use the full range of galaxies with well-measured Hα fluxes, while maintaining the connection directly to the massive stars that produce this emission. Given the dust is expected to principally come from local scales, it may be that such effects are similar in centrals and satellites for similar star-formation rates. However, we must test this assumption, and show its consistency in all the regions we probe. We estimate the effect these dust corrections would have on our SFRs by using the Balmer decrement, as in Gilbank et al. (2010) (see references therein):

$$A_{\mathrm{H}\alpha} = \frac{2.5}{k_{\mathrm{H}\beta}/k_{\mathrm{H}\alpha} - 1} \log\left(\frac{1}{2.85}\frac{f_{\mathrm{H}\alpha}}{f_{\mathrm{H}\beta}}\right), \tag{2.6}$$

where $k_{\mathrm{H}\beta}/k_{\mathrm{H}\alpha} = 1.48$ and $f_{\mathrm{H}\alpha(\beta)}$ is the H$\alpha(\beta)$ flux. Using the fluxes of Hβ and Hα for galaxies with both well measured we find that the average attenuation is $A_{\mathrm{H}\alpha} \sim 1$, and this shows no difference between satellites and central galaxies. Since applying this attenuation correction would have no appreciable difference on the differential effects of centrals and satellites and thus no effect on our subsequent analysis, we do not apply it. However, we fully investigate the relative effect of dust attenuation here. We use the ratio of Hα to Hβ as a proxy for the attenuation coefficient. We ensure that each galaxy that is considered to have well-measured Hα or Hβ has a SNR > 3 for both measurements.

Figure 2.13 illustrates the flux ratio for centrals and satellites in three stellar mass bins, $M_*/\mathrm{M}_\odot < 10^{10}$, $10^{10} \leq M_*/\mathrm{M}_\odot < 10^{11}$ and $M_*/\mathrm{M}_\odot \geq 10^{11}$. Each bin contains 11,006 centrals and 4,031 satellites, 49,119 centrals and 13,300 satellites, and 63,854 centrals and 11,474 satellites respectively. The mean flux ratio in each bin is 3.32 ± 0.03 (centrals) and 3.40 ± 0.05 (satellites), 4.04 ± 0.04 (centrals) and 4.08 ± 0.05 (satellites), and 4.38 ± 0.31 (centrals) and 4.27 ± 0.15 (satellites) respectively. Apart from negligible differences, the distributions of the flux ratio are identical. This implies that the dust attenuation is the same for centrals and satellites with respect to stellar mass, at least for the case when both Hα and Hβ are well measured.

To check whether there could be differences in dust attenuations, we will look at subgroups of satellites in different host halo masses, different radial positions and different velocity offsets. First, in Figure 2.15, we plot the flux ratio with respect to three group halomass bins. These bins have total galaxy numbers of 9,712, 5,483, and 11,266 respectively and the mean flux ratio in each bin is 4.08 ± 0.07, 4.19 ± 0.09, and 4.06 ± 0.15 respectively. These differences are minimal.

Next, we plot the flux ratio of satellite galaxies in different bins of absolute normalised velocity offset, $|\Delta v/\sigma|$. This is shown in Figure 2.14. The number of galaxies in each bin is 14,643, 7,665, and 4,153, with mean flux ratio 4.13 ± 0.06, 4.08 ± 0.18, and 4.01 ± 0.09 respectively. Again, we see negligible difference in flux ratio.

Finally, Figure 2.16 plots the flux ratio of satellite galaxies in bins of group-centric radius, r/r_{180}. The number of galaxies in each bin are 15,811, 5,690, and 4,960, with mean flux ratio 4.12 ± 0.13, 4.11 ± 0.09, and 3.99 ± 0.07 respectively. There is a slightly larger flux ratio (i.e. dust attenuation coefficient) for galaxies closer to the group centre, and a slightly lower flux ratio for galaxies towards the group edge. However, these slight offsets are considered negligible.

It is possible that galaxies that are deemed passive by sSFR have preferentially higher dust attenuation coefficients, meaning their sSFR is underestimated. However, in Figure 2.17 we see this is not the case. This figure plots the flux ratios of star-forming and quenched galaxies as these

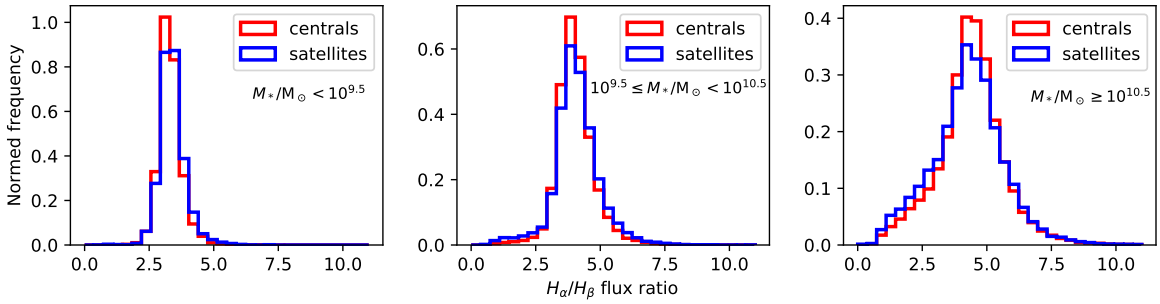


Figure 2.13: Distributions of flux ratios Hα/Hβ in three stellar mass (M_*) bins as labeled in each panel. We see the flux ratio distribution is the same for central galaxies and satellite galaxies with respect to stellar mass.

were defined in Section 2.3.1. We see that, for quenched galaxies (i.e. low sSFR), there is a wide range of flux ratio available. In fact, the mean flux ratio for quenched galaxies is lower than that of star-forming galaxies, with 3.90 ± 0.09 and 4.16 ± 0.11 respectively. These results confirm that our results are not biased by dust attenuation.

In this Appendix, we have shown that there appears to be no evidence for differential dust effects which could be affecting the bulk of our results. However, we caution that we can not rule out effects when Hβ can not be accurately measured, or for individual galaxies.

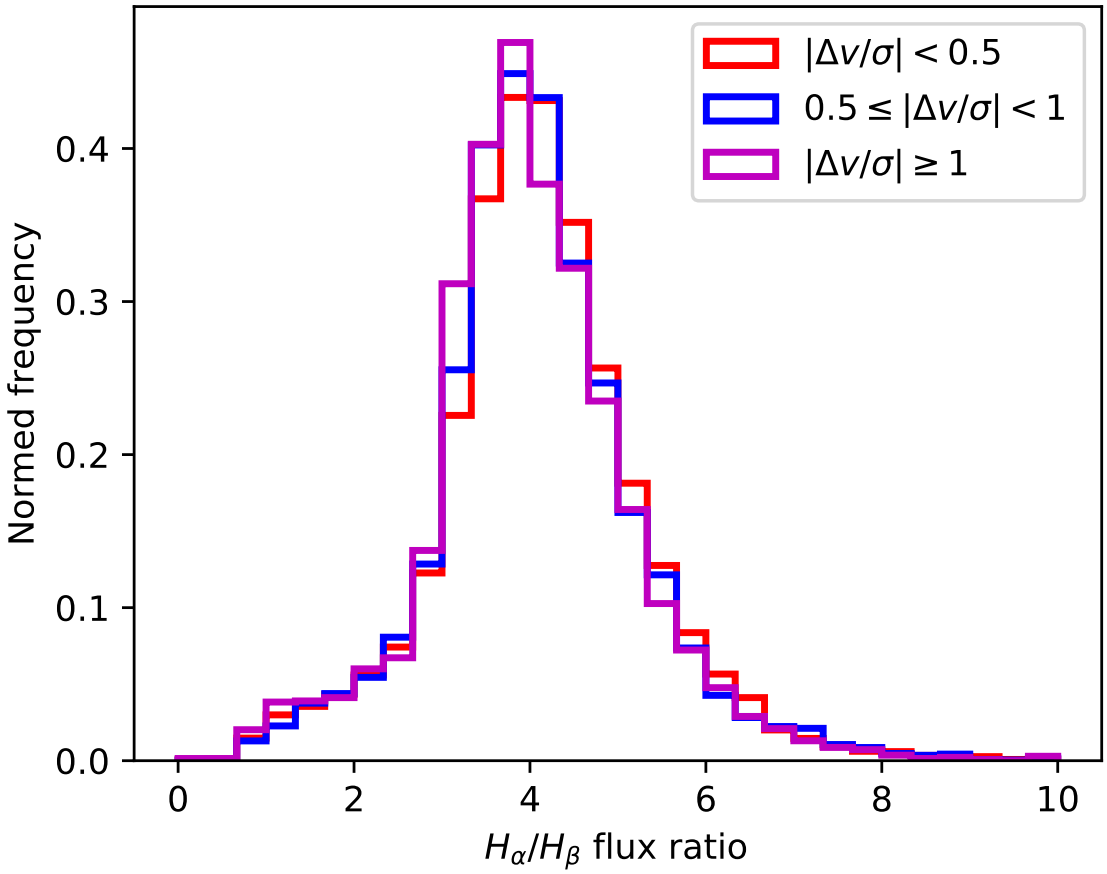


Figure 2.14: Distributions of flux ratios Hα/Hβ in three absolute normalised velocity offset ($|\Delta v/\sigma|$) bins. We see the flux ratio distribution is the same regardless of velocity offset.

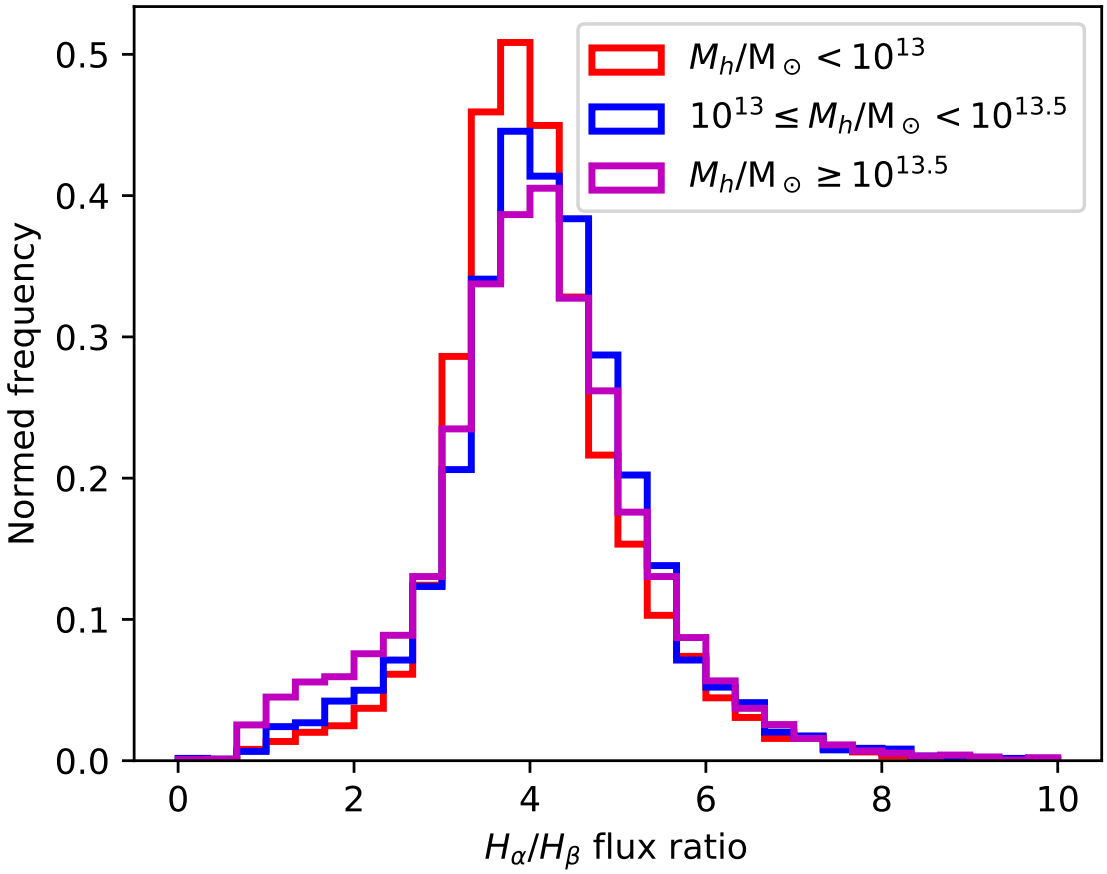


Figure 2.15: Distributions of flux ratios Hα/Hβ in three halomass (M_h) bins. We see the flux ratio distribution is the same regardless of halomass.

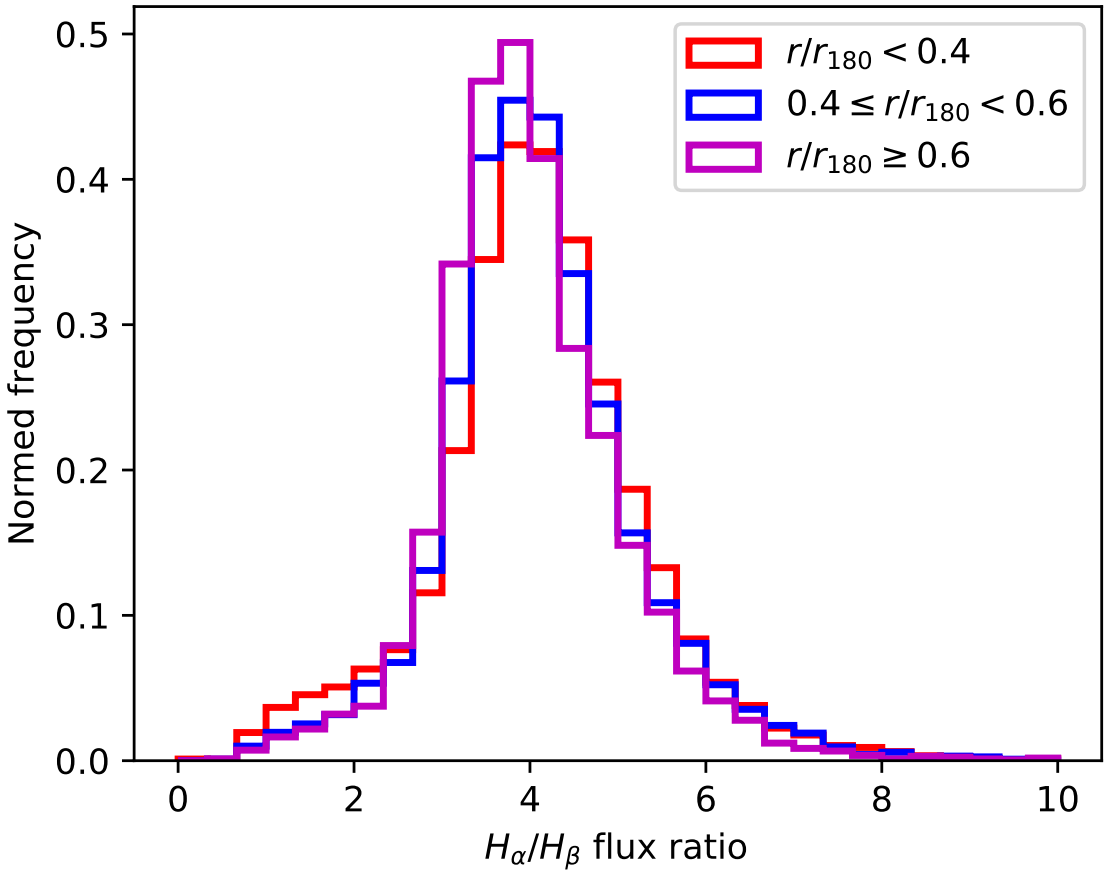


Figure 2.16: Distributions of flux ratios Hα/Hβ in three group-centric radius (r/r_{180}) bins. We see the flux ratio distribution is the same regardless of group-centric radius.

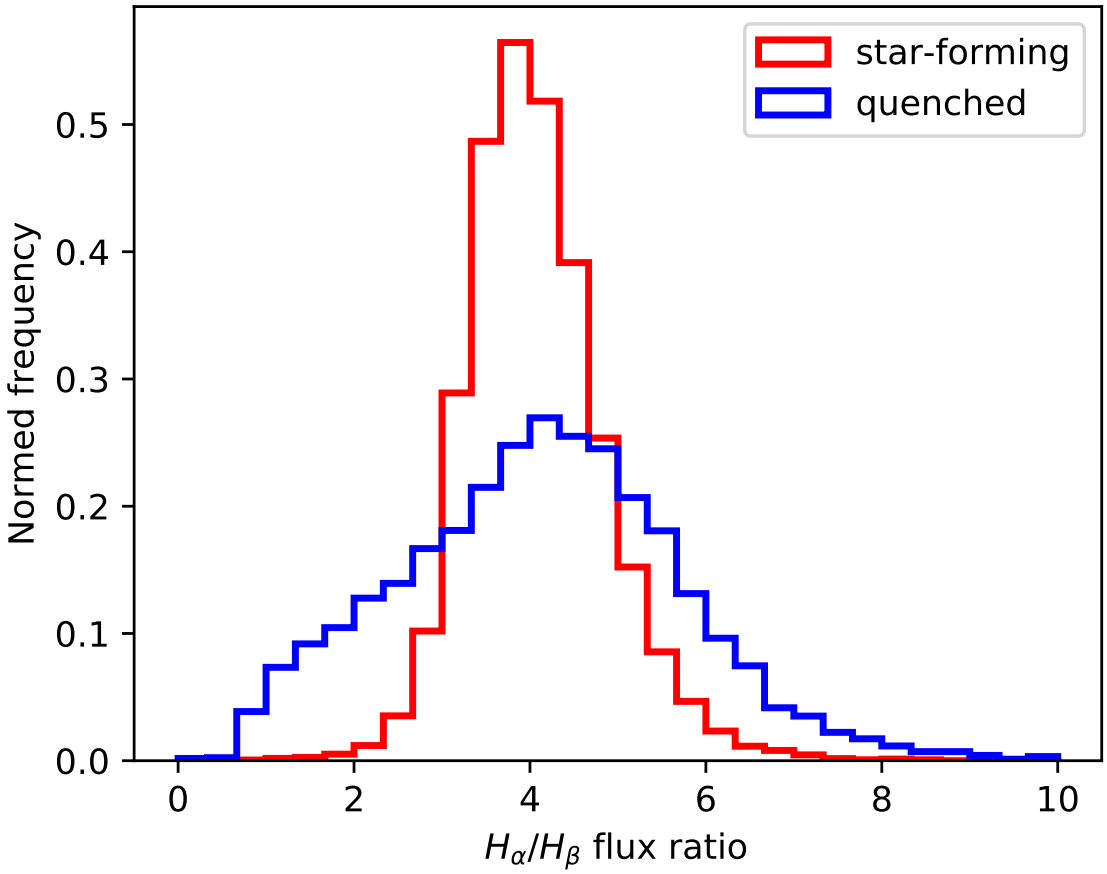


Figure 2.17: Distributions of flux ratios Hα/Hβ for star-forming ($\log(\mathrm{sSFR_{UV}}[\mathrm{yr}^{-1}]) > -11.1$) and quenched ($\log(\mathrm{sSFR_{UV}}[\mathrm{yr}^{-1}]) \leq -11.1$) galaxies. We see the quenched population is not unduly biased by high flux ratios (i.e. dust attenuation coefficients).

Chapter Three

AGN variability

This Chapter contains the paper "Photometric variability in star-forming galaxies as evidence for low-mass AGN and a precursor to quenching" (Cleland and McGee, 2022), published in MNRAS.

We measure the optical variability in $\sim$ 16500 low-redshift ($z \sim 0.1$) galaxies to map the relations between AGN activity and galaxy stellar mass, specific star-formation rate, half-light radius and bulge-to-total ratio. To do this, we use a reduced χ^2 variability measure on > 10 epoch lightcurves from the Zwicky Transient Facility and combine with spectroscopic data and derived galaxy parameters from the Sloan Digital Sky Survey. We find that below stellar mass of 10^{11} $M_\odot$, galaxies classed as star-forming via the BPT diagram have higher mean variablities than AGN or composite galaxies. Revealingly, the highest mean variabilities occur in star-forming galaxies in a narrow range of specific star-formation $10^{-11} <$ sSFR/yr$^{-1} < 10^{-10}$. In very actively star-forming galaxies $\left(\text{sSFR/yr}^{-1} > 10^{-10}\right)$, the reduced variability implies a lack of instantaneous correlation with star-formation rate. Our results may indicate that a high level of variability, and thus black hole growth, acts as a precursor for reduced star-formation, bulge growth, and revealed AGN-like emission lines. These results add to the mounting evidence that optical variability can act as a viable tracer for low-mass AGNs and that such AGNs can strongly affect their host galaxy.

3.1 Introduction

In the past two decades, the study of active galactic nuclei (AGN) and their properties has become widespread, in part thanks to recent advances in both multi-wavelength astronomy and long-term time-domain surveys. One of the celebrated facets of AGN behaviour is that the central black hole is well correlated with the growth of the bulge, and thus, the growth of the galaxy stellar mass (Magorrian et al., 1998; McConnell and Ma, 2013; Kormendy and Ho, 2013; Reines and Volonteri, 2015). This tight correlation implies a self-regulation which links galaxy evolution to black hole growth that has been shown to be important in theoretical models of galaxy formation (Di Matteo et al., 2005; Croton et al., 2006; Bower et al., 2006). This raises the question - can we see observational evidence that AGN activity and the resulting black hole growth has a direct effect on galaxy properties such as its star-formation rate or morphology?

Theoretically, it is understood that AGN feedback has an effect on the star-formation rate of a galaxy, by either heating up cold gas and thus preventing it from condensing to form stars, or by energetically expelling gas from star-forming regions (see Fabian, 2012, for a review). However, these processes are still not fully understood and this mode of quenching is heavily confounded with other processes such as environmental quenching (e.g. Wetzel et al., 2013; Cleland and McGee, 2021) and/or mass quenching (Peng et al., 2010; Peng et al., 2015). Therefore, it is useful to investigate AGN activity in galaxies across the full stellar mass range in a wide variety of environments and stages of evolution.

Unfortunately, it is difficult to find a single observational measure which gives a uniform accounting of the presence of an AGN. Generally, commonly used indicators cannot be uniformly applied to all galaxies with equal effectiveness. For instance, the often-used practise of measuring emission line ratios to distinguish AGN emission from star-formation is often not effective in strongly star-forming galaxies because the star-formation swamps the AGN emission (Baldwin et al., 1981; Cann et al., 2019; Agostino et al., 2021). One promising route to a uniform indicator

is through examining the photometric variability. Variability in the luminosity of galaxies can act as an indicator for varying activity levels in the AGN. Higher levels of activity over the observing period may suggest stronger black hole growth and thus stronger evolutionary links. In the short term, i.e. over timescales of days to years, variability has been detected in lightcurves of AGN in a variety of wavelengths (Cartier et al., 2015; Caplar et al., 2017; Smith et al., 2018a). Variability over longer timescales has been uncovered through the use of models and simulations (Novak et al., 2011; Bland-Hawthorn et al., 2013; Sartori et al., 2018). Optical variability has also been shown to be a reliable method of uncovering low-mass AGN otherwise obscured by star-formation (Baldassare et al., 2018, 2020; Ward et al., 2022; Burke et al., 2022).

In this paper we attempt to extend the application of optical variability across a full sample of galaxies at low redshift drawn from the Sloan Digital Sky Survey. To quantify the optical variability, we use the reduced χ^2 of the magnitudes of galaxy lightcurves drawn from the Zwicky Transit Facility. This is found to be a robust method, both from our own formalism, and from the work of Zibecchi et al. (2020). This method is agnostic of galaxy type and can be applied to the entire sample, including galaxies that are deemed non-AGN by other methods such as a BPT diagram (Baldwin et al., 1981). In Section 3.2 we describe the dataset, in Section 3.3 we explain how variability is calculated and discuss some initial results, in Section 3.4 we interpret and discuss the results, and in Section 3.5 we summarize. Throughout we adopt the cosmology used in Omand et al. (2014), from where we derive our sample (see also Bennett et al., 2013), with $h = 0.693$, $\Omega_M = 0.286$, and $\Omega_\Lambda = 0.714$ and a Kroupa (2001) IMF.

3.2 Data

Our sample is based on galaxies with spectroscopic measurements from the Sloan Digital Sky Survey (SDSS) Data Release 7 with $0.01 < z \leq 0.2$ (Abazajian et al., 2009). We use a sample

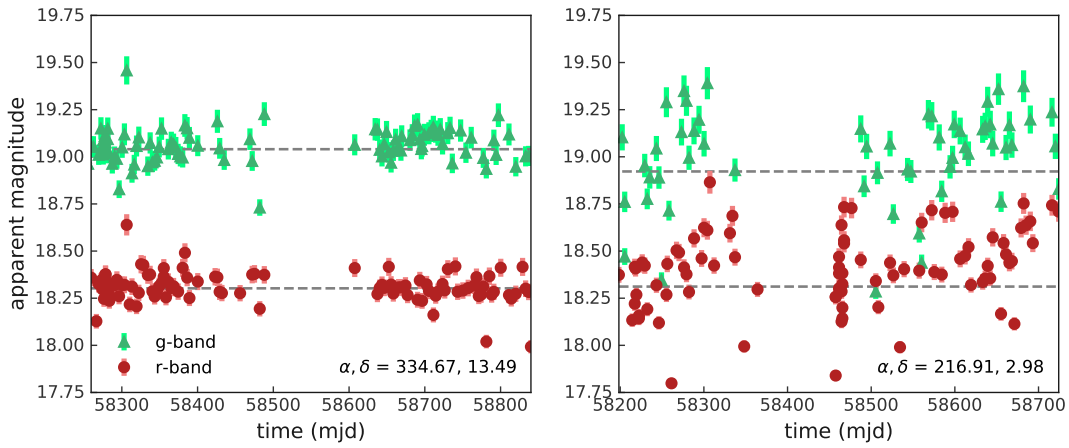


Figure 3.1: Two examples of galaxy lightcurves, with variability = 0.46 on the left and variability = 1.53 on the right as measured using Equation 3.1. r-band magnitudes are plotted as red circles, with g-band magnitudes plotted as green triangles, for illustrative purposes. Here, the dashed line represents the constant line of best fit through the photometric datapoints. These galaxies were chosen to have similar mean r magnitudes, similar number of photometric observations, and similar observation time periods.

of galaxies constructed by Omand et al. (2014)[1], which contains several value-added catalogues to use in addition, including the stellar mass (M_*) and star-formation rate (SFR) which come from the MPA-JHU value-added catalogue (Brinchmann et al., 2004)[2], and effective radii and bulge-to-total estimations from Simard et al. (2011)[3]. The stellar masses are calculated by comparing photometry fits to various stellar population models, and the star-formation rates are inferred from emission lines in the spectra for star-forming galaxies, and are estimated using the 4000 Å break for non-star-forming galaxies. Using the Zwicky Transient Facility (ZTF; DR7) catalogue search[4], we match these coordinates to photometric sources observed by ZTF (Bellm, 2014; Masci et al., 2019). We search for matching sources in a radius of 1 arcsecond; this radius was chosen to maximise matches while also avoiding contamination from non-matches. The resulting table provides object IDs that can be used to retrieve photometric lightcurves from ZTF. The photometric lightcurves were measured with psf-matching source extraction at each individual epoch and the range of magnitudes we cover are well detected in each frame. We restrict observation magnitudes to the r-band as it is the same band as the spectroscopic selection. We have aimed to make as homogeneous a galaxy selection as possible, and examining the r-band avoids the need for cross-band corrections.

In total, we retrieve 51068 non-empty lightcurves matched with the Omand et al. (2014) sample. In Figure 3.1, we show two example lightcurves in both the g- and r-band, although our variability measures use only the r-band. These were selected to highlight the difference between high and low variability (0.46, left; 1.53, right, see Section 3.3.1 for details on how the variability is calculated). The observations were taken over similar time periods (581 days, left; 526 days, right), similar number of photometric observations (191, left; 93, right) and similar mean r magnitudes (and thus similar photometric error bars). The variabilities exhibited here are typical of the ones we study in this paper – that is, they are not the result of systematic trends in the data, or 'one-off'

[1] http://cdsarc.u-strasbg.fr/viz-bin/cat/J/MNRAS/440/843

[2] https://wwwmpa.mpa-garching.mpg.de/SDSS/DR7/

[3] https://cdsarc.cds.unistra.fr/viz-bin/cat/J/ApJS/196/11

[4] https://irsa.ipac.caltech.edu/cgi-bin/Gator/nph-scan?projshort=ZTF

transient events. They seem to result from short-timescale apparent stochastic variability. By comparing the g- and r-band variability, we can see that there is clearly some very short timescale variation (< week) which appears in one band but not another. For instance, in the right plot of Figure 3.1 there is a large dispersion in the r magnitudes near mjd $\sim$ 58475 which do not appear in the g magnitude. Nonetheless, there is some more coherent variation in both magnitude bands near the beginning and end of the light curves which seems of a physical nature. Furthermore, it is difficult if not impossible to know what a source with truly zero variability would look like, due to photometric uncertainties. However, in this work we attempt to roughly demarcate between sources with small amounts of variability and sources with larger amounts of variability, and identify correlations and trends between them. To definitively identify a baseline of zero variability would be the subject of future work.

We extract emission line fluxes from Brinchmann et al. (2004) to construct a BPT diagram (Baldwin et al., 1981) in order to classify galaxies between AGN, star-forming, or composite, based on their emission line ratios.

3.3 Analysis and Results

3.3.1 Calculating variability

To ensure the robustness of the galaxy classes and variabilities, we impose a signal-to-noise cut on the SDSS spectral emission lines and a cut on the number of photometric observations from ZTF. We enact a signal-to-noise ratio cut of SNR > 3 for the Hα, Hβ, [NII]λ6584 and [OIII]λ5007 emission lines in order to classify between AGN-like emission and emission consistent with star-formation (SF) on a BPT diagram (Baldwin et al., 1981). The resulting BPT diagram is shown in Figure 3.2, along with the demarcation lines from the studies of Kauffmann et al. (2003b) and

Kewley et al. (2006). In the rest of the paper, we will refer to star-forming, composite and AGN, galaxies as labelled in the Figure. For instance, the composite galaxies are those with emission line ratios greater than the Kauffmann line and less than the Kewley line. Note that our classification does not require 'star-forming' galaxies to be forming stars at a particular rate, simply that their emission lines appear due to star-formation.

We restrict analysis to lightcurves with $n > 10$ photometric epochs from ZTF to ensure robust determination of the variability. However, we have verified that varying the cut-off for n does not quantitatively change the results of this paper. If a galaxy passes the SNR and epoch cuts, the variability is calculated. After SNR and epoch cuts, we are left with 16577 galaxies.

The variability is calculated using the logarithm of the reduced chi-squared $\left(\chi^2_\nu\right)$ of the magnitudes of each epoch, taking the errors on the magnitudes into account, as in Equation 3.1:

$$\begin{aligned} \chi^2_\nu &= \left[\sum_i^N \left(\frac{m_i - a}{\mathrm{d}m_i}\right)^2\right] / (N-1), \\ \text{variability} &\equiv \log_{10}\left(\chi^2_\nu\right), \end{aligned} \tag{3.1}$$

where N is the number of epochs, m_i is the magnitude measured at the ith epoch, a is the constant line of best fit through the datapoints and $\mathrm{d}m_i$ is the error on the magnitude at the ith epoch. We emphasise that variability, as referred to in this paper, is the logarithm of the reduced χ^2 as shown in Equation 3.1.

Under the hypothesis that the galaxy photometry is non-variable, the photometric data form a flat line as a function of date of observation. The reduced χ^2 tests this hypothesis, and provides a measure of how scattered the points are about the baseline, i.e. how variable the magnitudes of the galaxy are over the entire observation period. The result is a measure of the variability of the galaxies that depends on the magnitudes and the errors on the magnitudes. This means that dim galaxies with large uncertainties on the magnitude will have systematically underestimated variabilities compared to bright galaxies with small uncertainties, regardless of the actual variability of the source. To counteract this effect, we simulate variabilities and magnitudes of 10000 galaxies.

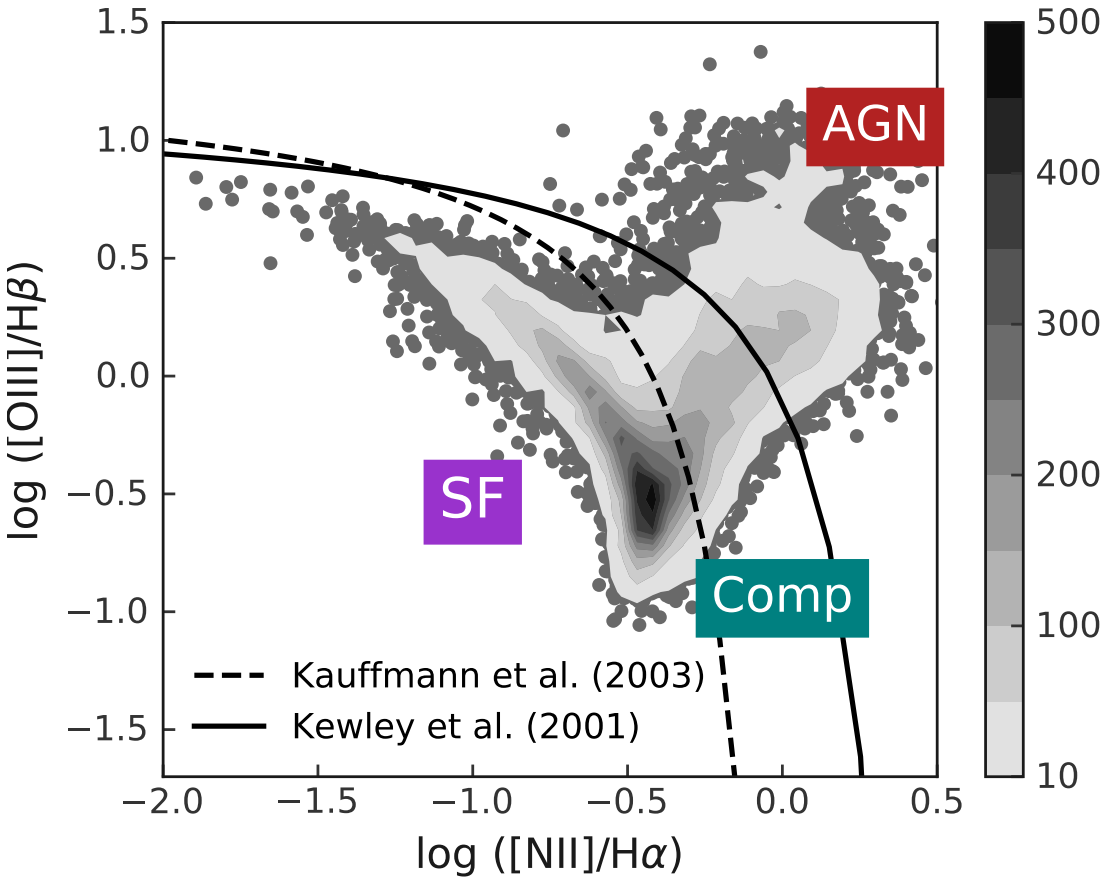


Figure 3.2: BPT diagram with demarcation lines from Kauffmann et al. (2003b) (dashed) and Kewley et al. (2006) (solid). The colourbar indicates number of galaxies found at each point in a contour region.

The full details of the simulations are included in Appendix 3.A. The simulations allow us to match a 'true' variability with the observed variability, at a given magnitude. Note that variability as described here is a dimensionless measure of of the scatter of points about a baseline, with variabilities > 1 roughly indicating a variable source.

For the purposes of this work, we decide to employ a magnitude cut when considering variabilities. This is because of the large disparity in distributions of magnitudes in AGN and star-forming galaxies, and that the variability calculation depends on the magnitude of the source. In effect, we want to examine the trends without the uncertainties that different magnitude ranges have on the calculated variabilities. Due to large overlap in the distributions, we choose $17 < m \leq 18$ to be the magnitude slice; note that results are not sensitive to the choice of magnitude slice.

One additional benefit of employing a narrow apparent magnitude cut is that it reduces the variation in source 'extendedness' on the sky. A potential source of non-physical variation in magnitudes is that ZTF psf-fit photometry depends on the on-sky extent of the galaxy. By restricting to a narrow apparent magnitude, we naturally reduce the variation in on-sky extent. Intrinsically fainter galaxies will be nearer than intrinsically brighter galaxies, but such fainter galaxies are also intrinsically smaller on average. In this way, the on-sky extent of our sample (as measured by the Petrosian radius) is quite narrow with a peak at ~ 2 arcsecs, and the vast majority of galaxies less than 5 arcsecs. This on-sky extent is also largely consistent with stellar mass, with a slight tendency for more massive galaxies to appear larger. As we will discuss later, the effect of increased variation from large galaxies would act to reduce our results rather than explain them.

The resulting distribution of variabilities for BPT diagram-defined AGN, composite galaxies, and star-forming galaxies are shown in Figure 3.3. In this Figure, the classes are individually normalized to have an area under their curve of 1. The number of galaxies in each of these classes is 2858 (AGN), 3729 (composite) and 9990 (star-forming). We see that, unexpectedly, star-forming galaxies exhibit higher levels of variability than their counterparts with more active black holes via

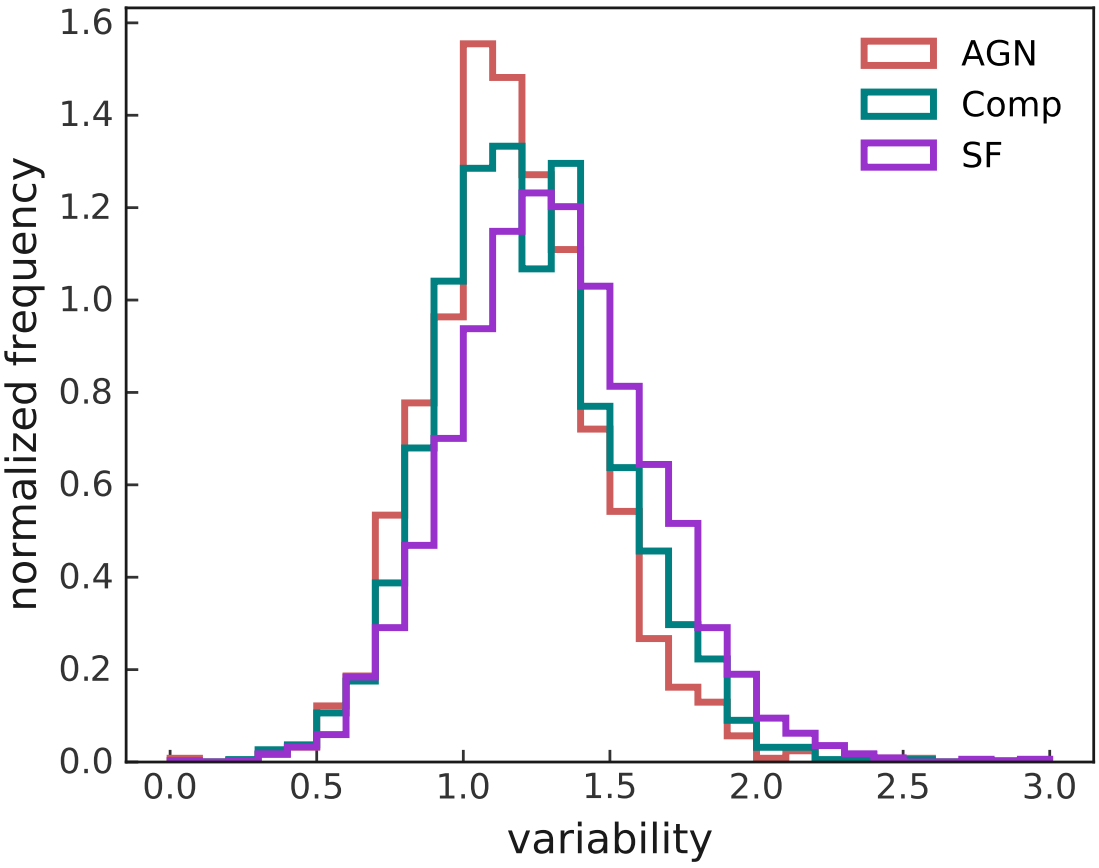


Figure 3.3: Variability distributions of AGN, star-forming galaxies, and composite galaxies. Here, distributions are normalised so that the area under each curve is 1.

emission line diagnostics. By fitting Gaussians to these histograms, we can measure the means and standard deviations of each distribution; we find $\sigma_{\rm AGN} = 0.299 \pm 0.021$, $\sigma_{\rm comp} = 0.298 \pm 0.026$ and $\sigma_{\rm sf} = 0.341 \pm 0.012$, and $\mu_{\rm AGN} = 1.153 \pm 0.016$, $\mu_{\rm comp} = 1.182 \pm 0.011$ and $\mu_{\rm sf} = 1.300 \pm 0.010$. We find slight differences in the widths of the distributions, but significant differences in the means, with $\mu_{\rm sf} > \mu_{\rm comp} > \mu_{\rm AGN}$. This result will be expanded upon and discussed throughout the rest of the paper.

3.3.2 Variability and galaxy properties

We may now explore the relationships between variability and a variety of galactic properties. First, it must be stressed that many of these properties are highly inter-dependent and thus the exact causality of the changes in variability is difficult to identify. Nevertheless, in this section we attempt to present the data as is, and more in-depth discussion will take place in Section 3.4. In Figure 3.4, we plot the mean variability in each stellar mass bin separated by emission type as determined by the BPT diagram. The AGN and composite galaxies have very similar mean variabilities as a function of stellar mass, with both increasing from variability ~ 1 at $M_* \sim 10^{9.5}$ $M_\odot$ to ~ 1.2 at $M_* \sim 10^{11.5}$ $M_\odot$. In contrast, in all but the most massive bins ($M_* > 10^{11} M_\odot$), the star-forming galaxies have mean variabilities that exceed that of AGN and composites. At $M_* = 10^{10} M_\odot$ the difference is 0.305 which is approximately 47 per cent of the width of the star-forming variability Gaussian, thus this is a significant deviation between the star-forming and AGN populations. Additionally, we see that the peak in mean variability occurs at $M_* \sim 10^{10.5} M_\odot$ for star-forming galaxies and starts to decline at higher masses. In contrast, the AGN and composite mean variabilities appear roughly monotonically increasing with stellar mass.

The interesting dependence of variability on stellar mass from Figure 3.4 suggests an investigation into the variability as a function of stellar mass and specific star-formation rate (sSFR). The specific star-formation rate is the star-formation rate divided by the stellar mass, and gives an indication of how rapidly the galaxy is forming stars relative to its past average. A sSFR of $\log(\mathrm{sSFR}) = -11 \mathrm{yr}^{-1}$ is commonly used as a demarcation between quenched and star-forming galaxies at $z = 0$, with star-forming galaxies having a higher sSFR (eg., Wetzel et al., 2013; Cleland and McGee, 2021). In Figure 3.5, we show the sSFR and stellar mass measurements for the AGN and star-forming classes and color each datapoint by their measured variability. We see that AGN (marked as circles) dominate the quenched region of the sSFR-M_* plane, and that SF galaxies (marked by stars) are typically found above this region, as expected.

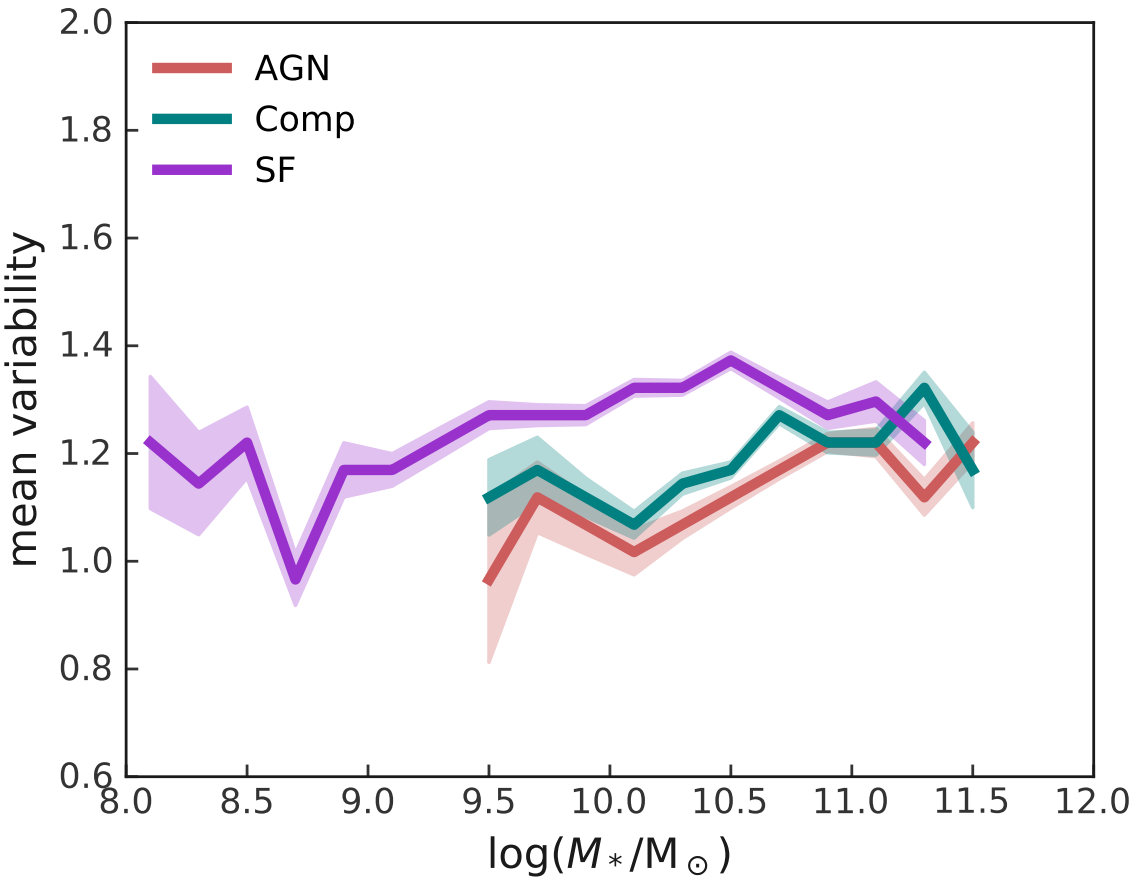


Figure 3.4: Mean variability binned by stellar mass, separated by emission type. Shaded regions indicate the standard deviation of the mean in that bin. Bins with fewer than 3 galaxies are omitted for clarity.

Note that in this Figure, composite galaxies are omitted for clarity. Interestingly, by examining the figure, it appears that there is a band of high variability in the intermediate sSFR region, roughly $10^{-11}\text{yr}^{-1} < \text{sSFR} < 10^{-10}\text{yr}^{-1}$. This is where the vast majority of the 'purple' points from the high end of the variability color map lie. It also appears that both the high and low end of the sSFR distributions have lower variabilities than this middle region.

In Figure 3.6, several trends emerge with respect to the mean variability binned by various galactic properties for the three galaxy classes. In the left panel, we plot the mean variability with respect to the bulge-to-total ratio (B/T) as measured by Simard et al. (2011) using bulge to disk decompositions. We see that for the most part, the mean variability is similar for each class and is steadily declining with the bulge-to-total ratio, deviating only at extreme values of B/T. However, this similarity of the galaxy classes does not hold when looking at the half-light radius (R) in the centre panel. We see that at almost all radii $R \lesssim 7$ kpc, star-forming galaxies have higher mean variabilities in each bin than composite galaxies and AGN. This is explained by the fact that at the same galaxy size, star-forming galaxies will typically have less massive bulges than AGN do, and thus will have a smaller B/T. As we see in the left panel of Figure 3.6, galaxies with smaller B/T have higher mean variabilities, so the excess in mean variability for star-forming galaxies in the centre panel is accounted for. The right panel in Figure 3.6 is similar to Figure 3.5, but better illustrates the trend we identified in which variability is highest in intermediate sSFR of star-forming galaxies. Interestingly, we also see stark declines in mean variability at $\log(\text{sSFR}) \gtrsim -10\text{yr}^{-1}$, indicating it is not sufficient to have high rates of star-formation to have high levels of variability.

3.4 Discussion

We have found several empirical relations. We see that galaxies whose optical line emission is predominately the result of star-formation have higher variabilities (in the mean) than galaxies

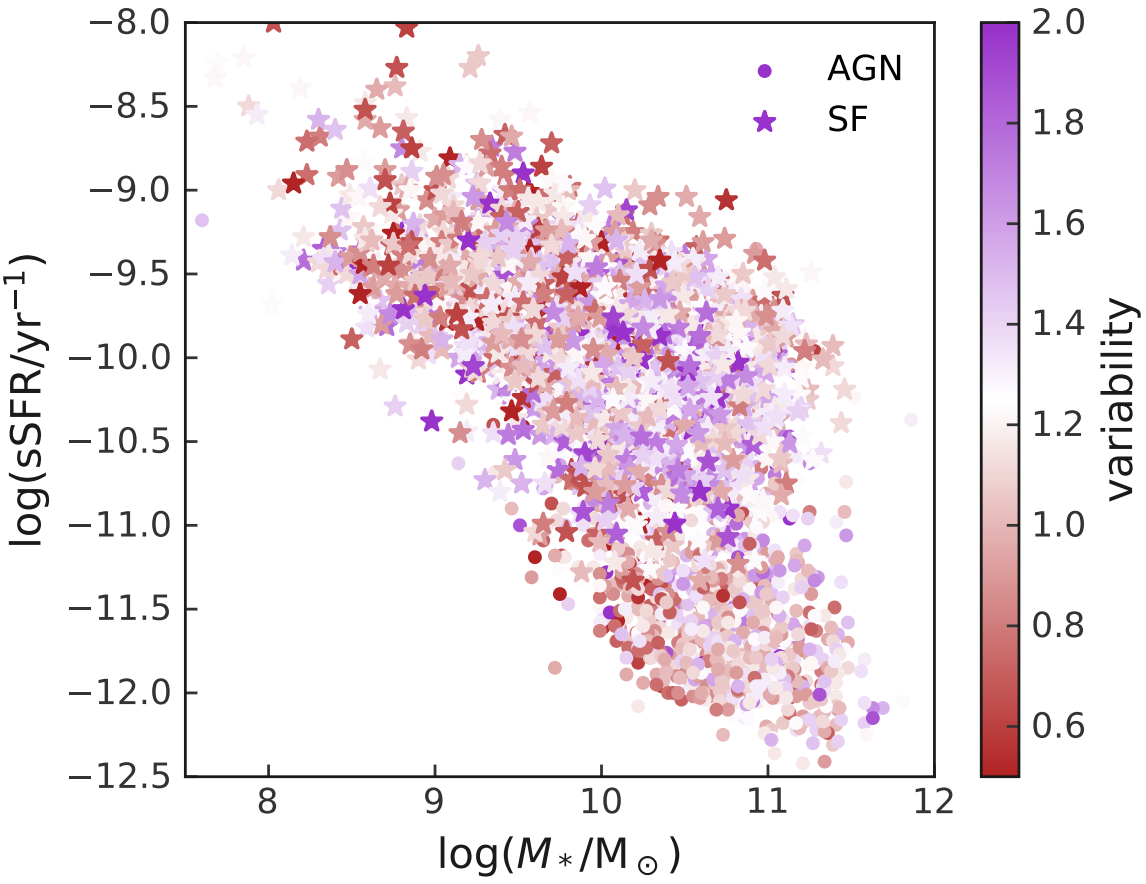


Figure 3.5: The relation between sSFR and M_* of galaxies, separated by emission type (AGN [circle] and star-forming [star], composite galaxies are omitted for clarity), and colour-coded by variability.

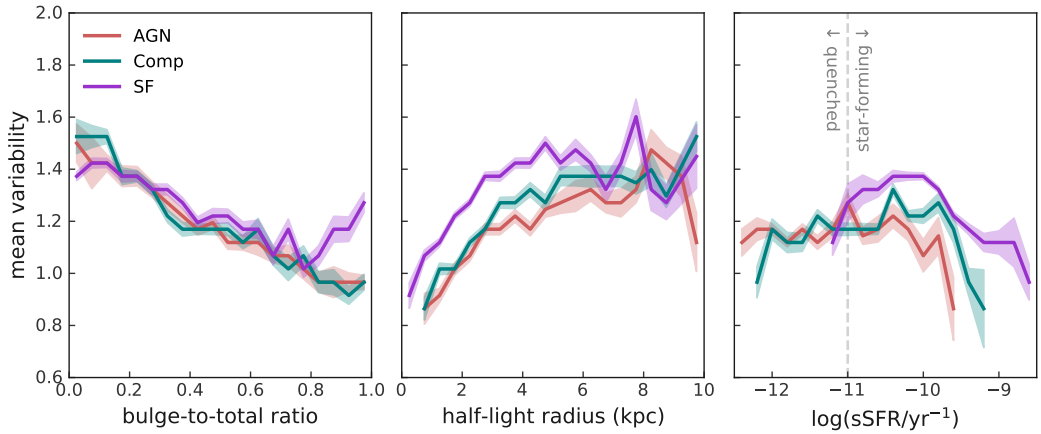


Figure 3.6: Mean variability binned by different quantities, separated by emission type. Shaded regions indicate the standard deviation of the mean in that bin. Bins with fewer than 3 galaxies are omitted for clarity. Left: mean variability against bulge-to-total ratio. Centre: mean variability against half-light radius. Right: mean variability against $\log(\mathrm{sSFR}/\mathrm{yr}^{-1})$.

whose optical line emission is from AGN or a composite of AGN and star-formation. Further, we see that star-forming galaxies have higher variabilities at all stellar masses than composite or AGN. Interestingly, we showed that at fixed bulge-to-total ratio the mean variabilities of all three classes were similar, but at fixed half-light radius, star-forming galaxies had higher mean variabilities than seen in AGN or composite galaxies. Perhaps most interestingly, we found variability is strongly dependent on the galaxy location within the sSFR-M_* plane. The star-forming galaxies have mean variability higher than either the AGN or composite galaxies at any fixed sSFR, but star-forming galaxies have a peak in their variability just 'above' the quenched demarcation line. This intermediate region of sSFR is consistent with galaxies in the 'green valley' (Salim, 2014).

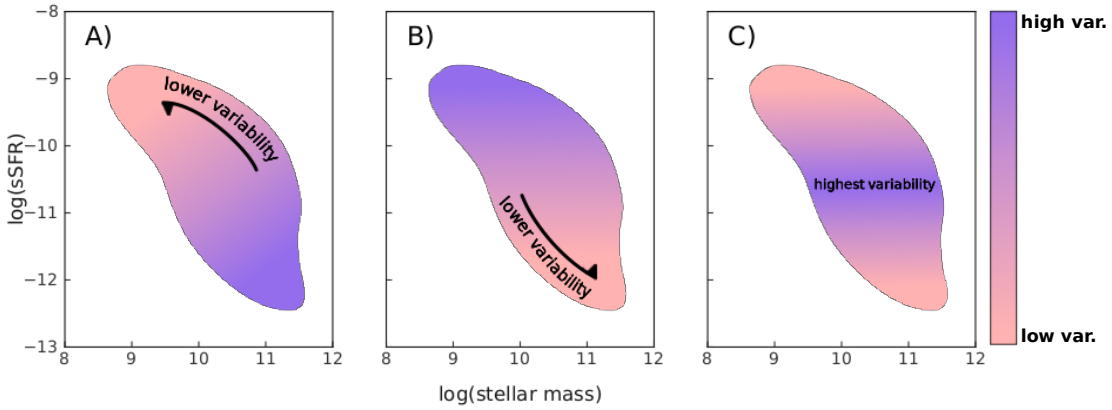


Figure 3.7: Three hypothetical scenarios that could possibly describe the behaviour of variability in sSFR-M_* space. Scenario A) describes a situation where the BPT identifies all the AGN, and so variability is tightly linked to stellar mass and lack of star-formation. Scenario B) illustrates the idea of variability being dependent on gas content in a galaxy, so higher gas content implies higher SFR implies higher variability. Scenario C) is the situation we see in Figure 3.5, where a galaxy funnels gas into the centre after some time forming stars, exhibits variability, consumes the gas and quenches.

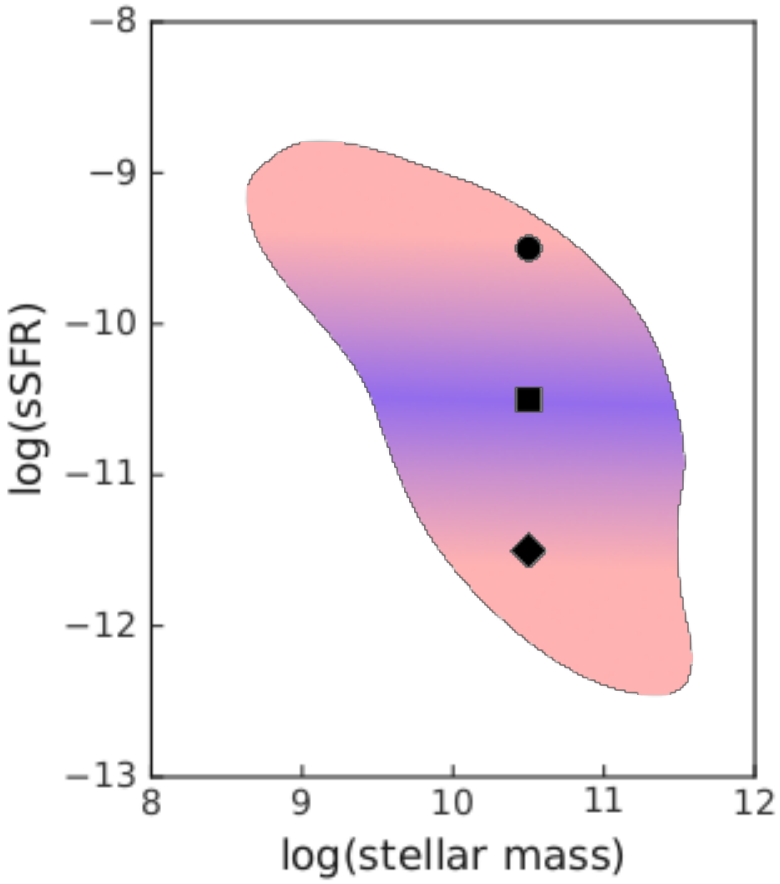


Figure 3.8: Scenario C) illustrated further; see text for full details. The colourbar is as in Figure 3.7, where pink denoted low variability and purple denotes high variability. The symbols refer to different stages of a galaxy's evolution, as explained in the text.

3.4.1 Source of the variability

Until now, we have not discussed what actually causes the variability we see in these galaxies. There are at least three possibilities: 1. unaccounted-for errors in the photometric measurements, 2. intrinsic variability in the light from the dust/gas/stars in the galaxy, and 3. intrinsic variability caused by emission from the central black hole and associated accretion disk. We will look at each of these possibilities and the expectations of their signal.

The most obvious explanation for variability in photometric data is an unaccounted-for variation in the photometric measurements – whether from inaccurate zeropoint calibration, unmatched aperture measurements (from seeing, etc) or a similar observational problem. While it is difficult to rule this out as a factor in all of the computed variabilities, we have taken a number of steps to minimize the possibility for error. For instance, we have principally examined the mean variability for wide classes of galaxies rather than the 'extremes' of a particular distribution. We have limited our sample of galaxies to only one magnitude of apparent magnitude ($17 < m \leq 18$) to avoid the reliance on photometric error bars to be well represented across a wide dynamical range. Finally, if the mean variabilities we have measured were completely determined by unaccounted-for photometric errors, we would not expect these to show the dependence on physical galaxy properties that we have seen in the previous section. The main way that a physical property could induce photometric errors would be through a correlation of the errors with the physical extent of the galaxy. The on-sky extent of a galaxy is likely to have a positive correlation with photometric errors. However, as we have discussed earlier, our narrow magnitude cut limits the correlation between the physical extent of the galaxy and the 'on-sky' extent. We have found the galaxies with higher stellar mass tend to have slightly higher on-sky extents on average. But, this would tend to induce increased errors as a function of stellar mass in the opposite manner of our results. Given this, it is worth looking at the possible causes of intrinsic variability in the galaxy light.

The next possibility is that the variability comes from the interstellar gas/dust or stars in the

galaxy itself. The galaxies in this paper have half-light radii of $\sim 1 - 10$ kpc, which would imply that the timescale for *complete* variability across the galaxy would have to be greater than $\sim$ 3000 - 30,000 years (assuming unimpeded light travel across the galaxy r/c). However, the variability we see is on the $\sim$ week to year timescale. Thus, the variability would have to be on smaller scales - individual stars or gas clouds. In this case, the individual stars and clouds would have to have widely and rapidly varying luminosities to avoid being washed away by the uncorrelated variations of other stars. This is clearly not possible for the normal variation of stars. The only possibility would be the large variation caused by supernovae or similar cataclysmic events. However, the variation we measure appears stochastic (Figure 3.1) rather than the result of a particular rare event. Although there have been recent suggestions that even supernova or stellar variation can mimic some of the AGN-like variation (Burke et al., 2020), these events are still expected to be rare ($\sim 0.1 - 2$ per 100 yr for a star-forming galaxy, Tammann et al., 1994). As we are principally looking at the mean variability, we are not driven by these uncommon occurrences.

That leaves the possibility that the variation we measure is due to variable emission from the central black hole/AGN in each galaxy. The scale of central black holes and their accretion disks are thought to be < 0.1 pc which would imply light crossing times of < 100 days (Hawkins, 2007; Morgan et al., 2010). Although it is unlikely that global changes in the accretion disks are made on that timescale, it does indicate that large changes are possible on short timescales possibly through thermal fluctuations of the UV-emitting region (Kelly et al., 2009; Burke et al., 2021). Indeed, direct observations of AGN have shown that $>$ order of magnitude changes are possible on hour to year timescales (McHardy et al., 2006; Hickox et al., 2014). Given the known variability of AGN, and the lack of an viable alternative source for the variability, in the rest of the paper will we consider what implications this variability has for our understanding of galaxy formation if it is due to AGN.

3.4.2 Implications for galaxy formation if variability is from AGN

Our finding that higher variability occurs at particular locations depending on galaxy type, stellar mass and specific star-formation rate may seem counter-intuitive to the current understanding of AGN physics. In this section, we attempt to illustrate a possible scenario for the physical mechanisms behind these results, and rule other possibilities out.

In Figure 3.7, there are 3 plots illustrating possible physical scenarios which could be expected to occur in Figure 3.5, labelled A), B) and C). These three scenarios are roughly: A) variability traces the appearance of emission line galaxies classed as AGNs, B) the variability traces the global sSFR, or C) variability traces those galaxies that are in the process of being most actively quenched. We will now discuss each in turn.

In scenario A), we illustrate the variability trend in sSFR-M_* assuming that a BPT diagram correctly and completely identifies all the AGN in the galaxy sample. In this case, any star-forming galaxy will neither have an active black hole nor exhibit variability. Tracing these emission classes would result in the behavior shown in Figure 3.7 A). We see the highest variability would be found at the low-sSFR–high-mass end of the plot. Moving up the plot, variability decreases. In essence, scenario A) implies that variability is correlated with stellar mass, and anti-correlated with star-formation. While the assumption that star-forming galaxies have no active black hole is extreme, it is often treated as such when analysing star-forming galaxies.

In scenario B), we show the variability trend assuming that variability is fueled by global gas content in the galaxy, and thus is correlated with sSFR. This scenario would result in the behavior illustrated by Figure 3.7 B), which shows a region of high variability at high sSFR, with variability decreasing as sSFR decreases. While this complete correlation may seem extreme, it is a natural outcome of the often assumed tight relation between star-formation and black hole growth (eg., Hopkins et al., 2006).

However, neither scenario A) nor B) resemble what is seen in Figure 3.5. Figure 3.7 C) is intended to schematically represent what is actually happening; rather than finding high variability at the extremes of the sSFR-M_* plot, we see a band of high variability at intermediate sSFR. We saw that a band of high variability occurred in the middle range of sSFR values, and so, the data rules out either of the extreme cases presented in A) and B). Assuming the variability traces AGN activity, then 1) there are active black holes in galaxies classified as star-forming via their emission line ratios and 2) there is not a direct instantaneous relation between the sSFR and the black hole growth rate. Scenario C) may imply a convolution of scenario A) and B).

Scenario C) can be described using the 3 points in Figure 3.8; a circle, a square, and a diamond. The circle represents a galaxy in the early stages of its evolution, that has a high sSFR. Our data imply this galaxy has gas fuelling star-formation but relatively little gas feeding the black hole, thus, the galaxy shows the required low variability. The square represents a galaxy which now has gas feeding the black hole, and also has gas fuelling star-formation. The presence of gas in the centre of the galaxy provides the required variability. However, it would appear that due to AGN feedback and gas consumption, the galaxy's star-formation drops. So, the square galaxy has an intermediate sSFR and high variability. After some time, AGN feedback suppresses star-formation, thus the galaxy becomes quenched, as indicated by the diamond. Due to gas consumption, gas can no longer feed the black hole, and so the variability decreases, as required.

This scenario is consistent with other results throughout this work; in Figure 3.4, mean variability in SF galaxies peaks at $M_* \sim 10^{10.5}$ $M_\odot$, implying that as the bulge grows in a SF galaxy, variability increases until the point where the AGN 'turns on' (as determined by the galaxy emission). Similarly, in Figure 3.6, we see that galaxies with underdeveloped bulges have higher variabilities compared to galaxies which have had longer to build their bulges. In our possible scenarios, we have have not explicitly addressed the possibility that host galaxy dilution plays some role. For instance, two black holes of the same mass, accreting at the same rate, would likely have different contributions to the galaxy-wide variability if put in two galaxies with significantly

different luminosities. It is very hard to rule out this effect playing a role, but we expect it would work to reduce the trends we see. That is, at a fixed stellar mass, star forming galaxies will have higher luminosities than AGN or composite galaxies – because their more recent star formation leads to lower M/L ratios. So, we would expect host-dilution to muffle the signal in SF galaxies. Given we see the highest signal at fixed stellar mass in the SF galaxies, we expect this effect is not dominant.

3.5 Conclusions

We have combined photometric lightcurve data from the Zwicky Transient Facility with spectroscopic data from the Sloan Digital Sky Survey to examine the variability of $\sim$ 16500 galaxies at z < 0.2. Using the value-added measurements of SDSS, we examine this variability as a function of stellar mass, specific star-formation rate, galaxy class as determined by emission line ratios, effective radii and bulge to total ratios. Our main findings can be summarised as:

- The photometric variability of star-forming galaxies (with their class determined by their location in the BPT diagram) is higher than the variability of either the composite or AGN-dominated galaxies. Restricting to a narrow slice in apparent magnitude ($17 < m \leq 18$), we find the median variability of star-forming galaxies is 1.289, while it is 1.150 for AGN and 1.190 for composite galaxies.

- The elevated variability in star-forming galaxies compared to AGN or composite galaxies is also seen at fixed stellar mass for all but the highest ranges ($> 10^{11}$ $M_\odot$).

- The highest variabilities occur in a well defined region of the sSFR-M_* plane – in a band with -11 > log(sSFR/yr^{-1}) > -10. In this region, we again see that star-forming galaxies have the highest variabilities of the three galaxy classes.

- The differences in mean variabilties of the galaxy classes largely go away when compared at fixed bulge-to-total ratio (for $B/T < 0.8$), but remain for small half-light ratios < 6 kpc.

We argue that the best explanation, based on timing arguments, for the observed behavior of mean variabilities is that the variability is driven by AGN activity. Under this assumption, we argue this provides evidence that central supermassive black holes exist in star-forming galaxies, including in low mass galaxies. We also argue that the appearance of the mean variabilities rules out an exact correlation between instantaneous star-formation and black hole growth. Finally, we argue this enhanced variability is evidence that AGN feedback is shutting down the star-formation in actively star-forming galaxies. Taken as a whole, these results indicate that emission in the form of star-formation may obscure a low-mass AGN, and hide the dramatic effects the AGN are having on galaxy evolution.

In our work, we have attempted to measure the variation of a well-selected sample of galaxies in a 'source-agnostic' way. Given our current explanation that this variation arises chiefly from AGN activity, in future work we will explore further measures to quantify the AGN. We plan to use both the g- and r-bands to measure the variability with other techniques such as by quantifying the RMS of the intrinsic source variability (Shen et al., 2019), and comparing to expected summary statistics of stochastic variations (Kelly et al., 2009; Kozłowski, 2016). We also expect to tie the requirements for the length of light curves more directly to possible time-frames which maximize the coverage of relevant BH timescales (eg., Burke et al., 2021).

Appendix

3.A Simulations of recovered variability

These simulations are motivated by the fact that without them, low variability is biased towards bright objects with small uncertainties. To account for this effect, without discarding the uncertainties entirely, we begin with a sample of 10,000 galaxies to which we randomly assign a variability and a magnitude. Both the variability and magnitudes are taken independently from uniform distributions. For clarity, this variability will be referred to as the 'true' variability. We reconstruct a lightcurve using the true variability and some Gaussian scatter. In order to reconstruct the lightcurve from the variability, an average value for dm must be assumed (see Equation 3.1). This value is taken from the best fit line through the magnitude uncertainties with respect to the magnitudes, as shown in Figure 3.9.

When the simulated observations are in place, we assign a different uncertainty on the magnitude. This uncertainty is drawn from a sample of uncertainties which is based on the real uncertainties in the data for a given magnitude bin. We now recalculate the variability in the exact same way; this variability may be thought of as the 'reco' variability, analogous to the observed variability in the real data. This allows for a direct comparison between the reco variability and the true variability, at a given magnitude. The resulting scatter acts as an uncertainty on the true variability.

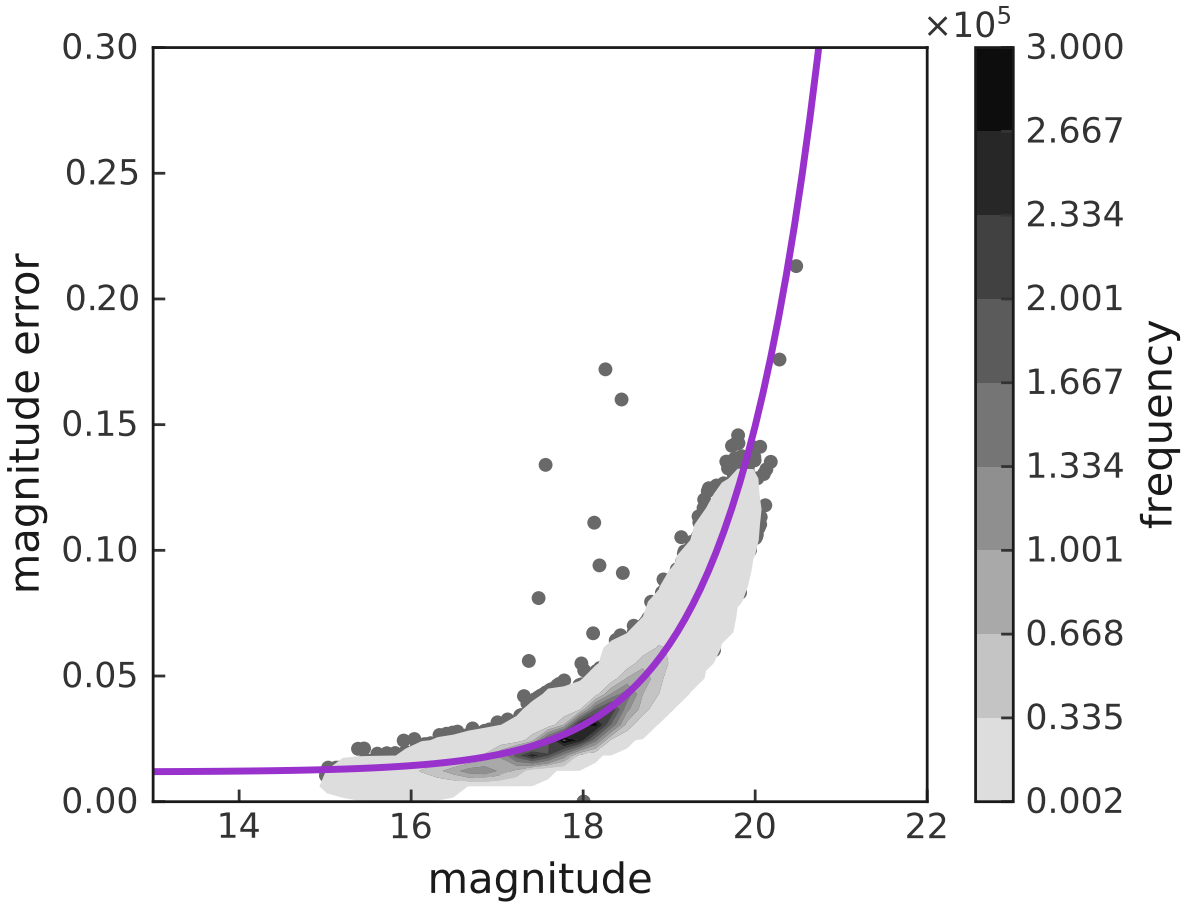


Figure 3.9: Magnitude against magnitude uncertainty for each epoch in the ZTF dataset. For plotting purposes, the number of datapoints has been reduced from 10^5 to 10^4.

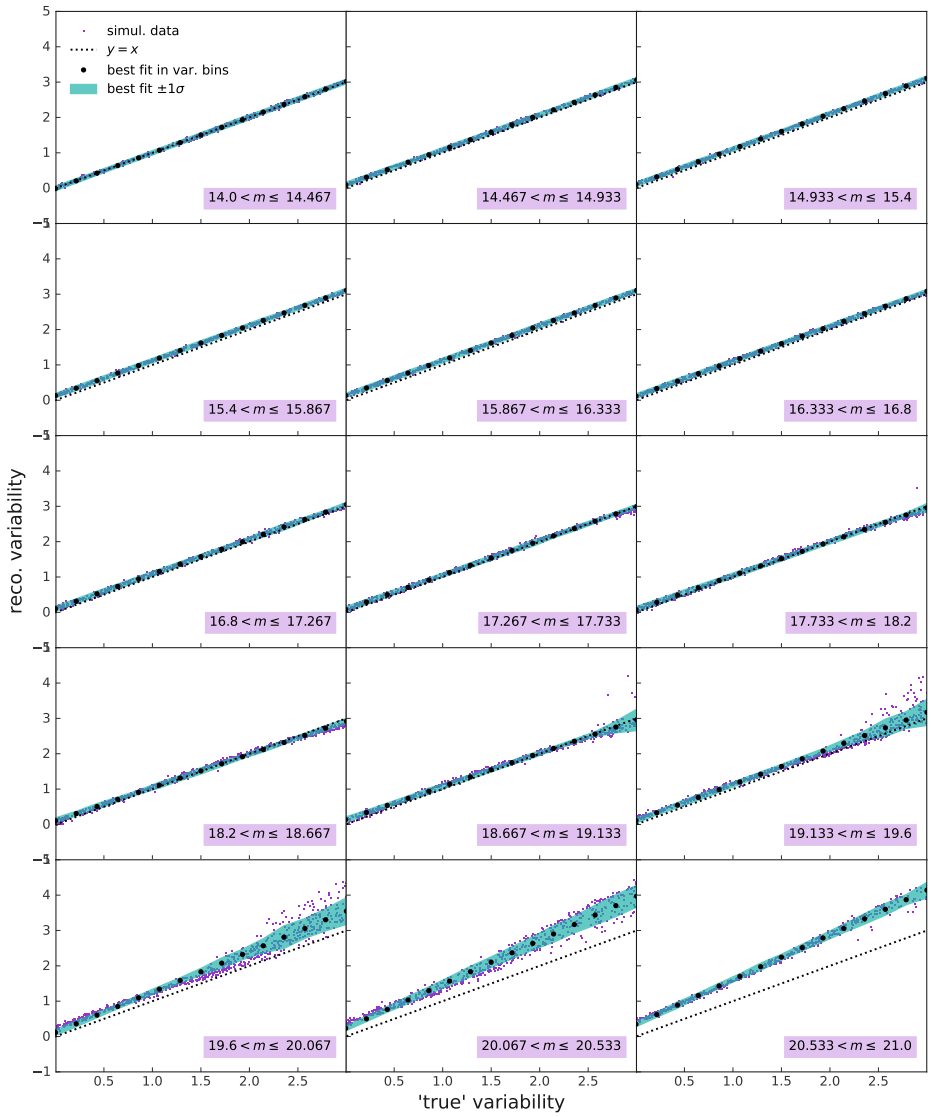


Figure 3.10: Example plots of the relation between the true variability and the reco variability, in various magnitude bins. The purple points are the simulated datapoints; the black points are the best fit line through the datapoints; the teal shaded region shows the 1σ area around the best fit; the black dashed line shows the $y = x$ line for illustrative purposes.

In practice, we take the observed variabilities (equivalent to reco variabilities) and match them up to the true variabilities, at a given magnitude. This is illustrated in Figure 3.10, where a small number of bins is shown for clarity purposes. The actual number of bins used is larger, and was chosen to minimize scatter while also avoiding overbinning. Note that although the scatter in dimmer magnitude bins appears significant in the Figure, the actual scatter is much smaller and negligible. These true variabilities are injected back in to analysis.

Chapter Four

Superluminous supernova host galaxies

This Chapter consists of the paper "Metallicity beats sSFR: The connection between superluminous supernova host galaxy environments and the importance of metallicity for their production", (Cleland et al., 2023), published in MNRAS.

We analyse 33 Type I superluminous supernovae (SLSNe) taken from ZTF's Bright Transient Survey to investigate the local environments of their host galaxies. We use a spectroscopic sample of galaxies from the SDSS to determine the large-scale environmental density of the host galaxy. Noting that SLSNe are generally found in galaxies with low stellar masses, high star formation rates, and low metallicities, we find that SLSN hosts are also rarely found within high-density environments. Only 3^{+9}_{-1} per cent of SLSN hosts were found in regions with 2 or more bright galaxies within 2 Mpc. For comparison, we generate a sample of 662 SDSS galaxies matched to the photometric properties of the SLSN hosts. This sample is also rarely found within high-density environments, suggesting that galaxies with properties required for SLSN production favour more isolated environments. Furthermore, we select galaxies within the Illustris-TNG simulation to match SLSN host galaxy properties in colour and stellar mass. We find that the fraction of simulated galaxies in high-density environments quantitatively matches the observed SLSN hosts only if we restrict to simulated galaxies with metallicity $12 + \log(\mathrm{O/H}) \leq 8.12$. In contrast, limiting to only

the highest sSFR galaxies in the sample leads to an overabundance of SLSN hosts in high-density environments. Thus, our measurement of the environmental density of SLSN host galaxies appears to break the degeneracy between low-metallicity or high-sSFR as the driver for SLSN hosts and provides evidence that the most constraining factor on SLSN production is low-metallicity.

4.1 Introduction

While the detection rates of supernovae have rapidly increased over the last decade or so, thanks to wide-field high-cadence surveys such as Pan-STARRs (Chambers et al., 2016), ATLAS (Tonry et al., 2018) and ZTF (Bellm et al., 2019), superluminous supernovae (SLSNe) remain a rare and elusive transient event. SLSNe were originally classed as a supernova event that is 10-100 times brighter than typical supernovae (Quimby et al., 2011; Gal-Yam, 2012), however are now classified by their unique spectra (e.g. Lunnan et al., 2018; Quimby et al., 2018; Angus et al., 2019). Their lightcurves differ from those of other supernovae as they are both broader and brighter. There are two classes of SLSNe: Type I and Type II. Type I SLSNe (often referred to as simply SLSNe, a convention we adopt in this work) are dominated by OII absorption lines at maximum luminosity, while Type II SLSNe exhibit sharply peaked hydrogen emission lines from circumstellar interaction. The physical mechanisms which cause Type I SLSNe remain a topic of debate, with mechanisms such as a central engine in the form of a magnetar (see e.g. Kasen and Bildsten, 2010; Inserra et al., 2013; Nicholl et al., 2017) or interaction with the circumstellar medium (see e.g. Smith and McCray, 2007; Chevalier and Irwin, 2011; Chatzopoulos et al., 2012; Ginzburg and Balberg, 2012) being proposed as possible power sources for the increased luminosity.

We can use properties of their host galaxies to infer the conditions required for a SLSN to occur. This can help constrain the processes at work. SLSNe have been found mostly in low-mass galaxies, with very few being found in host galaxies with stellar mass $> 10^8$ $M_\odot$ (Schulze et al.,

Sample	# obj.	Redshift	Med(z)	Magnitude	Med(M_i)	Description
SLSN-g	33	0.064, 0.39	0.159	−22.74, −15.32	-18.41	SLSN host gals.
SDSS-m	662	0.036, 0.312	0.117	−22.196, −16.709	-19.632	SDSS phot-z gals. matched to SLSN-g
SN-Ia	3268	0.001, 0.156	0.065	−26.56, −11.56	-20.76	Type Ia host gals.
Spec-z	300000	0.00, 0.40	0.144	−31.214, −10.006	-22.385	SDSS spec-z gals.

Table 4.1: Descriptions of each of the samples used. The columns are the name of the sample, the number of objects in the sample, the minimum and maximum of the redshift, the median of the redshift, the minimum and maximum of the absolute magnitude, the median of of absolute magnitude, and the description of the sample.

2018). This is surprising, as one might expect that with more stars comes more supernova events (Sullivan et al., 2006; Smith et al., 2012; Wiseman et al., 2021, see also Perley et al., 2016b). Various authors have found that SLSN host galaxies typically have high specific star-formation rates ($\sim 10^{-9}$ yr^{-1}, Neill et al., 2011; Leloudas et al., 2015; Angus et al., 2016), leading to the idea that SLSNe may be the first stars to explode following a starburst. Leloudas et al. (2015) note that SLSN host galaxies have properties which are consistent with extreme emission line galaxies (EELGs), i.e. high-sSFR and also highly ionised gas. Meanwhile, Lunnan et al. (2014), Chen et al. (2017c) and Perley et al. (2016a) argue that the low-metallicity observed in SLSN hosts is the more important factor in the production of these rare transients, and that their low metallicities can explain the extreme energies seen (Chen et al., 2013). Nevertheless, since dwarf galaxies tend to have both low metallicities and bursty star-formation histories, and the production of SLSNe appears averse to high-metallicity and low specific star-formation rate (Schulze et al., 2018), there is a degeneracy regarding which of these factors is more critical.

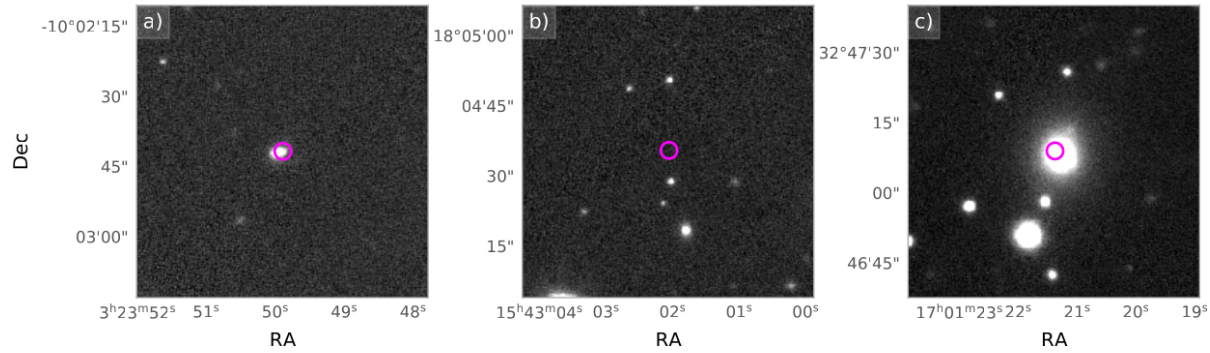


Figure 4.1: PanSTARRS *i*-band cut-out images (Flewelling et al., 2020) of SLSN sources and of a SN Type Ia host. Panel a) shows object ZTF21aaarmti, panel b) shows object ZTF22aalzjdc and panel c) shows object ZTF18aangpkx. The magenta circle in each panel depicts the location of the source. In panel b), no host galaxy was found for the source. The host galaxy in panel c) is in a higher-density environment than the SLSN hosts; see Section 4.3.1 for details. The absolute magnitude of the host galaxy in panel a) is $M_i = -21.36$ and its redshift is $z = 0.193$. The absolute magnitude of the host galaxy in panel c) is $M_i = -22.67$ and its redshift is $z = 0.070$. The redshift of the SLSN source in panel b) is $z = 0.200$. The size of each of the images is 62.50″.

It is well known that the local environment of galaxies, that is whether a galaxy is located within a galaxy group or a galaxy cluster or it is isolated, has a profound effect on a number of galaxy properties, including the metallicity (Tremonti et al., 2004; Ellison et al., 2009; Cooper et al., 2009), star formation rate (Wetzel et al., 2013; Cleland and McGee, 2021) and overall evolution of the galaxy (Dressler, 1980). Gravitational interactions between galaxies can disturb the gas and dust which fuels star-formation, leading to starburst phases, or similarly galaxies may merge which will also have an effect on the star-formation rates of the galaxies involved. Conversely, high-density environments may cause the quenching of star-formation in an infalling galaxy. It naturally follows to investigate the local environment of SLSNe host galaxies to uncover any environmental factors that may impact SLSNe rates. Ørum et al. (2020) find that up to 50 per cent of superluminous supernova host galaxies have at least one companion within 5 kpc, which they use to explain the increased star-formation rates required for SLSNe to occur. However, for the purposes of this work we are interested in the overall density of the local environment of the SLSN host galaxy. That is, a close companion galaxy of arbitrary stellar mass within kiloparsecs of the supernova host galaxy does not necessarily lead to the same environmental effects at larger scales (e.g., Mpc). In order to probe for such effects, we aim to use bright galaxies as a proxy for density, noting that this is a first order approach, with the absolute magnitude of galaxies roughly tracing stellar mass. By investigating the environments of these galaxies in this way, we aim to break the degeneracy between the requirements of low-metallicity and high specific star-formation rate for SLSN production.

In this work we identify isolated SLSNe and SLSNe in groups, and compare between various host galaxy properties. We also compare against Type Ia supernova host galaxies, which occur in a wider variety of host galaxies. We then investigate these host galaxies further within the Illustris-TNG simulation suite, by exploring the metallicities and specific star-formation rates of a sample of simulated galaxies with observational properties similar to those of SLSN hosts.

The paper is structured as follows: in Section 4.2, we describe the data used and how it was obtained; in Section 4.3 we explain the results and discuss their implications; finally in Section 4.4

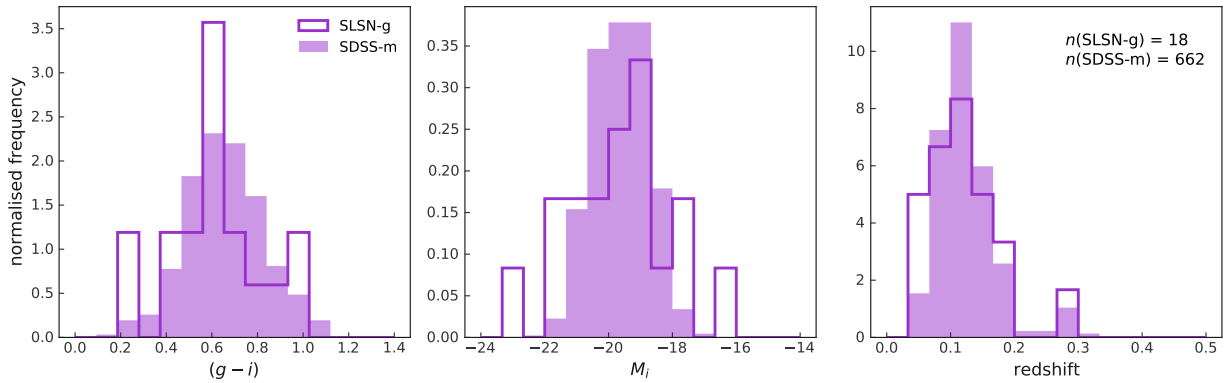


Figure 4.2: Histograms of the colours, absolute magnitudes, and redshifts of galaxies in SLSN-g with reliable photometry compared to the matched SDSS sample. KS-tests result in p-values of 0.46, 0.36, and 0.75 respectively, validating that the SLSN-g and SDSS-m samples match each other.

we summarise our findings. For the computation of cosmological distances, we use a flat universe with $H_0 = 70.2$ and $\Omega_m = 0.277$.

4.2 Data

We obtain coordinates, redshifts and host photometry ($g-i$ colours and M_i absolute magnitudes) of 55 Type I SLSNe (hereafter simply referred to as SLSNe) and 4816 Type Ia supernovae from the ZTF Bright Transient Survey[1] (BTS; Masci et al., 2019; Perley et al., 2020c). This was the full sample of Type I SLSNe and Type Ia SNe available on the BTS at the time of analysis (September 2022). The BTS is used to obtain properties on supernova events and their host galaxies due it being a well-defined sample with a limiting magnitude of $\approx$ 18.5 mag that selects for nearby events with a higher chance of host detection. The supernovae in this sample have been classified spectroscopically, and by a variety of research groups. Table 4.2 lists and cites the classification

[1]https://sites.astro.caltech.edu/ztf/bts/bts.php

group for each SLSN. The code SHERLOCK[2] is used to cross-identify for a host galaxy and its photometry (Smith et al., 2020); this information is available directly on the LASAIR broker (Smith et al., 2019) for each source. Some sources have no catalogued host, and are marked as 'orphans'. See Figure 4.1 for examples of a SLSN source with a host detection (left panel) and a SLSN source where no host was detected (middle panel). We denote the SLSN host galaxy sample as SLSN-g, and the Type Ia supernova host galaxy sample as SN-Ia.

We obtain a spectroscopically-redshifted sample of 300000 random galaxies (Spec-z) from the Sloan Digital Sky Survey (SDSS) DR17 (Smee et al., 2013; Blanton et al., 2017; Abdurro'uf et al., 2022), such that their redshifts are local and precisely-known, $0 < z < 0.4$. We also obtain 16494 random photometrically-redshifted galaxies from SDSS DR17 (Fukugita et al., 1996; Gunn et al., 1998; Gunn et al., 2006; Doi et al., 2010) to better match the parameter space of the SLSNe sample, with $0 < z < 0.4$, such that $z_{\rm err} < 0.1$ and $z_{\rm err}/z < 0.5$. Both samples were obtained using the SDSS query service CasJobs[3]. For each sample of supernova hosts, we restrict to sources within the on-sky footprint of the spectroscopic sample, resulting in 35 SLSNe (18 with detected hosts) and 3450 Type Ia supernovae.

4.2.1 Matched sample generation

Since the number of SLSN host galaxies is so low, it is desirable to generate a matched galaxy sample, based on SLSN host galaxy properties. This means we can make statistical comparisons of SLSN host-like galaxies, but on a much larger sample of galaxies. The properties of the SLSN host galaxies are based on their photometry, so we generate a sample of galaxies that are matched based on photometric properties such as absolute magnitude and colour. We generate this matched sample to the SLSN host galaxies from the SDSS photometric galaxies (Cooper et al., 2009). For

[2]https://github.com/thespacedoctor/sherlock

[3]http://cas.sdss.org/dr17/

each SLSN host galaxy, we randomly search for a photometric galaxy within a sphere in parameter space according to Equation 4.1:

$$\left(\frac{\Delta\text{colour}}{0.2}\right)^2 + \left(\frac{\Delta M_i}{1.2}\right)^2 + \left(\frac{\Delta z}{0.04}\right)^2 = 1, \tag{4.1}$$

where Δcolour, ΔM_i and Δz refer to the difference between the $(g - i)$ colour, absolute magnitude, and redshift of the SLSN host galaxy and the photometric galaxy. The scaling factor in the denominator of each term in Equation 4.1 comes from taking the range of each property and multiplying by a factor of 0.1. This factor was chosen by visual inspection to ensure an adequate chance of finding an appropriate match, while reducing mismatches in parameter space. Applying this factor ensures each property has the same weight in parameter space. We attempt a random search for a unique SDSS galaxy that satisfies Equation 4.1 on a SLSN host galaxy; this search gets repeated until a match is found, to a maximum of 1000 times. This process is repeated on SLSN host galaxies 10000 times. This results in a matched sample (SDSS-m) of 662 galaxies. Note that varying the multiplicative factor in Equation 4.1, and the number of repetitions performed on each galaxy, has no quantitative effect on the results discussed in Section 4.3.1. For this matching procedure, we only use the 18 SLSN sources with detected hosts and reliable host photometry. The rest of the analysis depends on the positions and redshifts of each SLSN source directly, and so the entire sample of 33 SLSNe is used.

The details of each sample are listed in Table 4.1. Histograms of the distributions of the colour, absolute magnitude, and redshift of SLSN-g and SDSS-m are plotted in Figure 4.2. Kolmogorov-Smirnov tests validate that the distributions match well, with the added benefit of over an order of magnitude more galaxies in the matched sample than SLSN host galaxies.

4.3 Results and discussion

4.3.1 Observations

Using bright, well-observed galaxies as a proxy for density, we count the number of bright ($M_i < -21.5$) Spec-z galaxies that are at an on-sky projection of 2 Mpc or less of the target galaxy, within $\Delta z = 0.005$, based off a typical velocity dispersion of a galaxy group/cluser (Yang et al., 2007). We denote this quantity as N_2. We use $M_i < -21.5$ as the threshold for bright galaxies as this magnitude is the completion limit for the entire spectroscopic sample for this redshift range, and we use 2 Mpc as it is the upper end of galaxy group diameters (Yang et al., 2007). Note that varying the M_i threshold does not have a qualitative effect on the results. We calculate N_2 for SLSN-g, SDSS-m, and SN-Ia as a control. SN-Ia works as a control sample because these galaxies are much less confined to a specific region of parameter-space compared to SLSNe, and the photometry is easily comparable to SLSN-g since both samples come from ZTF. A 2-d histogram showing these results is shown in Figure 4.3, with N_2 shown as a function of absolute magnitude. Note the log scale in the z-axis. This quantity is also plotted for SLSN-g and SDSS-m in dark purple and light purple, respectively. We can see that while the distribution N_2 for SN-Ia occupies a large and varied region of parameter-space (note 70 per cent of SN-Ia still has $N_2 = 0$), $N_2 \leq 2$ for SLSN-g and $N_2 \leq 3$ for SDSS-m, with the majority of galaxies having $N_2 = 0$. This is not simply a consequence of reduced numbers of SLSN-g compared to SN-Ia; binned by magnitude, the fraction of SLSN-g with any bright neighbour (i.e. $N_2 \geq 1$) reaches a maximum of about 10 per cent[4], which is only half of the minimum of the fraction of SN-Ia with any neighbour in the same bins. Similarly, SDSS-m only reaches a maximum of about 10 per cent.

We consider galaxies with $N_2 \geq 2$ as being in a high-density environment, with everything else being in a low-density environment. This number is chosen under the assumption that a typical

[4]This number is entirely dependent on the choice of binning since $N_2 \approx 1$ for SLSN-g in any magnitude bin

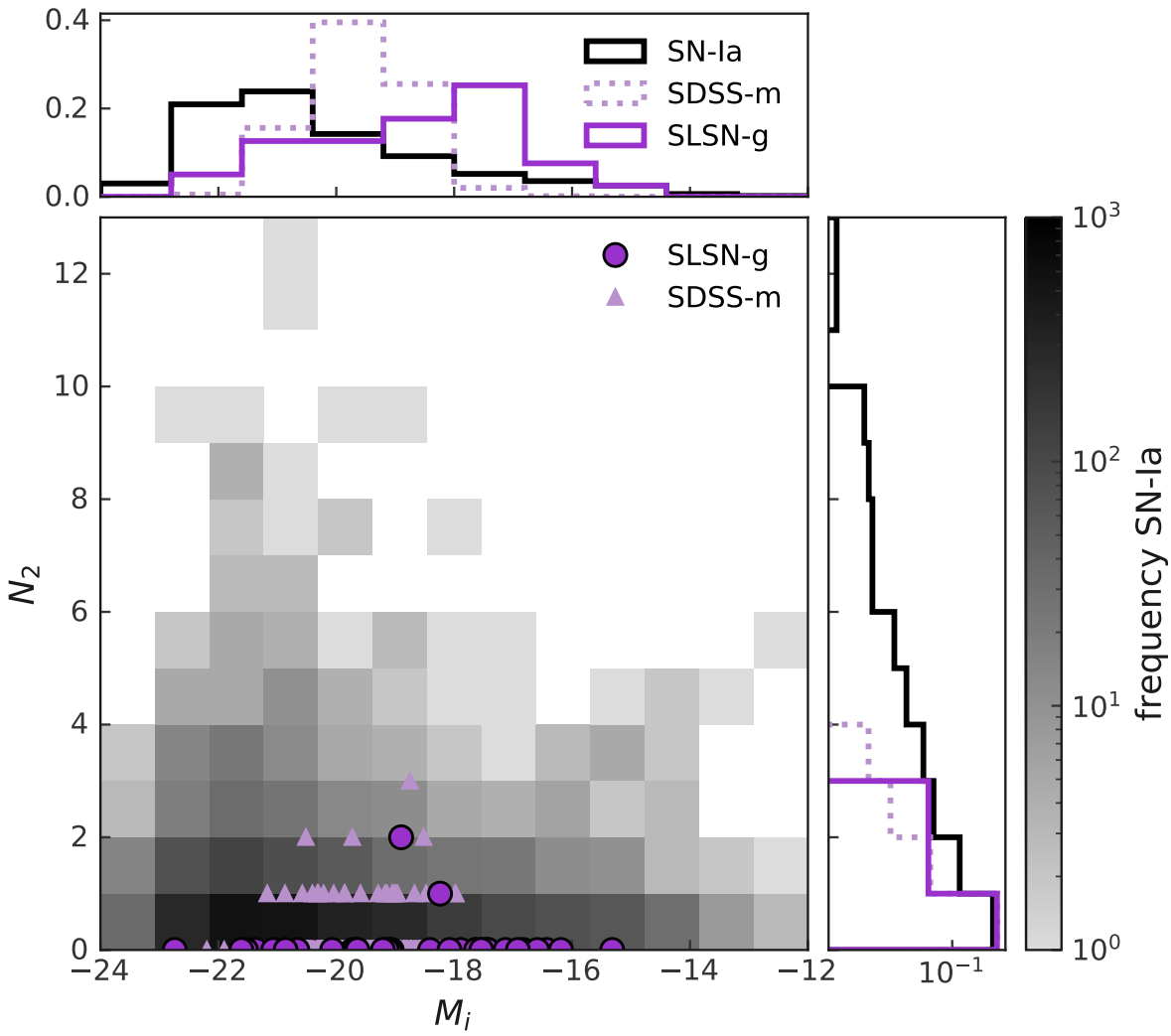


Figure 4.3: A scatter plot of the number of bright Spec-z galaxies within 2 Mpc of a target galaxy against absolute magnitude, compared to a 2d histogram of the same distribution for Type Ia SNe host galaxies. SLSN-g is shown as dark purple circles and the matched sample, SDSS-m, is shown as light purple triangles. Normalised histograms are included on the $x-$ and $y-$axes and show the absolute magnitude and N_2 distributions for SN-Ia, SDSS-m and SDSS-g.

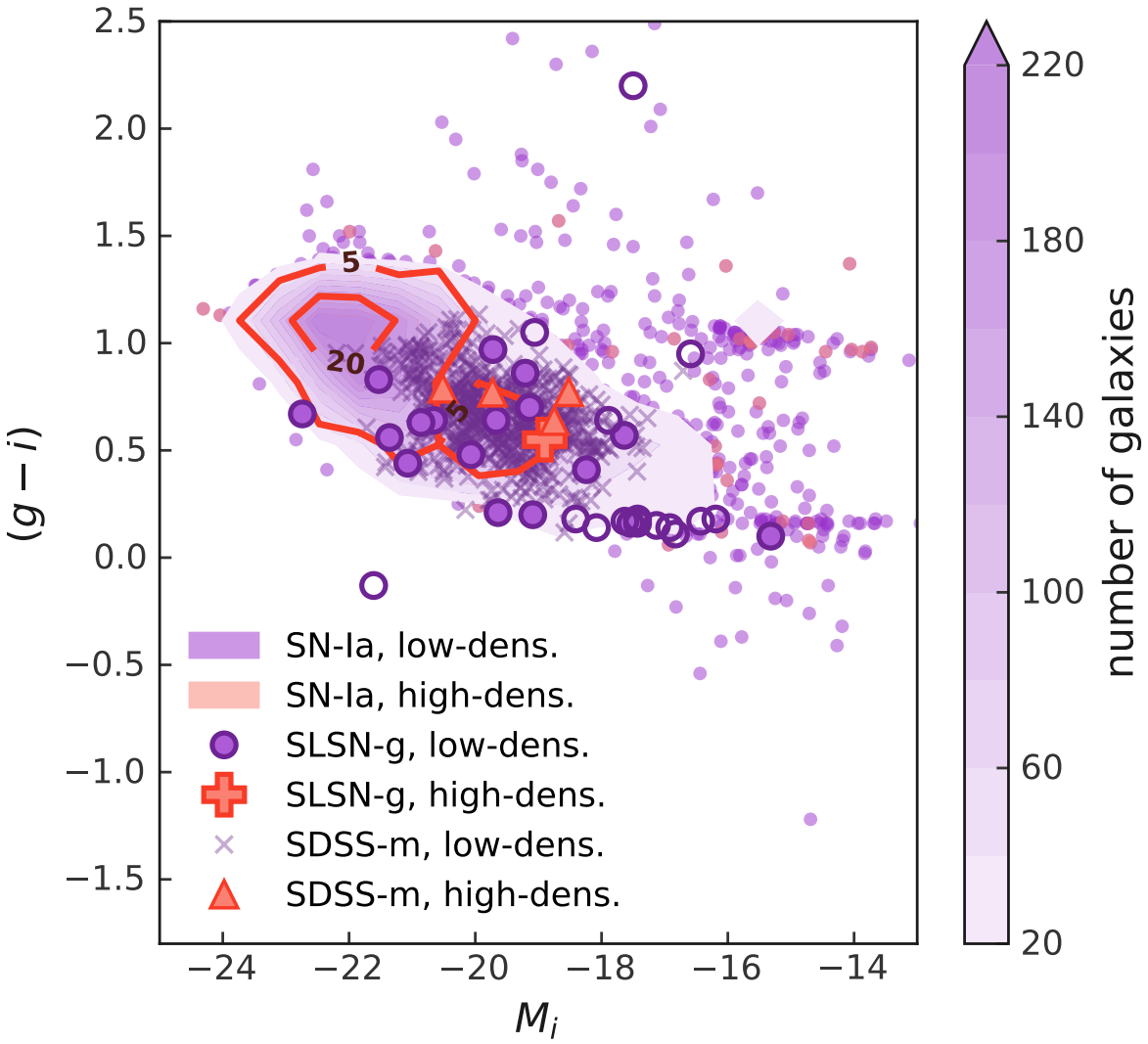


Figure 4.4: A colour-magnitude diagram comparing SLSN-g and SDSS-m to SN-Ia. Low-density SLSN-g galaxies are plotted in purple circles, high-density SLSN-g galaxies are plotted in orange pluses, low-density SDSS-m galaxies are plotted in purple crosses, high-density SDSS-m are plotted in orange triangles, and the distributions for low- and high-density SN-Ia galaxies are plotted as purple filled in contours and orange contour lines respectively. Open purple circles represent the SLSN-g sources with unreliable host photometry. Purple and orange points shown individual SN-Ia galaxies when they are not captured by the contours.

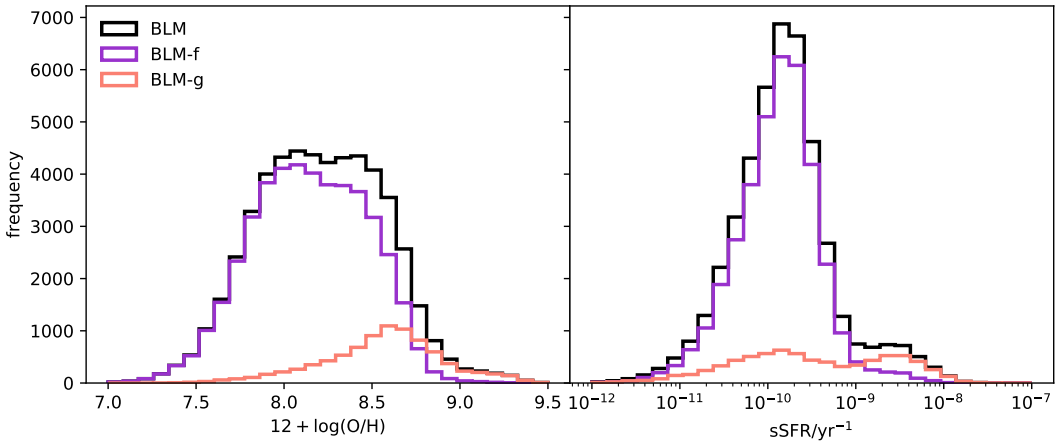


Figure 4.5: Histograms of metallicity (left) and sSFR (right) in IllustrisTNG for all blue low-mass (BLM) galaxies (black), BLM field galaxies (purple) and BLM group galaxies (orange).

galaxy group or cluster halo is of the order of a few Mpc in diameter (Yang et al., 2007), so any more than two bright (large) galaxies would be considered a high-density environment. We emphasise the fact that this is a generous constraint, set in an attempt to maximise the number of SLSN hosts in high-density environments. An example of a SN-Ia host galaxy with a high N_2 number ($N_2 = 8$) is shown in the right panel of Figure 4.1. We plot SLSN-g, SDSS-m, and SN-Ia on a colour-magnitude diagram in Figure 4.4, separated by high- and low-density. Contour lines map out the SN-Ia galaxies that are in high-density environments. We see that the high-density SLSN-g and SDSS-m galaxies are found on the outer regions of these contour lines. That is, they preferentially avoid the region in phase-space where high-density environments occur. This result, along with finding that the matched sample galaxies are also almost exclusively found in low-density environments, is indicative that the galactic properties of SLSN hosts are the constraining factor in the density of the environment of these galaxies. In other words, the type of galaxies where SLSNe are found (blue, low-mass, low-metallicity) are rarely found in high-density environments. As a fraction of each sample, SLSNe that occur in high-density environments is $1/33 = 0.03\pm^{0.06}_{0.01}$, and matched galaxies that occur in high-density environments is even lower, at $4/662 = 0.006\pm^{0.005}_{0.002}$.

4.3.2 Simulations

Since these galaxies are so faint, often the reliable host photometry or spectroscopy required to accurately measure physical properties like metallicity and star-formation rate is not available. Therefore it can be useful to use simulations to distinguish between real physical properties, and observational constraints. In Section 4.3.3 we utilize the IllustrisTNG suite of simulations[5] (Pillepich et al., 2018; Springel et al., 2018; Nelson et al., 2018; Naiman et al., 2018; Marinacci et al., 2018; Nelson et al., 2019). IllustrisTNG is a set of large-scale cosmological, gravo-magnetohydrodynamical simulations based on the Arepo code (Springel, 2010). We use the TNG-100 simulation, which has a volume of 106.5^3 cMpc. This simulation provides the best balance of large haloes (i.e. $M_h > 10^{12}$ M$_\odot$) and smaller resolution subhaloes (i.e. $M_h < 10^9$ M$_\odot$), although qualitatively similar results were found with the use of TNG-300. From this simulation, we use stellar masses, star-formation rates, gas-phase metallicity abundances, galaxy colours, group halo masses, and information about group membership.

4.3.3 IllustrisTNG

To investigate the tendency of SLSN host-like galaxies to avoid high-density environments further, we make use of the IllustrisTNG suite of simulations. From the TNG100-1 simulation, we obtain stellar masses, gas metallicities, star-formation rates, and g and i photometry on all 4.4 million subhaloes in the most recent redshift snapshot. Each subhalo resides in a parent halo with a total halo mass M_{200}, defined as the total mass of a sphere whose mean density is 200 times the critical density of the Universe. In line with the properties of SLSN host galaxies, we define a sample of blue, low-mass galaxies (BLM), with $(g-i) < 1$ and $10^7 < M_*/\mathrm{M}_\odot < 10^9$. This stellar mass range has an upper limit in line with observations of SLSN host galaxies (e.g. Schulze et al., 2018), and a lower limit to avoid contamination from haloes not yet formed into galaxies. Note that at this

[5]https://www.tng-project.org/data/

stellar mass range, virtually all galaxies ($\sim$ 98 per cent) have $(g-i) < 1$ and also are star-forming. For each subhalo, we retrieve the number of subhaloes ($N_{\rm subs}$) in its parent halo. For a galaxy to be in a group, we require $N_{\rm subs} > 1$ and $M_{200} > 10^{12}$ M$_\odot$. This is to ensure we avoid including field galaxies with smaller (non-galaxy) haloes associated with them. Everything else is assigned as being in the field.

In Figure 4.5, we plot a histogram of the log of the metallicity of BLM and a histogram of the log of sSFR, separated by group membership. Immediately it is clear that this sample is biased towards low metallicities, as is expected from observations of SLSN host galaxies (see Figure 11 in Chen et al. (2015), and Figure 8 in Perley et al. (2016a)). Notably there are much fewer BLM galaxies in groups than in the field, with group galaxies making up 35.5 per cent of the BLM sample. Additionally, the BLM galaxies that reside in groups lie at the high end of the metallicity distribution. We also see that BLM galaxies typically have intermediate sSFR, as is seen in the properties of SLSN host galaxies. However, BLM galaxies in groups dominate over field galaxies at high-sSFR.

Thus, in agreement with our observational results in the previous section, the simulation results qualitatively suggest that the reason SLSN-g are not found in dense environments is because the galaxies that host SLSN, blue low-mass, are not often found in groups. However, quantitatively, there is a potential discrepancy. From the simulation results in Figure 4.5 we measure that 35.5 per cent of such BLM galaxies are found in groups within the simulation. This means, observationally, we would expect about 12(235) of SLSN-g(SDSS-m) to be in high-density environments, compared to the 1(4) in SLSN-g(SDSS-m).

This potential discrepancy is pointing to an additional requirement in our simulated sample to properly recover the observed environmental distribution – that of low-metallicity. It is known that SLSNe require host galaxies with low metallicities (e.g. Lunnan et al., 2014), and in the simulation results of Figure 4.5, the lower metallicity ranges are dominated by field galaxies. We

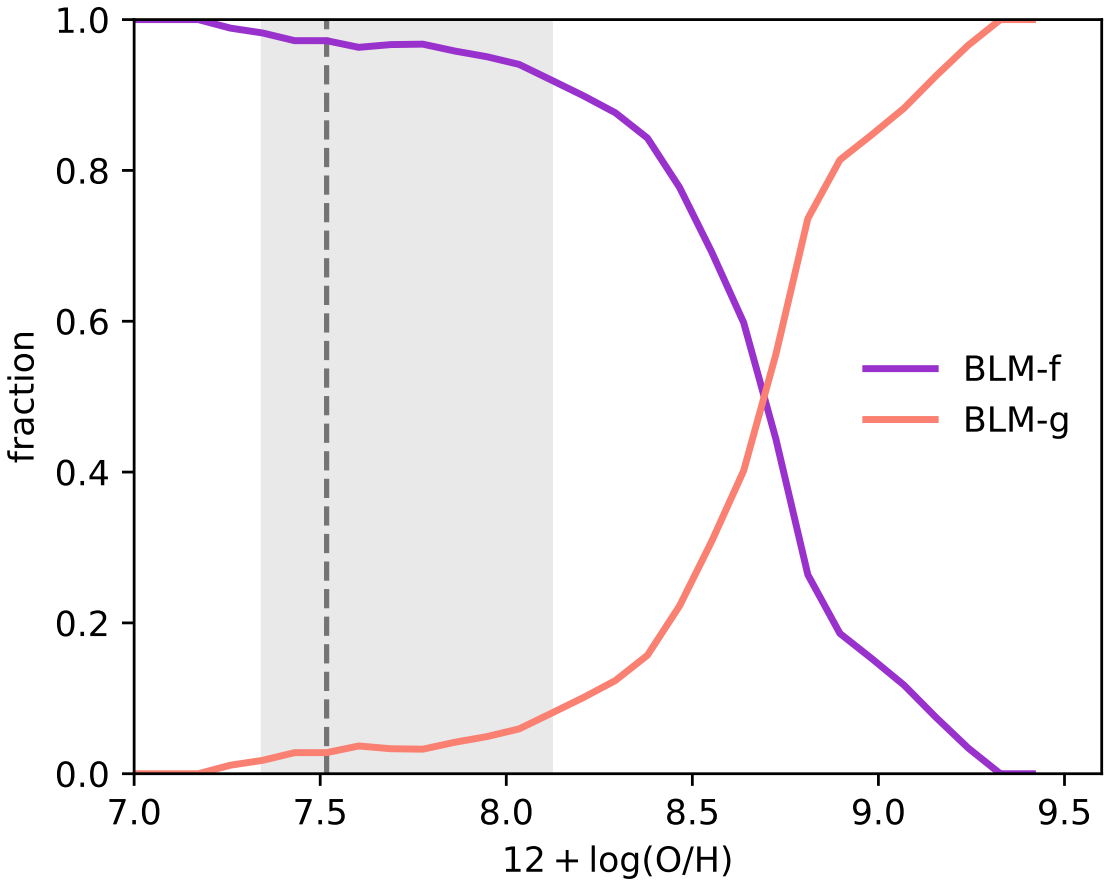


Figure 4.6: Fractions of BLM-f (purple) and BLM-g (orange) of the total BLM sample with respect to metallicity. The gray dashed line shows the metallicity at which group galaxies account for 3 per cent of the entire BLM sample, in accordance with observations, with upper and lower limits shaded in gray.

better illustrate this in Figure 4.6, where we plot the fractions of field galaxies and group galaxies with respect to the total BLM sample as a function of metallicity. Field galaxies clearly dominate at $Z < Z_{\odot}$, and group galaxies dominate at $Z > Z_{\odot}$; here we assume $Z_{\odot} = 8.69$ following Asplund et al. (2009). We also plot the metallicity at which the fraction of observed SLSN host galaxies in groups is 0.03. We can then apply generous constraints by considering the uncertainties on the SLSN occurrence rate above. By computing beta distribution confidence intervals at $c = 0.68$ (Cameron, 2011) on the fraction of observed SLSNe in groups we find this fraction to be $0.03^{+0.09}_{-0.02}$. In Figure 4.6 these confidence intervals are shaded in gray. Even with such a wide confidence interval, the highest metallicity that is consistent with the observed environmental density of SLSN hosts, and therefore the apparent upper limit of SLSN production is $12 + \log(\mathrm{O/H}) = 8.12$. This is approximately 0.2 dex lower than the apprent threshold reported in Schulze et al. (2018), $12 + \log(\mathrm{O/H}) \sim 8.3$, and 0.3 dex lower than the threshold reported in Chen et al. (2017c), $12 + \log(\mathrm{O/H}) \sim 8.4$.

In addition, we find that only about 26 per cent of BLM galaxies in groups reside in haloes of $M_h \geq 10^{13}$ $\mathrm{M}_{\odot}$. This supports the idea that the typical galaxies that host SLSNe will rarely be found in large groups or clusters.

The distributions in Figure 4.5 provide evidence that low-metallicity is the constraining requirement for SLSN production, rather than high-SFR. Focusing on the right panel, we see that the distribution of BLM-g in sSFR is more evenly distributed compared to metallicity in the left panel. In particular, noting SLSN host galaxies require $\mathrm{sSFR} \gtrsim 10^{-9}$ yr^{-1} (Schulze et al., 2018), there is actually an excess of BLM-g galaxies at this sSFR. This means that if a high-sSFR was the predominant factor for SLSN production compared to low-metallicity, we would see many more SLSN host galaxies in denser environments: ≈ 24 out of the 33 SLSN events in this sample. Since this is not the case, our analysis suggests that low-metallicity is likely the more important requirement.

4.4 Conclusions

Using SLSN sources from the ZTF BTS, we calculate whether their host galaxies are found in high-density or low-density large-scale environments. We use bright, spectroscopically redshifted galaxies with absolute magnitude $M_i < -21.5$ as tracers of density, and classify a source as in a high-density environment if there are 2 or more bright galaxies within 2 Mpc. We test our findings by comparing the SLSN sample with a sample of Type Ia supernovae, whose host galaxies span a wider range of galaxy colour and absolute magnitude. We also create another sample, derived from SDSS photometrically-redshifted galaxies, matched to the SLSN host galaxies in galaxy colour, absolute magnitude, and redshift. Our main findings may be summarised as follows:

- SLSN host galaxies are almost always located in low-density environments, with all but 2 (of 33) host galaxies having no bright galaxies within 2 Mpc. The photometrically selected matched sample (in luminosity, colour, and redshift) shows similar results. This is in contrast to Type Ia supernova host galaxies, 8.5 per cent of which have 2 or more bright neighbours This is consistent with the fraction of SNe Ia found in clusters compared to field galaxies, according to Larison et al. (2023). In any relevant magnitude bin, the maximum high-density fraction is < 10 per cent for the SLSN and matched samples, while for the SN-Ia sample the minimum is > 20 per cent.

- In analysis of the Illustris-TNG simulations, over 70 per cent of blue, low-mass galaxies are found in the field, rather than in groups. These galaxies have low metallicities and high star-formation rates, which are typical of SLSN host galaxies.

- Crucially, we find that in order to quantitatively match the rate of SLSN host galaxies found in dense environments, an additional condition on the metallicity of the host in the simulation is required. Taking the uncertainties into account, SLSN production is only favoured in galaxies with $12 + \log(\mathrm{O/H}) = 8.12$. In contrast, selecting only high-sSFR galaxies would

lead to an over-representation of high-density hosts in the simulation.

The fact that simulations suggest that galaxies capable of producing SLSNe and having high-sSFR would preferentially be found in groups, but such galaxies with low-metallicity would preferentially be found in the field, suggests that the metallicity of a galaxy is the more important factor in the occurrence of these explosive transients. However, this result will be strengthened with more observations of SLSNe and their host galaxies, which will be achieved over the coming years when new high-cadence surveys come online such as LSST at the Vera Rubin Observatory.

Appendix

4.A List of SLSNe

Table 4.2 lists all 55 SLSNe events that were available on the BTS when analysis began, the groups that classified them as SLSNe, and the relevant citation.

Table 4.2: Table of ZTF IDs of the transient events that were obtained on the BTS, the group that classified them as SLSNe, and the relevant citation.

ZTFID	Classifying group	Citation
ZTF18aavrmcg	NUTS	Dong (2018)
ZTF18aapgrxo	ZTF	Fremling and Sharma (2018)
ZTF18abmasep	ZTF	Fremling et al. (2018a)
ZTF18ablwafp	ePESSTO	Gromadzki et al. (2018)
ZTF18abshezu	ZTF	Fremling et al. (2018b)
ZTF18abvgjyl	ZTF	Fremling et al. (2018c)
ZTF18acapyww	ZTF	Fremling et al. (2018d)
ZTF18acenqto	ZTF	Fremling et al. (2018e)
ZTF18achdidy	ZTF	Fremling et al. (2019b)

Continued on next page

Table 4.2 – continued from previous page

ZTFID	Classifying group	Citation
ZTF18acxgqxq	ZTF	Fremling et al. (2019b)
ZTF18acyxnyw	ZTF	Fremling et al. (2019c)
ZTF19aaknqmp	ZTF	Fremling et al. (2019d)
ZTF19aanesgt	ZTF	Fremling et al. (2019e)
ZTF19aacxrab	ZTF	Fremling et al. (2019f)
ZTF19aavouyw	None	Chen (2019)
ZTF19aarphwc	ZTF	Fremling et al. (2019g)
ZTF19aawfbtg	TCD	Prentice et al. (2019a)
ZTF19abpbopt	ZTF	Perley (2019)
ZTF19abnacvf	ZTF	Perley et al. (2019)
ZTF19abfvnns	ZTF	Fremling and Dahiwale (2019)
ZTF18aajqcue	ZTF	Fremling et al. (2019h)
ZTF19abxgmzr	ZTF	Fremling et al. (2019a)
ZTF19acfwynw	C-SNAILS	Nicholl et al. (2019)
ZTF19acgjpgh	TCD	Prentice et al. (2019b)
ZTF20aahbfmf	SGLF	Poidevin et al. (2020)
ZTF20aaifybu	ZTF	Yan et al. (2020b)
ZTF19acbonaa	ZTF	Yan et al. (2020a)
ZTF20aayprqz	ZTF	Perley et al. (2020b)
ZTF20aattyuz	ZTF	Dahiwale and Fremling (2020)
ZTF20abobpcb	SGLF	Perez-Fournon et al. (2020)
ZTF20abpuwxl	None	Terreran (2020)
ZTF20abzumlr	ZTF	Perley et al. (2020a)
ZTF20acphdcg	ePESSTO+	Ihanec et al. (2020)

Continued on next page

Table 4.2 – continued from previous page

ZTFID	Classifying group	Citation
ZTF20acpyldh	FLEET	Blanchard et al. (2020)
ZTF21aaarmti	ePESSTO+	Gillanders et al. (2021)
ZTF21aagpymw	ePESSTO+	Magee et al. (2021)
ZTF19ackjrru	FLEET	Gomez et al. (2021a)
ZTF19acyjzbe	FLEET	Gomez et al. (2021a)
ZTF19adaivcf	FLEET	Gomez et al. (2021a)
ZTF21aappdnv	Global SN Project	Gonzalez et al. (2021)
ZTF21aakjkec	ZTF	Dahiwale and Fremling (2021)
ZTF21aaxwpyv	TCD	Deckers et al. (2021)
ZTF21aavdqgf	None	Yao et al. (2021)
ZTF21abaiono	ZTF	Perley et al. (2021)
ZTF21abcpsjy	REFITT	Weil et al. (2021)
ZTF21abbqeea	SGLF	Poidevin et al. (2021)
ZTF21absyjff	FLEET	Gomez et al. (2021b)
ZTF21accwovq	ePESSTO+	Gromadzki et al. (2021)
ZTF21abrqria	FLEET	Gomez et al. (2021c)
ZTF21aalkhot	ePESSTO+	Smith et al. (2022)
ZTF22aabimec	ePESSTO+	Srivastav et al. (2022)
ZTF22aadqgoa	SGLF	Poidevin et al. (2022)
ZTF22aalzjdc	UCSC	Davis et al. (2022)
ZTF22aarqrxf	ePESSTO+	Ayala et al. (2022)
ZTF22abcvfgs	ePESSTO+	Harvey et al. (2022)

Chapter Five

Conclusions

This thesis has illustrated the complicated web connecting various processes of galaxy evolution, from very local scales such as the effect of the central black hole on the surrounding galaxy, to global scales such as the intergalactic medium and other galaxies in the environment. Yet, we see connections between these very distinct mechanisms, in that each galaxy population discussed in this thesis can be thought of as being in a transitionary state, or in the 'green valley'.

Chapter 1 gave some context for this work, and briefly described some of the most pertinent facets of the workings of galaxies, including how gas relates to star-formation, how star-formation is quenched, and how some of the most explosive events within galaxies occur and their properties.

I presented work on the environmental dependence of galaxy quenching in Chapter 2. Most similar studies look only at whether or not a galaxy is quenched, i.e., meaning it has ceased star-formation. However, in this work I probed the most recent star formation history of galaxies, and identified galaxies which had ceased star-formation in the last $10 - 100$ Myr. This is a very small window in the lifetime of a galaxy and gives a good indication of the environmental conditions that are most linked to the initiation of quenching.

To achieve this, a combination of Hα and UV flux was exploited to trace star-formation

from different types of stars. Hα traces the biggest and brightest stars, and these are also the first to die. UV traces similar stars but with slightly longer lifetimes. Thus, when a galaxy stops producing new stars, the brightest stars will begin to die after 10 Myr, there will be little Hα, but there will still be some stars traced by UV. These galaxies were named 'recently-quenched' or RQ galaxies.

As a tracer of the environment of each galaxy, I distinguished between central and satellite galaxies in galaxy groups. I found a significant excess of RQ satellite galaxies compared to RQ central galaxies at mass $<10^{10}$ $M_{\odot}$. At larger masses, the central galaxies dominated, which was expected due to mass-quenching. Furthermore, the fraction of RQ galaxies increased with decreasing group-centric radius, indicating a radial dependence. That is, galaxies closer to the center of the group were more likely to have recently-quenched. There was also a halo-mass dependence, with higher mass haloes having higher fractions of recently-quenched satellites.

These results taken together illustrated a picture where the environment has a significant effect on the star-formation rate. Low mass satellites in high mass haloes showed the largest fraction of RQ galaxies, and this effect was stronger closer to the center of the group.

In Chapter 3, results from a study on optical variability as a probe of galaxy evolution were presented. The aim of this work was to quantify the effect of (potentially obscured) AGN variability on the star-formation rate of the galaxy. I defined a measure of the variability using the reduced χ^2 of the lightcurve of the galaxy. I classified each galaxy using a BPT diagram as either star-forming, AGN, or composite. Upon investigating how variability behaved compared to these classes and other galaxy properties, I surprisingly found that the star-forming galaxies had the highest measures of variability.

As a function of mass, the star-forming galaxies exhibited an excess of variability compared to their AGN counterparts, at least at $M_* < 10^{10.5}$ $M_{\odot}$. This also corresponded to an increase in mean variability at intermediate sSFR. At higher masses and lower sSFR, i.e. where AGN dominate, the mean variability decreased. These results were consistent with a scenario where the

effect of the AGN on the galaxy depends on the gas content, i.e. the star-formation rate, and also depends on how and when that gas gets consumed, i.e. when the galaxy becomes quenched and gas-poor. This study provided an effective way of identifying young AGN and found interesting links between the AGN variability and the evolution of the galaxy.

Finally, Chapter 4 described results from a study on the host galaxy environments of superluminous supernovae. I first established that SLSNe were almost exclusively found in low-density environments, which was perhaps not surprising considering the blue colours of SLSN hosts, but in slight contention with results from other studies that suggest SLSN hosts are sometimes found to be interacting with nearby companions.

Building on this result, I then compared to a simulated sample of galaxies with properties similar to those of SLSN hosts. I showed that, in order to match the observed rates of SLSNe in low-density environments, a low metallicity range is required. Contrastingly, the majority of galaxies at the high sSFR range were located in high-density environments, which does not match observations. These results provided evidence which suggested that the metallicity constraint in SLSN production is more crucial, compared to high star-formation rate.

To capture the complexities of galaxy evolution in one text is an ambitious task. There remain many gaps in our understanding of this subject. Fortunately, we find ourselves at the dawn of a new era in the field, with a number of exciting and promising new telescopes coming online in the next few years. Over the next decade, surveys such as the LSST at Rubin Observatory, and telescopes such as JWST and Euclid, will revolutionise our knowledge of galaxy evolution.

References

Abadi, Mario G., Ben Moore, and Richard G. Bower (Oct. 1999). "Ram pressure stripping of spiral galaxies in clusters". In: MNRAS 308.4, pp. 947–954. DOI: 10.1046/j.1365-8711.1999.02715.x. arXiv: astro-ph/9903436 [astro-ph].

Abazajian, Kevork N. et al. (June 2009). "The Seventh Data Release of the Sloan Digital Sky Survey". In: ApJS 182.2, pp. 543–558. DOI: 10.1088/0067-0049/182/2/543. arXiv: 0812.0649 [astro-ph].

Abdurro'uf et al. (Apr. 2022). "The Seventeenth Data Release of the Sloan Digital Sky Surveys: Complete Release of MaNGA, MaStar, and APOGEE-2 Data". In: ApJS 259.2, 35, p. 35. DOI: 10.3847/1538-4365/ac4414. arXiv: 2112.02026 [astro-ph.GA].

Agostino, Christopher J. et al. (Dec. 2021). "Physical Drivers of Emission-line Diversity of SDSS Seyfert 2s and LINERs after Removal of Contributions from Star Formation". In: ApJ 922.2, 156, p. 156. DOI: 10.3847/1538-4357/ac1e8d. arXiv: 2108.07812 [astro-ph.GA].

Aguerri, J. A. L., M. Balcells, and R. F. Peletier (Feb. 2001). "Growth of galactic bulges by mergers. I. Dense satellites". In: A&A 367, pp. 428–442. DOI: 10.1051/0004-6361:20000441. arXiv: astro-ph/0012156 [astro-ph].

Angus, C. R. et al. (May 2016). "A Hubble Space Telescope survey of the host galaxies of Superluminous Supernovae". In: MNRAS 458.1, pp. 84–104. DOI: 10.1093/mnras/stw063. arXiv: 1601.01874 [astro-ph.GA].

Angus, C. R. et al. (Aug. 2019). "Superluminous supernovae from the Dark Energy Survey". In: MNRAS 487.2, pp. 2215–2241. DOI: 10.1093/mnras/stz1321. arXiv: 1812.04071 [astro-ph.HE].

Arnouts, S. et al. (Oct. 2013). "Encoding of the infrared excess in the NUVrK color diagram for star-forming galaxies". In: A&A 558, A67, A67. DOI: 10.1051/0004-6361/201321768. arXiv: 1309.0008 [astro-ph.CO].

Asplund, Martin et al. (Sept. 2009). "The Chemical Composition of the Sun". In: ARA&A 47.1, pp. 481–522. DOI: 10.1146/annurev.astro.46.060407.145222. arXiv: 0909.0948 [astro-ph.SR].

Athanassoula, E. (Nov. 1992). "Morphology of bar orbits." In: MNRAS 259, pp. 328–344. DOI: 10.1093/mnras/259.2.328.

Athanassoula, E., Rubens E. G. Machado, and S. A. Rodionov (Mar. 2013). "Bar formation and evolution in disc galaxies with gas and a triaxial halo: morphology, bar strength and halo properties". In: MNRAS 429.3, pp. 1949–1969. DOI: 10.1093/mnras/sts452. arXiv: 1211.6754 [astro-ph.CO].

Ayala, B. et al. (Aug. 2022). "ePESSTO+ Transient Classification Report for 2022-08-20". In: *Transient Name Server Classification Report* 2022-2393, p. 1.

Baldassare, Vivienne F., Marla Geha, and Jenny Greene (Dec. 2018). "Identifying AGNs in Low-mass Galaxies via Long-term Optical Variability". In: ApJ 868.2, 152, p. 152. DOI: 10.3847/1538-4357/aae6cf. arXiv: 1808.09578 [astro-ph.GA].

— (June 2020). "A Search for Optical AGN Variability in 35,000 Low-mass Galaxies with the Palomar Transient Factory". In: ApJ 896.1, 10, p. 10. DOI: 10.3847/1538-4357/ab8936. arXiv: 1910.06342 [astro-ph.HE].

Baldry, I. K. et al. (Dec. 2006). "Galaxy bimodality versus stellar mass and environment". In: MNRAS 373.2, pp. 469–483. DOI: 10.1111/j.1365-2966.2006.11081.x. arXiv: astro-ph/0607648 [astro-ph].

Baldry, Ivan K. et al. (Jan. 2004). "Quantifying the Bimodal Color-Magnitude Distribution of Galaxies". In: ApJ 600.2, pp. 681–694. DOI: 10.1086/380092. arXiv: astro-ph/0309710 [astro-ph].

Baldwin, J. A., M. M. Phillips, and R. Terlevich (Feb. 1981). "Classification parameters for the emission-line spectra of extragalactic objects." In: PASP 93, pp. 5–19. DOI: 10.1086/130766.

Balogh, Michael L., Julio F. Navarro, and Simon L. Morris (Sept. 2000). "The Origin of Star Formation Gradients in Rich Galaxy Clusters". In: ApJ 540.1, pp. 113–121. DOI: 10.1086/309323. arXiv: astro-ph/0004078 [astro-ph].

Balogh, Michael L. et al. (Dec. 1999). "Differential Galaxy Evolution in Cluster and Field Galaxies at z$\sim$0.3". In: ApJ 527.1, pp. 54–79. DOI: 10.1086/308056. arXiv: astro-ph/9906470 [astro-ph].

Balogh, Michael L. et al. (Nov. 2004). "The Bimodal Galaxy Color Distribution: Dependence on Luminosity and Environment". In: ApJ 615.2, pp. L101–L104. DOI: 10.1086/426079. arXiv: astro-ph/0406266 [astro-ph].

Baum, S. A. and C. P. O'Dea (June 1991). "Multifrequency VLA observations of PKS 0745-191: the archetypal "cooling flow" radio source?" In: MNRAS 250, p. 737. DOI: 10.1093/mnras/250.4.737.

Behroozi, Peter et al. (Sept. 2019). "UNIVERSEMACHINE: The correlation between galaxy growth and dark matter halo assembly from z = 0-10". In: MNRAS 488.3, pp. 3143–3194. DOI: 10.1093/mnras/stz1182. arXiv: 1806.07893 [astro-ph.GA].

Bekki, Kenji (Feb. 2014). "Galactic star formation enhanced and quenched by ram pressure in groups and clusters". In: MNRAS 438.1, pp. 444–462. DOI: 10.1093/mnras/stt2216. arXiv: 1311.3010 [astro-ph.CO].

Bell, Eric F. et al. (Jan. 2004). "GEMS Imaging of Red-Sequence Galaxies at z$\sim$0.7: Dusty or Old?" In: ApJ 600.1, pp. L11–L14. DOI: 10.1086/381388. arXiv: astro-ph/0308272 [astro-ph].

Bellhouse, C. et al. (July 2017). "GASP. II. A MUSE View of Extreme Ram-Pressure Stripping along the Line of Sight: Kinematics of the Jellyfish Galaxy JO201". In: ApJ 844.1, 49, p. 49. DOI: 10.3847/1538-4357/aa7875. arXiv: 1704.05087 [astro-ph.GA].

Bellhouse, Callum et al. (Jan. 2021). "GASP XXIX - unwinding the arms of spiral galaxies via ram-pressure stripping". In: MNRAS 500.1, pp. 1285–1312. DOI: 10.1093/mnras/staa3298. arXiv: 2010.09733 [astro-ph.GA].

Bellm, E. (Jan. 2014). "The Zwicky Transient Facility". In: *The Third Hot-wiring the Transient Universe Workshop*. Ed. by P. R. Wozniak et al., pp. 27–33. DOI: 10.48550/arXiv.1410.8185. arXiv: 1410.8185 [astro-ph.IM].

Bellm, Eric C. et al. (Jan. 2019). "The Zwicky Transient Facility: System Overview, Performance, and First Results". In: PASP 131.995, p. 018002. DOI: 10.1088/1538-3873/aaecbe. arXiv: 1902.01932 [astro-ph.IM].

Bennett, C. L. et al. (Oct. 2013). "Nine-year Wilkinson Microwave Anisotropy Probe (WMAP) Observations: Final Maps and Results". In: ApJS 208.2, 20, p. 20. DOI: 10.1088/0067-0049/208/2/20. arXiv: 1212.5225 [astro-ph.CO].

Bialas, D. et al. (Apr. 2015). "On the occurrence of galaxy harassment". In: A&A 576, A103, A103. DOI: 10.1051/0004-6361/201425235. arXiv: 1503.01965 [astro-ph.GA].

Bianconi, M. et al. (Jan. 2018). "LoCuSS: pre-processing in galaxy groups falling into massive galaxy clusters at z = 0.2". In: MNRAS 473.1, pp. L79–L83. DOI: 10.1093/mnrasl/slx167. arXiv: 1710.04230 [astro-ph.GA].

Bigiel, F. et al. (Sept. 2010). "Tightly Correlated H I and FUV Emission in the Outskirts of M83". In: ApJ 720.1, pp. L31–L35. DOI: 10.1088/2041-8205/720/1/L31. arXiv: 1007.4550 [astro-ph.CO].

Binney, James and Scott Tremaine (2008). *Galactic Dynamics: Second Edition*.

Blanchard, P. et al. (Dec. 2020). "FLEET Transient Classification Report for 2020-12-21". In: *Transient Name Server Classification Report* 2020-3871, p. 1.

Blanchard, Peter K. et al. (Nov. 2021). "Late-time Hubble Space Telescope Observations of a Hydrogen-poor Superluminous Supernova Reveal the Power-law Decline of a Magnetar Central Engine". In: ApJ 921.1, 64, p. 64. DOI: 10.3847/1538-4357/ac1b27. arXiv: 2105.03475 [astro-ph.HE].

Bland-Hawthorn, J. et al. (Nov. 2013). "Fossil Imprint of a Powerful Flare at the Galactic Center along the Magellanic Stream". In: ApJ 778.1, 58, p. 58. DOI: 10.1088/0004-637X/778/1/58. arXiv: 1309.5455 [astro-ph.GA].

Blanton, E. L. et al. (Aug. 2011). "A Very Deep Chandra Observation of A2052: Bubbles, Shocks, and Sloshing". In: ApJ 737.2, 99, p. 99. DOI: 10.1088/0004-637X/737/2/99. arXiv: 1105.4572 [astro-ph.CO].

Blanton, Elizabeth L. et al. (Sept. 2004). "Chandra Observation of the Central Region of the Cooling Flow Cluster A262: A Radio Source That Is a Shadow of Its Former Self?" In: ApJ 612.2, pp. 817–824. DOI: 10.1086/422677. arXiv: astro-ph/0405425 [astro-ph].

Blanton, Michael R. et al. (June 2005). "New York University Value-Added Galaxy Catalog: A Galaxy Catalog Based on New Public Surveys". In: AJ 129.6, pp. 2562–2578. DOI: 10.1086/429803. arXiv: astro-ph/0410166 [astro-ph].

Blanton, Michael R. et al. (July 2017). "Sloan Digital Sky Survey IV: Mapping the Milky Way, Nearby Galaxies, and the Distant Universe". In: AJ 154.1, 28, p. 28. DOI: 10.3847/1538-3881/aa7567. arXiv: 1703.00052 [astro-ph.GA].

Bluck, Asa F. L. et al. (June 2014). "Bulge mass is king: the dominant role of the bulge in determining the fraction of passive galaxies in the Sloan Digital Sky Survey". In: MNRAS 441.1, pp. 599–629. DOI: 10.1093/mnras/stu594. arXiv: 1403.5269 [astro-ph.GA].

Boehringer, H. et al. (Oct. 1993). "A ROSAT HRI study of the interaction of the X-ray emitting gas and radio lobes of NGC 1275." In: MNRAS 264, pp. L25–L28. DOI: 10.1093/mnras/264.1.L25.

Boissier, S. et al. (Dec. 2003). "The star formation rate in disc galaxies: thresholds and dependence on gas amount". In: MNRAS 346.4, pp. 1215–1230. DOI: 10.1111/j.1365-2966.2003.07170.x. arXiv: astro-ph/0309372 [astro-ph].

Bose, Subhash et al. (Jan. 2018). "Gaia17biu/SN 2017egm in NGC 3191: The Closest Hydrogen-poor Superluminous Supernova to Date Is in a "Normal," Massive, Metal-rich Spiral Galaxy". In: ApJ 853.1, 57, p. 57. DOI: 10.3847/1538-4357/aaa298. arXiv: 1708.00864 [astro-ph.HE].

Boselli, Alessandro and Giuseppe Gavazzi (Apr. 2006). "Environmental Effects on Late-Type Galaxies in Nearby Clusters". In: PASP 118.842, pp. 517–559. DOI: 10.1086/500691. arXiv: astro-ph/0601108 [astro-ph].

Bower, R. G. et al. (Aug. 2006). "Breaking the hierarchy of galaxy formation". In: MNRAS 370.2, pp. 645–655. DOI: 10.1111/j.1365-2966.2006.10519.x. arXiv: astro-ph/0511338 [astro-ph].

Brinchmann, J. et al. (July 2004). "The physical properties of star-forming galaxies in the low-redshift Universe". In: MNRAS 351.4, pp. 1151–1179. DOI: 10.1111/j.1365-2966.2004.07881.x. arXiv: astro-ph/0311060 [astro-ph].

Burke, Colin J. et al. (May 2020). "The Curious Case of PHL 293B: A Long-lived Transient in a Metal-poor Blue Compact Dwarf Galaxy". In: ApJ 894.1, L5, p. L5. DOI: 10.3847/2041-8213/ab88de. arXiv: 2002.12369 [astro-ph.GA].

Burke, Colin J. et al. (Aug. 2021). "A characteristic optical variability time scale in astrophysical accretion disks". In: *Science* 373.6556, pp. 789–792. DOI: 10.1126/science.abg9933. arXiv: 2108.05389 [astro-ph.GA].

Burke, Colin J. et al. (Oct. 2022). "Dwarf AGNs from Optical Variability for the Origins of Seeds (DAVOS): insights from the dark energy survey deep fields". In: MNRAS 516.2, pp. 2736–2756. DOI: 10.1093/mnras/stac2262. arXiv: 2111.03079 [astro-ph.GA].

Butcher, H. and Jr. Oemler A. (Jan. 1978). "The evolution of galaxies in clusters. I. ISIT photometry of Cl 0024+1654 and 3C 295." In: ApJ 219, pp. 18–30. DOI: 10.1086/155751.

Cameron, Ewan (June 2011). "On the Estimation of Confidence Intervals for Binomial Population Proportions in Astronomy: The Simplicity and Superiority of the Bayesian Approach". In: PASA 28.2, pp. 128–139. DOI: 10.1071/AS10046. arXiv: 1012.0566 [astro-ph.IM].

Cann, Jenna M. et al. (Jan. 2019). "The Limitations of Optical Spectroscopic Diagnostics in Identifying Active Galactic Nuclei in the Low-mass Regime". In: ApJ 870.1, L2, p. L2. DOI: 10.3847/2041-8213/aaf88d. arXiv: 1812.06170 [astro-ph.GA].

Cano-Díaz, M. et al. (Jan. 2012). "Observational evidence of quasar feedback quenching star formation at high redshift". In: A&A 537, L8, p. L8. DOI: 10.1051/0004-6361/201118358. arXiv: 1112.3071 [astro-ph.CO].

Caplar, Neven, Simon J. Lilly, and Benny Trakhtenbrot (Jan. 2017). "Optical Variability of AGNs in the PTF/iPTF Survey". In: ApJ 834.2, 111, p. 111. DOI: 10.3847/1538-4357/834/2/111. arXiv: 1611.03082 [astro-ph.GA].

Cartier, Régis et al. (Sept. 2015). "The QUEST-La Silla AGN Variability Survey". In: ApJ 810.2, 164, p. 164. DOI: 10.1088/0004-637X/810/2/164. arXiv: 1507.08676 [astro-ph.GA].

Catinella, Barbara et al. (May 2018). "xGASS: total cold gas scaling relations and molecular-to-atomic gas ratios of galaxies in the local Universe". In: MNRAS 476.1, pp. 875–895. DOI: 10.1093/mnras/sty089. arXiv: 1802.02373 [astro-ph.GA].

Chambers, K. C. et al. (Dec. 2016). "The Pan-STARRS1 Surveys". In: *arXiv e-prints*, arXiv:1612.05560, arXiv:1612.05560. DOI: 10.48550/arXiv.1612.05560. arXiv: 1612.05560 [astro-ph.IM].

Chatzopoulos, E., J. Craig Wheeler, and J. Vinko (Feb. 2012). "Generalized Semi-analytical Models of Supernova Light Curves". In: ApJ 746.2, 121, p. 121. DOI: 10.1088/0004-637X/746/2/121. arXiv: 1111.5237 [astro-ph.HE].

Chauke, Priscilla et al. (May 2019). "Rejuvenation in z ∼ 0.8 Quiescent Galaxies in LEGA-C". In: ApJ 877.1, 48, p. 48. DOI: 10.3847/1538-4357/ab164d. arXiv: 1905.07541 [astro-ph.GA].

Chen, T. (June 2019). "Transient Classification Report for 2019-06-05". In: *Transient Name Server Classification Report* 2019-938, p. 1.

Chen, T. -W. et al. (Sept. 2015). "The host galaxy and late-time evolution of the superluminous supernova PTF12dam". In: MNRAS 452.2, pp. 1567–1586. DOI: 10.1093/mnras/stv1360. arXiv: 1409.7728 [astro-ph.GA].

Chen, T. -W. et al. (June 2017a). "The evolution of superluminous supernova LSQ14mo and its interacting host galaxy system". In: A&A 602, A9, A9. DOI: 10.1051/0004-6361/201630163. arXiv: 1611.09910 [astro-ph.SR].

Chen, Ting-Wan et al. (Feb. 2013). "The Host Galaxy of the Super-luminous SN 2010gx and Limits on Explosive ^{56}Ni Production". In: ApJ 763.2, L28, p. L28. DOI: 10.1088/2041-8205/763/2/L28. arXiv: 1210.4027 [astro-ph.CO].

Chen, Ting-Wan et al. (Nov. 2017b). "Spatially Resolved MaNGA Observations of the Host Galaxy of Superluminous Supernova 2017egm". In: ApJ 849.1, L4, p. L4. DOI: 10.3847/2041-8213/aa8f40. arXiv: 1708.04618 [astro-ph.GA].

Chen, Ting-Wan et al. (Sept. 2017c). "Superluminous supernova progenitors have a half-solar metallicity threshold". In: MNRAS 470.3, pp. 3566–3573. DOI: 10.1093/mnras/stx1428. arXiv: 1605.04925 [astro-ph.GA].

Chevalier, Roger A. and Christopher M. Irwin (Mar. 2011). "Shock Breakout in Dense Mass Loss: Luminous Supernovae". In: ApJ 729.1, L6, p. L6. DOI: 10.1088/2041-8205/729/1/L6. arXiv: 1101.1111 [astro-ph.HE].

Cikota, Aleksandar et al. (Aug. 2017). "Spatially resolved analysis of superluminous supernovae PTF 11hrq and PTF 12dam host galaxies". In: MNRAS 469.4, pp. 4705–4717. DOI: 10.1093/mnras/stx1110. arXiv: 1705.01948 [astro-ph.HE].

Cleland, Cressida and Sean L. McGee (Jan. 2021). "The environmental dependence of rapidly quenching and rejuvenating galaxies". In: MNRAS 500.1, pp. 590–602. DOI: 10.1093/mnras/staa3267. arXiv: 2006.16307 [astro-ph.GA].

— (Oct. 2022). "Photometric variability in star-forming galaxies as evidence for low-mass AGN and a precursor to quenching". In: MNRAS 515.4, pp. 5905–5913. DOI: 10.1093/mnras/stac2188. arXiv: 2208.00831 [astro-ph.GA].

Cleland, Cressida, Sean L. McGee, and Matt Nicholl (Sept. 2023). "Metallicity beats sSFR: the connection between superluminous supernova host galaxy environments and the importance of metallicity for their production". In: MNRAS 524.3, pp. 3559–3567. DOI: 10.1093/mnras/stad2118. arXiv: 2307.06368 [astro-ph.GA].

Comerford, Julia M. et al. (June 2015). "Merger-driven Fueling of Active Galactic Nuclei: Six Dual and Offset AGNs Discovered with Chandra and Hubble Space Telescope Observations". In: ApJ 806.2, 219, p. 219. DOI: 10.1088/0004-637X/806/2/219. arXiv: 1504.01391 [astro-ph.GA].

Cooper, Michael C., Jeffrey A. Newman, and Renbin Yan (Oct. 2009). "The Large-scale Environments of Type Ia Supernovae: Evidence for a Metallicity Bias in the Rate or Luminosity of Prompt Ia Events". In: ApJ 704.1, pp. 687–704. DOI: 10.1088/0004-637X/704/1/687. arXiv: 0901.4338 [astro-ph.SR].

Couch, Warrick J. and R. M. Sharples (Dec. 1987). "A spectroscopic study of three rich galaxy clusters at zeta=0.31." In: MNRAS 229, pp. 423–456. DOI: 10.1093/mnras/229.3.423.

Croton, Darren J. et al. (Jan. 2006). "The many lives of active galactic nuclei: cooling flows, black holes and the luminosities and colours of galaxies". In: MNRAS 365.1, pp. 11–28. DOI: 10.1111/j.1365-2966.2005.09675.x. arXiv: astro-ph/0508046 [astro-ph].

Dahiwale, A. and C. Fremling (June 2020). "ZTF Transient Classification Report for 2020-06-11". In: *Transient Name Server Classification Report* 2020-1756, p. 1.

— (Apr. 2021). "ZTF Transient Classification Report for 2021-04-16". In: *Transient Name Server Classification Report* 2021-1234, pp. 1–1234.

David, Laurence P. et al. (Feb. 2011). "Active-galactic-nucleus-driven Weather and Multiphase Gas in the Core of the NGC 5044 Galaxy Group". In: ApJ 728.2, 162, p. 162. DOI: 10.1088/0004-637X/728/2/162. arXiv: 1010.0650 [astro-ph.CO].

Davies, L. J. M. et al. (Mar. 2019). "Galaxy and Mass Assembly (GAMA): environmental quenching of centrals and satellites in groups". In: MNRAS 483.4, pp. 5444–5458. DOI: 10.1093/mnras/sty3393. arXiv: 1901.01640 [astro-ph.GA].

Davis, K. et al. (July 2022). "UCSC Transient Classification Report for 2022-07-05". In: *Transient Name Server Classification Report* 2022-1881, p. 1.

De Cia, Annalisa et al. (June 2018). "Light Curves of Hydrogen-poor Superluminous Supernovae from the Palomar Transient Factory". In: ApJ 860.2, 100, p. 100. DOI: 10.3847/1538-4357/aab9b6. arXiv: 1708.01623 [astro-ph.HE].

de Vaucouleurs, Gerard (Jan. 1948). "Recherches sur les Nebuleuses Extragalactiques". In: *Annales d'Astrophysique* 11, p. 247.

Deckers, M. et al. (Apr. 2021). "TCD Transient Classification Report for 2021-04-26". In: *Transient Name Server Classification Report* 2021-1365, pp. 1–1365.

Dessart, Luc et al. (Oct. 2012). "Superluminous supernovae: ^{56}Ni power versus magnetar radiation". In: MNRAS 426.1, pp. L76–L80. DOI: 10.1111/j.1745-3933.2012.01329.x. arXiv: 1208.1214 [astro-ph.SR].

Di Matteo, Tiziana, Volker Springel, and Lars Hernquist (Feb. 2005). "Energy input from quasars regulates the growth and activity of black holes and their host galaxies". In: Nature 433.7026, pp. 604–607. DOI: 10.1038/nature03335. arXiv: astro-ph/0502199 [astro-ph].

Doi, Mamoru et al. (Apr. 2010). "Photometric Response Functions of the Sloan Digital Sky Survey Imager". In: AJ 139.4, pp. 1628–1648. DOI: 10.1088/0004-6256/139/4/1628. arXiv: 1002.3701 [astro-ph.IM].

Dong, S. (May 2018). "NUTS Transient Classification Report for 2018-05-19". In: *Transient Name Server Classification Report* 2018-673, p. 1.

Donnari, Martina et al. (Jan. 2021). "Quenched fractions in the IllustrisTNG simulations: the roles of AGN feedback, environment, and pre-processing". In: MNRAS 500.3, pp. 4004–4024. DOI: 10.1093/mnras/staa3006. arXiv: 2008.00005 [astro-ph.GA].

Dressler, A. (Mar. 1980). "Galaxy morphology in rich clusters: implications for the formation and evolution of galaxies." In: ApJ 236, pp. 351–365. DOI: 10.1086/157753.

Dressler, A. and J. E. Gunn (July 1983). "Spectroscopy of galaxies in distant clusters. II. The population of the 3C 295 cluster." In: ApJ 270, pp. 7–19. DOI: 10.1086/161093.

Dressler, Alan et al. (Dec. 1997). "Evolution since z = 0.5 of the Morphology-Density Relation for Clusters of Galaxies". In: ApJ 490.2, pp. 577–591. DOI: 10.1086/304890. arXiv: astro-ph/9707232 [astro-ph].

Duncan, Kenneth et al. (May 2019). "Observational Constraints on the Merger History of Galaxies since z ≈ 6: Probabilistic Galaxy Pair Counts in the CANDELS Fields". In: ApJ 876.2, 110, p. 110. DOI: 10.3847/1538-4357/ab148a. arXiv: 1903.12188 [astro-ph.GA].

Ellison, Sara L. et al. (July 2009). "The mass-metallicity relation in galaxy clusters: the relative importance of cluster membership versus local environment". In: MNRAS 396.3, pp. 1257–1272. DOI: 10.1111/j.1365-2966.2009.14817.x. arXiv: 0903.4684 [astro-ph.CO].

Faber, S. M. et al. (Aug. 2007). "Galaxy Luminosity Functions to z$_\sim$1 from DEEP2 and COMBO-17: Implications for Red Galaxy Formation". In: ApJ 665.1, pp. 265–294. DOI: 10.1086/519294. arXiv: astro-ph/0506044 [astro-ph].

Fabian, A. C. (Sept. 2012). "Observational Evidence of Active Galactic Nuclei Feedback". In: ARA&A 50, pp. 455–489. DOI: 10.1146/annurev-astro-081811-125521. arXiv: 1204.4114 [astro-ph.CO].

Fabian, A. C. et al. (Sept. 2003). "A deep Chandra observation of the Perseus cluster: shocks and ripples". In: MNRAS 344.3, pp. L43–L47. DOI: 10.1046/j.1365-8711.2003.06902.x. arXiv: astro-ph/0306036 [astro-ph].

Fabian, A. C. et al. (Feb. 2006). "A very deep Chandra observation of the Perseus cluster: shocks, ripples and conduction". In: MNRAS 366.2, pp. 417–428. DOI: 10.1111/j.1365-2966.2005.09896.x. arXiv: astro-ph/0510476 [astro-ph].

Fasano, Giovanni et al. (Oct. 2000). "The Evolution of the Galactic Morphological Types in Clusters". In: ApJ 542.2, pp. 673–683. DOI: 10.1086/317047. arXiv: astro-ph/0005171 [astro-ph].

Ferrarese, Laura and David Merritt (Aug. 2000). "A Fundamental Relation between Supermassive Black Holes and Their Host Galaxies". In: ApJ 539.1, pp. L9–L12. DOI: 10.1086/312838. arXiv: astro-ph/0006053 [astro-ph].

Ferreira, Leonardo et al. (May 2022). "A Simulation-driven Deep Learning Approach for Separating Mergers and Star-forming Galaxies: The Formation Histories of Clumpy Galaxies in All of the CANDELS Fields". In: ApJ 931.1, 34, p. 34. DOI: 10.3847/1538-4357/ac66ea. arXiv: 2204.05786 [astro-ph.GA].

Fiore, A. et al. (May 2022). "Close, bright, and boxy: the superluminous SN 2018hti". In: MNRAS 512.3, pp. 4484–4502. DOI: 10.1093/mnras/stac744. arXiv: 2111.07142 [astro-ph.HE].

Flewelling, H. A. et al. (Nov. 2020). "The Pan-STARRS1 Database and Data Products". In: ApJS 251.1, 7, p. 7. DOI: 10.3847/1538-4365/abb82d. arXiv: 1612.05243 [astro-ph.IM].

Forman, W. et al. (Dec. 2005). "Reflections of Active Galactic Nucleus Outbursts in the Gaseous Atmosphere of M87". In: ApJ 635.2, pp. 894–906. DOI: 10.1086/429746. arXiv: astro-ph/0312576 [astro-ph].

Fremling, C. and A. Dahiwale (Sept. 2019). "ZTF Transient Classification Report for 2019-09-08". In: *Transient Name Server Classification Report* 2019-1774, p. 1.

Fremling, C., A. Dahiwale, and A. Dugas (Sept. 2019a). "ZTF Transient Classification Report for 2019-09-26". In: *Transient Name Server Classification Report* 2019-1923, p. 1.

Fremling, C., A. Dugas, and Y. Sharma (Aug. 2018a). "ZTF Transient Classification Report for 2018-08-22". In: *Transient Name Server Classification Report* 2018-1232, p. 1.

— (Sept. 2018b). "ZTF Transient Classification Report for 2018-09-18". In: *Transient Name Server Classification Report* 2018-1411, p. 1.

— (Sept. 2018c). "ZTF Transient Classification Report for 2018-09-19". In: *Transient Name Server Classification Report* 2018-1416, p. 1.

— (Dec. 2018d). "ZTF Transient Classification Report for 2018-12-04". In: *Transient Name Server Classification Report* 2018-1870, p. 1.

— (Dec. 2018e). "ZTF Transient Classification Report for 2018-12-05". In: *Transient Name Server Classification Report* 2018-1877, p. 1.

— (Jan. 2019b). "ZTF Transient Classification Report for 2019-01-05". In: *Transient Name Server Classification Report* 2019-32, p. 1.

Fremling, C., A. Dugas, and Y. Sharma (Feb. 2019c). "ZTF Transient Classification Report for 2019-02-01 2018kly, SN2018kly, SN 2018kly, 2019kg, SN2019kg, SN 2019kg, 2019uo, SN2019uo, SN 2019uo, 2019ui, SN2019ui, SN 2019ui, 2019us, SN2019us, SN 2019us, 2018kyt, SN2018kyt, SN 2018kyt, 2018lan, SN2018lan, SN 2018lan, 2018lfb, SN2018lfb, SN 2018lfb, 2019abv, SN2019abv, SN 2019abv, 2018lev, SN2018lev, SN 2018lev, 2019vv, SN2019vv, SN 2019vv, 2019abk, SN2019abk, SN 2019abk, 2018khn, SN2018khn, SN 2018khn, 2018ktv, SN2018ktv, SN 2018ktv, 2019bq, SN2019bq, SN 2019bq, 2019aas, SN2019aas, SN 2019aas, 2019ail, SN2019ail, SN 2019ail, 2018kkv, SN2018kkv, SN 2018kkv, 2018liq, SN2018liq, SN 2018liq". In: *Transient Name Server Classification Report* 2019-188, p. 1.

— (Apr. 2019d). "ZTF Transient Classification Report for 2019-04-18". In: *Transient Name Server Classification Report* 2019-598, p. 1.

— (Apr. 2019e). "ZTF Transient Classification Report for 2019-04-25". In: *Transient Name Server Classification Report* 2019-636, p. 1.

— (May 2019f). "ZTF Transient Classification Report for 2019-05-10". In: *Transient Name Server Classification Report* 2019-747, p. 1.

— (June 2019g). "ZTF Transient Classification Report for 2019-06-07". In: *Transient Name Server Classification Report* 2019-952, p. 1.

Fremling, C. and Y. Sharma (June 2018). "ZTF Transient Classification Report for 2018-06-13". In: *Transient Name Server Classification Report* 2018-815, p. 1.

Fremling, C., Y. Sharma, and A. Dahiwale (Sept. 2019h). "ZTF Transient Classification Report for 2019-09-16". In: *Transient Name Server Classification Report* 2019-1838, p. 1.

French, K. Decker, Iair Arcavi, and Ann Zabludoff (Feb. 2016). "Tidal Disruption Events Prefer Unusual Host Galaxies". In: ApJ 818.1, L21, p. L21. DOI: 10.3847/2041-8205/818/1/L21. arXiv: 1601.04705 [astro-ph.GA].

Frohmaier, C. et al. (Jan. 2021). "From core collapse to superluminous: the rates of massive stellar explosions from the Palomar Transient Factory". In: MNRAS 500.4, pp. 5142–5158. DOI: 10.1093/mnras/staa3607. arXiv: 2010.15270 [astro-ph.HE].

Fukugita, M. et al. (Apr. 1996). "The Sloan Digital Sky Survey Photometric System". In: AJ 111, p. 1748. DOI: 10.1086/117915.

Gabor, J. M. et al. (Sept. 2010). "How is star formation quenched in massive galaxies?" In: MNRAS 407.2, pp. 749–771. DOI: 10.1111/j.1365-2966.2010.16961.x. arXiv: 1001.1734 [astro-ph.CO].

Gal-Yam, Avishay (Aug. 2012). "Luminous Supernovae". In: *Science* 337.6097, p. 927. DOI: 10.1126/science.1203601. arXiv: 1208.3217 [astro-ph.CO].

— (Aug. 2019). "The Most Luminous Supernovae". In: ARA&A 57, pp. 305–333. DOI: 10.1146/annurev-astro-081817-051819. arXiv: 1812.01428 [astro-ph.HE].

Gebhardt, Karl et al. (Aug. 2000). "A Relationship between Nuclear Black Hole Mass and Galaxy Velocity Dispersion". In: ApJ 539.1, pp. L13–L16. DOI: 10.1086/312840. arXiv: astro-ph/0006289 [astro-ph].

Gilbank, David G. et al. (July 2010). "The local star formation rate density: assessing calibrations using [OII], H and UV luminosities". In: MNRAS 405.4, pp. 2594–2614. DOI: 10.1111/j.1365-2966.2010.16640.x. arXiv: 1002.3172 [astro-ph.CO].

Gillanders, J. et al. (Jan. 2021). "ePESSTO+ Transient Classification Report for 2021-01-08". In: *Transient Name Server Classification Report* 2021-86, pp. 1–86.

Ginzburg, Sivan and Shmuel Balberg (Oct. 2012). "Superluminous Light Curves from Supernovae Exploding in a Dense Wind". In: ApJ 757.2, 178, p. 178. DOI: 10.1088/0004-637X/757/2/178. arXiv: 1205.3455 [astro-ph.SR].

Gomez, S. et al. (Feb. 2021a). "FLEET Transient Classification Report for 2021-02-22". In: *Transient Name Server Classification Report* 2021-565, pp. 1–565.

— (Sept. 2021b). "FLEET Transient Classification Report for 2021-09-22". In: *Transient Name Server Classification Report* 2021-3270, pp. 1–3270.

Gomez, S. et al. (Oct. 2021c). "FLEET Transient Classification Report for 2021-10-27". In: *Transient Name Server Classification Report* 2021-3662, pp. 1–3662.

Gomez, Sebastian et al. (June 2021d). "The Luminous and Double-peaked Type Ic Supernova 2019stc: Evidence for Multiple Energy Sources". In: ApJ 913.2, 143, p. 143. DOI: 10.3847/1538-4357/abf5e3. arXiv: 2103.02611 [astro-ph.HE].

Gonzalez, E. P. et al. (Apr. 2021). "Global SN Project Transient Classification Report for 2021-04-15". In: *Transient Name Server Classification Report* 2021-1220, pp. 1–1220.

Goto, Tomotsugu et al. (Aug. 2003a). "The Environment of Passive Spiral Galaxies in the SDSS". In: PASJ 55.4, pp. 757–770. DOI: 10.1093/pasj/55.4.757. arXiv: astro-ph/0301303 [astro-ph].

Goto, Tomotsugu et al. (Dec. 2003b). "The morphology-density relation in the Sloan Digital Sky Survey". In: MNRAS 346.2, pp. 601–614. DOI: 10.1046/j.1365-2966.2003.07114.x. arXiv: astro-ph/0312043 [astro-ph].

Graham, J., A. C. Fabian, and J. S. Sanders (Dec. 2008). "Detecting sound-wave-like surface brightness ripples in cluster cores". In: MNRAS 391.4, pp. 1749–1757. DOI: 10.1111/j.1365-2966.2008.13861.x. arXiv: 0808.2408 [astro-ph].

Greiner, Jochen et al. (July 2015). "A very luminous magnetar-powered supernova associated with an ultra-long γ-ray burst". In: Nature 523.7559, pp. 189–192. DOI: 10.1038/nature14579. arXiv: 1509.03279 [astro-ph.HE].

Gromadzki, M., R. Cartier, and O. Yaron (Oct. 2021). "ePESSTO+ Transient Classification Report for 2021-10-26". In: *Transient Name Server Classification Report* 2021-3651, pp. 1–3651.

Gromadzki, M. et al. (Sept. 2018). "ePESSTO Transient Classification Report for 2018-09-16". In: *Transient Name Server Classification Report* 2018-1396, p. 1.

Groves, Brent A. et al. (Jan. 2015). "Dust Continuum Emission as a Tracer of Gas Mass in Galaxies". In: ApJ 799.1, 96, p. 96. DOI: 10.1088/0004-637X/799/1/96. arXiv: 1411.2975 [astro-ph.GA].

Gültekin, Kayhan et al. (June 2009). "The M-σ and M-L Relations in Galactic Bulges, and Determinations of Their Intrinsic Scatter". In: ApJ 698.1, pp. 198–221. DOI: 10.1088/0004-637X/698/1/198. arXiv: 0903.4897 [astro-ph.GA].

Gunn, J. E. et al. (Dec. 1998). "The Sloan Digital Sky Survey Photometric Camera". In: AJ 116.6, pp. 3040–3081. DOI: 10.1086/300645. arXiv: astro-ph/9809085 [astro-ph].

Gunn, James E. and III Gott J. Richard (Aug. 1972). "On the Infall of Matter Into Clusters of Galaxies and Some Effects on Their Evolution". In: ApJ 176, p. 1. DOI: 10.1086/151605.

Gunn, James E. et al. (Apr. 2006). "The 2.5 m Telescope of the Sloan Digital Sky Survey". In: AJ 131.4, pp. 2332–2359. DOI: 10.1086/500975. arXiv: astro-ph/0602326 [astro-ph].

Haines, C. P. et al. (Aug. 2006). "The Different Environmental Dependencies of Star Formation for Giant and Dwarf Galaxies". In: ApJ 647.1, pp. L21–L24. DOI: 10.1086/507297. arXiv: astro-ph/0606521 [astro-ph].

Harfst, S., Ch. Theis, and G. Hensler (Apr. 2006). "Modelling galaxies with a 3d multi-phase ISM". In: A&A 449.2, pp. 509–518. DOI: 10.1051/0004-6361:20042190. arXiv: astro-ph/0511775 [astro-ph].

Harvey, L. et al. (Oct. 2022). "ePESSTO+ Transient Classification Report for 2022-10-15". In: *Transient Name Server Classification Report* 2022-2997, p. 1.

Hawkins, M. R. S. (Feb. 2007). "Timescale of variation and the size of the accretion disc in active galactic nuclei". In: A&A 462.2, pp. 581–589. DOI: 10.1051/0004-6361:20066283. arXiv: astro-ph/0611491 [astro-ph].

Heckman, Timothy M. and Philip N. Best (Aug. 2014). "The Coevolution of Galaxies and Supermassive Black Holes: Insights from Surveys of the Contemporary Universe". In: ARA&A 52, pp. 589–660. DOI: 10.1146/annurev-astro-081913-035722. arXiv: 1403.4620 [astro-ph.GA].

Heyer, Mark H. et al. (Feb. 2004). "The Molecular Gas Distribution and Schmidt Law in M33". In: ApJ 602.2, pp. 723–729. DOI: 10.1086/381196. arXiv: astro-ph/0311226 [astro-ph].

Hickox, Ryan C. et al. (Feb. 2014). "Black Hole Variability and the Star Formation-Active Galactic Nucleus Connection: Do All Star-forming Galaxies Host an Active Galactic Nucleus?" In: ApJ 782.1, 9, p. 9. DOI: 10.1088/0004-637X/782/1/9. arXiv: 1306.3218 [astro-ph.CO].

Hopkins, Philip F. et al. (Mar. 2006). "A Unified, Merger-driven Model of the Origin of Starbursts, Quasars, the Cosmic X-Ray Background, Supermassive Black Holes, and Galaxy Spheroids". In: ApJS 163.1, pp. 1–49. DOI: 10.1086/499298. arXiv: astro-ph/0506398 [astro-ph].

Hosseinzadeh, Griffin et al. (July 2022). "Bumpy Declining Light Curves Are Common in Hydrogen-poor Superluminous Supernovae". In: ApJ 933.1, 14, p. 14. DOI: 10.3847/1538-4357/ac67dd. arXiv: 2109.09743 [astro-ph.HE].

Hu, Jian (June 2008). "The black hole mass-stellar velocity dispersion correlation: bulges versus pseudo-bulges". In: MNRAS 386.4, pp. 2242–2252. DOI: 10.1111/j.1365-2966.2008.13195.x. arXiv: 0801.1481 [astro-ph].

Humphrey, Philip J. et al. (Mar. 2011). "A Census of Baryons and Dark Matter in an Isolated, Milky Way Sized Elliptical Galaxy". In: ApJ 729.1, 53, p. 53. DOI: 10.1088/0004-637X/729/1/53. arXiv: 1010.6078 [astro-ph.CO].

Ihanec, N. et al. (Nov. 2020). "ePESSTO+ Transient Classification Report for 2020-11-17". In: *Transient Name Server Classification Report* 2020-3486, p. 1.

Inserra, C. et al. (June 2013). "Super-luminous Type Ic Supernovae: Catching a Magnetar by the Tail". In: ApJ 770.2, 128, p. 128. DOI: 10.1088/0004-637X/770/2/128. arXiv: 1304.3320 [astro-ph.HE].

Inserra, C. et al. (July 2017). "Complexity in the light curves and spectra of slow-evolving superluminous supernovae". In: MNRAS 468.4, pp. 4642–4662. DOI: 10.1093/mnras/stx834. arXiv: 1701.00941 [astro-ph.HE].

Ioka, Kunihito, Kenta Hotokezaka, and Tsvi Piran (Dec. 2016). "Are Ultra-long Gamma-Ray Bursts Caused by Blue Supergiant Collapsars, Newborn Magnetars, or White Dwarf Tidal

Disruption Events?" In: ApJ 833.1, 110, p. 110. DOI: 10.3847/1538-4357/833/1/110. arXiv: 1608.02938 [astro-ph.HE].

Jaffé, Yara L. et al. (June 2018). "GASP. IX. Jellyfish galaxies in phase-space: an orbital study of intense ram-pressure stripping in clusters". In: MNRAS 476.4, pp. 4753–4764. DOI: 10.1093/mnras/sty500. arXiv: 1802.07297 [astro-ph.GA].

Kasen, Daniel and Lars Bildsten (July 2010). "Supernova Light Curves Powered by Young Magnetars". In: ApJ 717.1, pp. 245–249. DOI: 10.1088/0004-637X/717/1/245. arXiv: 0911.0680 [astro-ph.HE].

Kauffmann, G., S. D. M. White, and B. Guiderdoni (Sept. 1993). "The formation and evolution of galaxies within merging dark matter haloes." In: MNRAS 264, pp. 201–218. DOI: 10.1093/mnras/264.1.201.

Kauffmann, Guinevere et al. (May 2003a). "Stellar masses and star formation histories for 10^5 galaxies from the Sloan Digital Sky Survey". In: MNRAS 341.1, pp. 33–53. DOI: 10.1046/j.1365-8711.2003.06291.x. arXiv: astro-ph/0204055 [astro-ph].

Kauffmann, Guinevere et al. (Dec. 2003b). "The host galaxies of active galactic nuclei". In: MNRAS 346.4, pp. 1055–1077. DOI: 10.1111/j.1365-2966.2003.07154.x. arXiv: astro-ph/0304239 [astro-ph].

Kauffmann, Guinevere et al. (Dec. 2007). "Ongoing Formation of Bulges and Black Holes in the Local Universe: New Insights from GALEX". In: ApJS 173.2, pp. 357–376. DOI: 10.1086/516647. arXiv: astro-ph/0609436 [astro-ph].

Kaviraj, S. et al. (Dec. 2007). "The UV properties of E+A galaxies: constraints on feedback-driven quenching of star formation". In: MNRAS 382.3, pp. 960–970. DOI: 10.1111/j.1365-2966.2007.12475.x. arXiv: 0707.3570 [astro-ph].

Kelly, Brandon C., Jill Bechtold, and Aneta Siemiginowska (June 2009). "Are the Variations in Quasar Optical Flux Driven by Thermal Fluctuations?" In: ApJ 698.1, pp. 895–910. DOI: 10.1088/0004-637X/698/1/895. arXiv: 0903.5315 [astro-ph.CO].

Kennicutt Robert C., Jr. (Sept. 1989). “The Star Formation Law in Galactic Disks”. In: ApJ 344, p. 685. DOI: 10.1086/167834.

— (Jan. 1998a). “Star Formation in Galaxies Along the Hubble Sequence”. In: ARA&A 36, pp. 189–232. DOI: 10.1146/annurev.astro.36.1.189. arXiv: astro-ph/9807187 [astro-ph].

— (May 1998b). “The Global Schmidt Law in Star-forming Galaxies”. In: ApJ 498.2, pp. 541–552. DOI: 10.1086/305588. arXiv: astro-ph/9712213 [astro-ph].

Kennicutt Robert C., Jr. et al. (Dec. 2007). “Star Formation in NGC 5194 (M51a). II. The Spatially Resolved Star Formation Law”. In: ApJ 671.1, pp. 333–348. DOI: 10.1086/522300. arXiv: 0708.0922 [astro-ph].

Kennicutt, Robert C. and Neal J. Evans (Sept. 2012). “Star Formation in the Milky Way and Nearby Galaxies”. In: ARA&A 50, pp. 531–608. DOI: 10.1146/annurev-astro-081811-125610. arXiv: 1204.3552 [astro-ph.GA].

Kereš, Dušan et al. (May 2009). “Galaxies in a simulated ΛCDM Universe - I. Cold mode and hot cores”. In: MNRAS 395.1, pp. 160–179. DOI: 10.1111/j.1365-2966.2009.14541.x. arXiv: 0809.1430 [astro-ph].

Kewley, L. J. et al. (July 2001). “Theoretical Modeling of Starburst Galaxies”. In: ApJ 556.1, pp. 121–140. DOI: 10.1086/321545. arXiv: astro-ph/0106324 [astro-ph].

Kewley, Lisa J. et al. (Nov. 2006). “The host galaxies and classification of active galactic nuclei”. In: MNRAS 372.3, pp. 961–976. DOI: 10.1111/j.1365-2966.2006.10859.x. arXiv: astro-ph/0605681 [astro-ph].

Kimm, Taysun et al. (Apr. 2009). “The correlation of star formation quenching with internal galaxy properties and environment”. In: MNRAS 394.3, pp. 1131–1147. DOI: 10.1111/j.1365-2966.2009.14414.x. arXiv: 0810.2794 [astro-ph].

Kormendy, John and Luis C. Ho (Aug. 2013). “Coevolution (Or Not) of Supermassive Black Holes and Host Galaxies”. In: ARA&A 51.1, pp. 511–653. DOI: 10.1146/annurev-astro-082708-101811. arXiv: 1304.7762 [astro-ph.CO].

Kormendy, John and Jr. Kennicutt Robert C. (Sept. 2004). "Secular Evolution and the Formation of Pseudobulges in Disk Galaxies". In: ARA&A 42.1, pp. 603–683. DOI: 10.1146/annurev.astro.42.053102.134024. arXiv: astro-ph/0407343 [astro-ph].

Kozłowski, Szymon (Aug. 2016). "Revisiting Stochastic Variability of AGNs with Structure Functions". In: ApJ 826.2, 118, p. 118. DOI: 10.3847/0004-637X/826/2/118. arXiv: 1604.05858 [astro-ph.GA].

Kravtsov, Andrey V. (June 2003). "On the Origin of the Global Schmidt Law of Star Formation". In: ApJ 590.1, pp. L1–L4. DOI: 10.1086/376674. arXiv: astro-ph/0303240 [astro-ph].

Kroupa, Pavel (Apr. 2001). "On the variation of the initial mass function". In: MNRAS 322.2, pp. 231–246. DOI: 10.1046/j.1365-8711.2001.04022.x. arXiv: astro-ph/0009005 [astro-ph].

Lacey, Cedric and Shaun Cole (June 1993). "Merger rates in hierarchical models of galaxy formation". In: MNRAS 262.3, pp. 627–649. DOI: 10.1093/mnras/262.3.627.

Larison, Conor et al. (June 2023). "Environmental Dependence of Type Ia Supernovae in Low-Redshift Galaxy Clusters". In: *arXiv e-prints*, arXiv:2306.01088, arXiv:2306.01088. DOI: 10.48550/arXiv.2306.01088. arXiv: 2306.01088 [astro-ph.HE].

Leloudas, G. et al. (May 2015). "Spectroscopy of superluminous supernova host galaxies. A preference of hydrogen-poor events for extreme emission line galaxies". In: MNRAS 449.1, pp. 917–932. DOI: 10.1093/mnras/stv320. arXiv: 1409.8331 [astro-ph.GA].

Levan, A. J. et al. (Jan. 2014). "A New Population of Ultra-long Duration Gamma-Ray Bursts". In: ApJ 781.1, 13, p. 13. DOI: 10.1088/0004-637X/781/1/13. arXiv: 1302.2352 [astro-ph.HE].

Li, Yuexing, Mordecai-Mark Mac Low, and Ralf S. Klessen (Mar. 2006). "Star Formation in Isolated Disk Galaxies. II. Schmidt Laws and Efficiency of Gravitational Collapse". In: ApJ 639.2, pp. 879–896. DOI: 10.1086/499350. arXiv: astro-ph/0508054 [astro-ph].

Lucas, William E., Ian A. Bonnell, and James E. Dale (Apr. 2020). "Supernova feedback and the energy deposition in molecular clouds". In: MNRAS 493.4, pp. 4700–4710. DOI: 10.1093/mnras/staa451. arXiv: 2002.04868 [astro-ph.GA].

Luna, A. et al. (Apr. 2006). "Molecular Gas, Kinematics, and OB Star Formation in the Spiral Arms of the Southern Milky Way". In: ApJ 641.2, pp. 938–948. DOI: 10.1086/500163. arXiv: astro-ph/0512046 [astro-ph].

Lunnan, R. et al. (June 2014). "Hydrogen-poor Superluminous Supernovae and Long-duration Gamma-Ray Bursts Have Similar Host Galaxies". In: ApJ 787.2, 138, p. 138. DOI: 10.1088/0004-637X/787/2/138. arXiv: 1311.0026 [astro-ph.HE].

Lunnan, R. et al. (May 2015). "Zooming In on the Progenitors of Superluminous Supernovae With the HST". In: ApJ 804.2, 90, p. 90. DOI: 10.1088/0004-637X/804/2/90. arXiv: 1411.1060 [astro-ph.HE].

Lunnan, R. et al. (Jan. 2018). "Hydrogen-poor Superluminous Supernovae from the Pan-STARRS1 Medium Deep Survey". In: ApJ 852.2, 81, p. 81. DOI: 10.3847/1538-4357/aa9f1a. arXiv: 1708.01619 [astro-ph.HE].

Magee, M. et al. (Feb. 2021). "ePESSTO+ Transient Classification Report for 2021-02-04". In: *Transient Name Server Classification Report* 2021-338, pp. 1–338.

Magorrian, John et al. (June 1998). "The Demography of Massive Dark Objects in Galaxy Centers". In: AJ 115.6, pp. 2285–2305. DOI: 10.1086/300353. arXiv: astro-ph/9708072 [astro-ph].

Maiolino, R. et al. (Sept. 2012). "Evidence of strong quasar feedback in the early Universe". In: MNRAS 425.1, pp. L66–L70. DOI: 10.1111/j.1745-3933.2012.01303.x. arXiv: 1204.2904 [astro-ph.CO].

Mantha, Kameswara Bharadwaj et al. (Apr. 2018). "Major merging history in CANDELS. I. Evolution of the incidence of massive galaxy-galaxy pairs from z = 3 to z ∼ 0". In: MNRAS 475.2, pp. 1549–1573. DOI: 10.1093/mnras/stx3260. arXiv: 1712.06611 [astro-ph.GA].

Marinacci, Federico et al. (Nov. 2018). "First results from the IllustrisTNG simulations: radio haloes and magnetic fields". In: MNRAS 480.4, pp. 5113–5139. DOI: 10.1093/mnras/sty2206. arXiv: 1707.03396 [astro-ph.CO].

Martin, D. Christopher et al. (Jan. 2005). "The Galaxy Evolution Explorer: A Space Ultraviolet Survey Mission". In: ApJ 619.1, pp. L1–L6. DOI: 10.1086/426387. arXiv: astro-ph/0411302 [astro-ph].

Martizzi, Davide et al. (July 2016). "Supernova feedback in a local vertically stratified medium: interstellar turbulence and galactic winds". In: MNRAS 459.3, pp. 2311–2326. DOI: 10.1093/mnras/stw745. arXiv: 1601.03399 [astro-ph.GA].

Masci, Frank J. et al. (Jan. 2019). "The Zwicky Transient Facility: Data Processing, Products, and Archive". In: PASP 131.995, p. 018003. DOI: 10.1088/1538-3873/aae8ac. arXiv: 1902.01872 [astro-ph.IM].

Mateo, Mario L. (Jan. 1998). "Dwarf Galaxies of the Local Group". In: ARA&A 36, pp. 435–506. DOI: 10.1146/annurev.astro.36.1.435. arXiv: astro-ph/9810070 [astro-ph].

McConnell, Nicholas J. and Chung-Pei Ma (Feb. 2013). "Revisiting the Scaling Relations of Black Hole Masses and Host Galaxy Properties". In: ApJ 764.2, 184, p. 184. DOI: 10.1088/0004-637X/764/2/184. arXiv: 1211.2816 [astro-ph.CO].

McGee, S. L., R. G. Bower, and M. L. Balogh (July 2014). "Overconsumption, outflows and the quenching of satellite galaxies." In: MNRAS 442, pp. L105–L109. DOI: 10.1093/mnrasl/slu066. arXiv: 1404.6251 [astro-ph.GA].

McGee, Sean L. et al. (Dec. 2009). "The accretion of galaxies into groups and clusters". In: MNRAS 400.2, pp. 937–950. DOI: 10.1111/j.1365-2966.2009.15507.x. arXiv: 0908.0750 [astro-ph.CO].

McGee, Sean L. et al. (May 2011). "The Dawn of the Red: star formation histories of group galaxies over the past 5 billion years". In: MNRAS 413.2, pp. 996–1012. DOI: 10.1111/j.1365-2966.2010.18189.x. arXiv: 1012.2388 [astro-ph.CO].

McGuire, Brett A. (Dec. 2018). "2018 Census of Interstellar, Circumstellar, Extragalactic, Protoplanetary Disk, and Exoplanetary Molecules". In: ApJS 239.2, 17, p. 17. DOI: 10.3847/1538-4365/aae5d2. arXiv: 1809.09132 [astro-ph.GA].

McHardy, I. M. et al. (Dec. 2006). "Active galactic nuclei as scaled-up Galactic black holes". In: Nature 444.7120, pp. 730–732. DOI: 10.1038/nature05389. arXiv: astro-ph/0612273 [astro-ph].

McNamara, B. R. et al. (May 2000). "Chandra X-Ray Observations of the Hydra A Cluster: An Interaction between the Radio Source and the X-Ray-emitting Gas". In: ApJ 534.2, pp. L135–L138. DOI: 10.1086/312662. arXiv: astro-ph/0001402 [astro-ph].

McNamara, B. R. et al. (Sept. 2006). "The Starburst in the Abell 1835 Cluster Central Galaxy: A Case Study of Galaxy Formation Regulated by an Outburst from a Supermassive Black Hole". In: ApJ 648.1, pp. 164–175. DOI: 10.1086/505859. arXiv: astro-ph/0604044 [astro-ph].

Melnick, J. and R. De Propris (May 2013). "The spectral energy distributions of K+A galaxies from the UV to the mid-IR: stellar populations, star formation and hot dust". In: MNRAS 431.3, pp. 2034–2049. DOI: 10.1093/mnras/stt199. arXiv: 1301.5325 [astro-ph.CO].

Mihos, J. Christopher and Lars Hernquist (June 1996). "Gasdynamics and Starbursts in Major Mergers". In: ApJ 464, p. 641. DOI: 10.1086/177353. arXiv: astro-ph/9512099 [astro-ph].

Misiriotis, A. et al. (Nov. 2006). "The distribution of the ISM in the Milky Way. A three-dimensional large-scale model". In: A&A 459.1, pp. 113–123. DOI: 10.1051/0004-6361:20054618. arXiv: astro-ph/0607638 [astro-ph].

Moore, Ben, George Lake, and Neal Katz (Mar. 1998). "Morphological Transformation from Galaxy Harassment". In: ApJ 495.1, pp. 139–151. DOI: 10.1086/305264. arXiv: astro-ph/9701211 [astro-ph].

Moore, Ben et al. (Feb. 1996). "Galaxy harassment and the evolution of clusters of galaxies". In: Nature 379.6566, pp. 613–616. DOI: 10.1038/379613a0. arXiv: astro-ph/9510034 [astro-ph].

Morgan, Christopher W. et al. (Apr. 2010). "The Quasar Accretion Disk Size-Black Hole Mass Relation". In: ApJ 712.2, pp. 1129–1136. DOI: 10.1088/0004-637X/712/2/1129. arXiv: 1002.4160 [astro-ph.CO].

Morrissey, Patrick et al. (Dec. 2007). "The Calibration and Data Products of GALEX". In: ApJS 173.2, pp. 682–697. DOI: 10.1086/520512. arXiv: 0706.0755 [astro-ph].

Muzzin, Adam et al. (Nov. 2014). "The Phase Space and Stellar Populations of Cluster Galaxies at z ∼1: Simultaneous Constraints on the Location and Timescale of Satellite Quenching". In: ApJ 796.1, 65, p. 65. DOI: 10.1088/0004-637X/796/1/65. arXiv: 1402.7077 [astro-ph.GA].

Naab, Thorsten and Jeremiah P. Ostriker (Aug. 2017). "Theoretical Challenges in Galaxy Formation". In: ARA&A 55.1, pp. 59–109. DOI: 10.1146/annurev-astro-081913-040019. arXiv: 1612.06891 [astro-ph.GA].

Naiman, Jill P. et al. (June 2018). "First results from the IllustrisTNG simulations: a tale of two elements - chemical evolution of magnesium and europium". In: MNRAS 477.1, pp. 1206–1224. DOI: 10.1093/mnras/sty618. arXiv: 1707.03401 [astro-ph.GA].

Neill, James D. et al. (Jan. 2011). "The Extreme Hosts of Extreme Supernovae". In: ApJ 727.1, 15, p. 15. DOI: 10.1088/0004-637X/727/1/15. arXiv: 1011.3512 [astro-ph.CO].

Nelson, Dylan et al. (Mar. 2018). "First results from the IllustrisTNG simulations: the galaxy colour bimodality". In: MNRAS 475.1, pp. 624–647. DOI: 10.1093/mnras/stx3040. arXiv: 1707.03395 [astro-ph.GA].

Nelson, Dylan et al. (May 2019). "The IllustrisTNG simulations: public data release". In: *Computational Astrophysics and Cosmology* 6.1, 2, p. 2. DOI: 10.1186/s40668-019-0028-x. arXiv: 1812.05609 [astro-ph.GA].

Nicholl, M. and S. J. Smartt (Mar. 2016). "Seeing double: the frequency and detectability of double-peaked superluminous supernova light curves". In: MNRAS 457.1, pp. L79–L83. DOI: 10.1093/mnrasl/slv210. arXiv: 1511.03740 [astro-ph.SR].

Nicholl, M. et al. (Nov. 2014). "Superluminous supernovae from PESSTO". In: MNRAS 444.3, pp. 2096–2113. DOI: 10.1093/mnras/stu1579. arXiv: 1405.1325 [astro-ph.HE].

Nicholl, M. et al. (July 2015a). "LSQ14bdq: A Type Ic Super-luminous Supernova with a Double-peaked Light Curve". In: ApJ 807.1, L18, p. L18. DOI: 10.1088/2041-8205/807/1/L18. arXiv: 1505.01078 [astro-ph.SR].

Nicholl, M. et al. (Oct. 2015b). "On the diversity of superluminous supernovae: ejected mass as the dominant factor". In: MNRAS 452.4, pp. 3869–3893. DOI: 10.1093/mnras/stv1522. arXiv: 1503.03310 [astro-ph.SR].

Nicholl, M. et al. (July 2016a). "SN 2015BN: A Detailed Multi-wavelength View of a Nearby Superluminous Supernova". In: ApJ 826.1, 39, p. 39. DOI: 10.3847/0004-637X/826/1/39. arXiv: 1603.04748 [astro-ph.SR].

Nicholl, M. et al. (Sept. 2016b). "Superluminous Supernova SN 2015bn in the Nebular Phase: Evidence for the Engine-powered Explosion of a Stripped Massive Star". In: ApJ 828.2, L18, p. L18. DOI: 10.3847/2041-8205/828/2/L18. arXiv: 1608.02995 [astro-ph.HE].

Nicholl, M. et al. (Nov. 2019). "C-SNAILS Transient Classification Report for 2019-11-04". In: *Transient Name Server Classification Report* 2019-2271, p. 1.

Nicholl, Matt (Oct. 2021). "Superluminous supernovae: an explosive decade". In: *Astronomy and Geophysics* 62.5, pp. 5.34–5.42. DOI: 10.1093/astrogeo/atab092. arXiv: 2109.08697 [astro-ph.HE].

Nicholl, Matt, James Guillochon, and Edo Berger (Nov. 2017). "The Magnetar Model for Type I Superluminous Supernovae. I. Bayesian Analysis of the Full Multicolor Light-curve Sample with MOSFiT". In: ApJ 850.1, 55, p. 55. DOI: 10.3847/1538-4357/aa9334. arXiv: 1706.00825 [astro-ph.HE].

Novak, Gregory S., Jeremiah P. Ostriker, and Luca Ciotti (Aug. 2011). "Feedback from Central Black Holes in Elliptical Galaxies: Two-dimensional Models Compared to One-dimensional Models". In: ApJ 737.1, 26, p. 26. DOI: 10.1088/0004-637X/737/1/26. arXiv: 1007.3505 [astro-ph.GA].

Nulsen, P. E. J. et al. (Jan. 2007). "AGN Heating Through Cavities and Shocks". In: *Heating versus Cooling in Galaxies and Clusters of Galaxies*. Ed. by H. Böhringer et al., p. 210. DOI: 10.1007/978-3-540-73484-0_37. arXiv: astro-ph/0611136 [astro-ph].

Nulsen, Paul et al. (Dec. 2009). "Radio Mode Outbursts in Giant Elliptical Galaxies". In: *The Monster's Fiery Breath: Feedback in Galaxies, Groups, and Clusters*. Ed. by Sebastian Heinz and Eric Wilcots. Vol. 1201. American Institute of Physics Conference Series, pp. 198–201. DOI: 10.1063/1.3293033. arXiv: 0909.1809 [astro-ph.GA].

Oman, Kyle A., Michael J. Hudson, and Peter S. Behroozi (May 2013). "Disentangling satellite galaxy populations using orbit tracking in simulations". In: MNRAS 431.3, pp. 2307–2316. DOI: 10.1093/mnras/stt328. arXiv: 1301.6757 [astro-ph.CO].

Omand, C. M. B., M. L. Balogh, and B. M. Poggianti (Jan. 2015). "VizieR Online Data Catalog: SIM2D parameters of SDSS-DR7 galaxies (Omand+, 2014)". In: *VizieR Online Data Catalog*, J/MNRAS/440/843, J/MNRAS/440/843.

Omand, Conor M. B., Michael L. Balogh, and Bianca M. Poggianti (May 2014). "The connection between galaxy structure and quenching efficiency". In: MNRAS 440.1, pp. 843–858. DOI: 10.1093/mnras/stu331. arXiv: 1402.3394 [astro-ph.GA].

Ørum, Simon Vanggaard et al. (Nov. 2020). "The interacting nature of dwarf galaxies hosting superluminous supernovae". In: A&A 643, A47, A47. DOI: 10.1051/0004-6361/202038176. arXiv: 2009.03925 [astro-ph.GA].

Owers, Matt S. et al. (Mar. 2019). "The SAMI Galaxy Survey: Quenching of Star Formation in Clusters I. Transition Galaxies". In: ApJ 873.1, 52, p. 52. DOI: 10.3847/1538-4357/ab0201. arXiv: 1901.08185 [astro-ph.GA].

Paccagnella, A. et al. (Apr. 2017). "OmegaWINGS: The First Complete Census of Post-starburst Galaxies in Clusters in the Local Universe". In: ApJ 838.2, 148, p. 148. DOI: 10.3847/1538-4357/aa64d7. arXiv: 1703.03204 [astro-ph.GA].

Paccagnella, A. et al. (Jan. 2019). "The strong correlation between post-starburst fraction and environment". In: MNRAS 482.1, pp. 881–894. DOI: 10.1093/mnras/sty2728. arXiv: 1805.11475 [astro-ph.GA].

Page, M. J. et al. (May 2012). "The suppression of star formation by powerful active galactic nuclei". In: Nature 485.7397, pp. 213–216. DOI: 10.1038/nature11096. arXiv: 1310.4147 [astro-ph.CO].

Pastorello, A. et al. (Nov. 2010). "Ultra-bright Optical Transients are Linked with Type Ic Supernovae". In: ApJ 724.1, pp. L16–L21. DOI: 10.1088/2041-8205/724/1/L16. arXiv: 1008.2674 [astro-ph.SR].

Pawlik, M. M. et al. (Mar. 2019). "The diverse evolutionary pathways of post-starburst galaxies". In: *Nature Astronomy* 3, pp. 440–446. DOI: 10.1038/s41550-019-0725-z. arXiv: 1903.11050 [astro-ph.GA].

Pearson, W. J. et al. (Nov. 2019). "Effect of galaxy mergers on star-formation rates". In: A&A 631, A51, A51. DOI: 10.1051/0004-6361/201936337. arXiv: 1908.10115 [astro-ph.GA].

Pedlar, A. et al. (Oct. 1990). "The radio structure of NGC 1275." In: MNRAS 246, p. 477.

Peng, Y., R. Maiolino, and R. Cochrane (May 2015). "Strangulation as the primary mechanism for shutting down star formation in galaxies". In: Nature 521.7551, pp. 192–195. DOI: 10.1038/nature14439. arXiv: 1505.03143 [astro-ph.GA].

Peng, Ying-jie et al. (Sept. 2010). "Mass and Environment as Drivers of Galaxy Evolution in SDSS and zCOSMOS and the Origin of the Schechter Function". In: ApJ 721.1, pp. 193–221. DOI: 10.1088/0004-637X/721/1/193. arXiv: 1003.4747 [astro-ph.CO].

Peng, Ying-jie et al. (Sept. 2012). "Mass and Environment as Drivers of Galaxy Evolution. II. The Quenching of Satellite Galaxies as the Origin of Environmental Effects". In: ApJ 757.1, 4, p. 4. DOI: 10.1088/0004-637X/757/1/4. arXiv: 1106.2546 [astro-ph.CO].

Perez-Fournon, I. et al. (Aug. 2020). "SGLF Transient Classification Report for 2020-08-11". In: *Transient Name Server Classification Report* 2020-2456, p. 1.

Perley, D. et al. (Sept. 2019). "ZTF Transient Classification Report for 2019-09-02". In: *Transient Name Server Classification Report* 2019-1712, p. 1.

Perley, D. et al. (Oct. 2020a). "ZTF Transient Classification Report for 2020-10-14". In: *Transient Name Server Classification Report* 2020-3125, p. 1.

Perley, D. A. (Aug. 2019). "ZTF Transient Classification Report for 2019-08-27". In: *Transient Name Server Classification Report* 2019-1646, p. 1.

Perley, D. A. et al. (Oct. 2016a). "Host-galaxy Properties of 32 Low-redshift Superluminous Supernovae from the Palomar Transient Factory". In: ApJ 830.1, 13, p. 13. DOI: 10.3847/0004-637X/830/1/13. arXiv: 1604.08207 [astro-ph.HE].

Perley, D. A. et al. (Jan. 2016b). "The Swift GRB Host Galaxy Legacy Survey. II. Rest-frame Near-IR Luminosity Distribution and Evidence for a Near-solar Metallicity Threshold". In: ApJ 817.1, 8, p. 8. DOI: 10.3847/0004-637X/817/1/8. arXiv: 1504.02479 [astro-ph.GA].

Perley, D. A. et al. (June 2020b). "ZTF Transient Classification Report for 2020-06-10". In: *Transient Name Server Classification Report* 2020-1749, p. 1.

Perley, D. A. et al. (May 2021). "ZTF Transient Classification Report for 2021-05-15". In: *Transient Name Server Classification Report* 2021-1649, pp. 1–1649.

Perley, Daniel A. et al. (Nov. 2020c). "The Zwicky Transient Facility Bright Transient Survey. II. A Public Statistical Sample for Exploring Supernova Demographics". In: ApJ 904.1, 35, p. 35. DOI: 10.3847/1538-4357/abbd98. arXiv: 2009.01242 [astro-ph.HE].

Pillepich, Annalisa et al. (Mar. 2018). "First results from the IllustrisTNG simulations: the stellar mass content of groups and clusters of galaxies". In: MNRAS 475.1, pp. 648–675. DOI: 10.1093/mnras/stx3112. arXiv: 1707.03406 [astro-ph.GA].

Poggianti, Bianca M. et al. (June 1999). "The Star Formation Histories of Galaxies in Distant Clusters". In: ApJ 518.2, pp. 576–593. DOI: 10.1086/307322. arXiv: astro-ph/9901264 [astro-ph].

Poggianti, Bianca M. et al. (July 2017). "GASP. I. Gas Stripping Phenomena in Galaxies with MUSE". In: ApJ 844.1, 48, p. 48. DOI: 10.3847/1538-4357/aa78ed. arXiv: 1704.05086 [astro-ph.GA].

Poggianti, Bianca M. et al. (Feb. 2019). "GASP XIII. Star formation in gas outside galaxies". In: MNRAS 482.4, pp. 4466–4502. DOI: 10.1093/mnras/sty2999. arXiv: 1811.00823 [astro-ph.GA].

Poidevin, F. et al. (Feb. 2020). "SGLF Transient Classification Report for 2020-02-14". In: *Transient Name Server Classification Report* 2020-500, p. 1.

Poidevin, F. et al. (July 2021). "SGLF Transient Classification Report for 2021-07-01". In: *Transient Name Server Classification Report* 2021-2271, pp. 1–2271.

Poidevin, F. et al. (May 2022). "SGLF Transient Classification Report for 2022-05-03". In: *Transient Name Server Classification Report* 2022-1175, p. 1.

Postman, M. and M. J. Geller (June 1984). "The morphology-density relation - The group connection." In: ApJ 281, pp. 95–99. DOI: 10.1086/162078.

Pracy, Michael B. et al. (July 2009). "The kinematics and spatial distribution of stellar populations in E+A galaxies". In: MNRAS 396.3, pp. 1349–1369. DOI: 10.1111/j.1365-2966.2009.14836.x. arXiv: 0903.4719 [astro-ph.CO].

Prentice, S. J. et al. (Aug. 2019a). "TCD Transient Classification Report for 2019-08-23". In: *Transient Name Server Classification Report* 2019-1598, p. 1.

— (Nov. 2019b). "TCD Transient Classification Report for 2019-11-11". In: *Transient Name Server Classification Report* 2019-2339, p. 1.

Puglisi, Annagrazia et al. (Mar. 2021). "A titanic interstellar medium ejection from a massive starburst galaxy at redshift 1.4". In: *Nature Astronomy* 5, pp. 319–330. DOI: 10.1038/s41550-020-01268-x. arXiv: 2101.04021 [astro-ph.GA].

Quimby, R. M. et al. (June 2011). "Hydrogen-poor superluminous stellar explosions". In: Nature 474.7352, pp. 487–489. DOI: 10.1038/nature10095. arXiv: 0910.0059 [astro-ph.CO].

Quimby, Robert M. et al. (Mar. 2018). "Spectra of Hydrogen-poor Superluminous Supernovae from the Palomar Transient Factory". In: ApJ 855.1, 2, p. 2. DOI: 10.3847/1538-4357/aaac2f. arXiv: 1802.07820 [astro-ph.HE].

Randall, S. W. et al. (Jan. 2011). "Shocks and Cavities from Multiple Outbursts in the Galaxy Group NGC 5813: A Window to Active Galactic Nucleus Feedback". In: ApJ 726.2, 86, p. 86. DOI: 10.1088/0004-637X/726/2/86. arXiv: 1006.4379 [astro-ph.CO].

Reines, Amy E. and Marta Volonteri (Nov. 2015). "Relations between Central Black Hole Mass and Total Galaxy Stellar Mass in the Local Universe". In: ApJ 813.2, 82, p. 82. DOI: 10.1088/0004-637X/813/2/82. arXiv: 1508.06274 [astro-ph.GA].

Richardson, Dean et al. (Feb. 2002). "A Comparative Study of the Absolute Magnitude Distributions of Supernovae". In: AJ 123.2, pp. 745–752. DOI: 10.1086/338318. arXiv: astro-ph/0112051 [astro-ph].

Rodríguez Montero, Francisco et al. (Dec. 2019). "Mergers, starbursts, and quenching in the SIMBA simulation". In: MNRAS 490.2, pp. 2139–2154. DOI: 10.1093/mnras/stz2580. arXiv: 1907.12680 [astro-ph.GA].

Rodriguez-Gomez, Vicente et al. (May 2015). "The merger rate of galaxies in the Illustris simulation: a comparison with observations and semi-empirical models". In: MNRAS 449.1, pp. 49–64. DOI: 10.1093/mnras/stv264. arXiv: 1502.01339 [astro-ph.GA].

Rubin, V. C., Jr. Ford W. K., and N. Thonnard (June 1980). "Rotational properties of 21 SC galaxies with a large range of luminosities and radii, from NGC 4605 (R=4kpc) to UGC 2885 (R=122kpc)." In: ApJ 238, pp. 471–487. DOI: 10.1086/158003.

Rupke, David S. N. and Sylvain Veilleux (Mar. 2011). "Integral Field Spectroscopy of Massive, Kiloparsec-scale Outflows in the Infrared-luminous QSO Mrk 231". In: ApJ 729.2, L27, p. L27. DOI: 10.1088/2041-8205/729/2/L27. arXiv: 1102.4349 [astro-ph.GA].

Saintonge, Amélie and Barbara Catinella (Aug. 2022). "The Cold Interstellar Medium of Galaxies in the Local Universe". In: ARA&A 60, pp. 319–361. DOI: 10.1146/annurev-astro-021022-043545. arXiv: 2202.00690 [astro-ph.GA].

Saintonge, Amélie et al. (Dec. 2017). "xCOLD GASS: The Complete IRAM 30 m Legacy Survey of Molecular Gas for Galaxy Evolution Studies". In: ApJS 233.2, 22, p. 22. DOI: 10.3847/1538-4365/aa97e0. arXiv: 1710.02157 [astro-ph.GA].

Salim, S. (Dec. 2014). "Green Valley Galaxies". In: *Serbian Astronomical Journal* 189, pp. 1–14. DOI: 10.2298/SAJ1489001S. arXiv: 1501.01963 [astro-ph.GA].

Salim, Samir, Médéric Boquien, and Janice C. Lee (May 2018). "Dust Attenuation Curves in the Local Universe: Demographics and New Laws for Star-forming Galaxies and High-redshift Analogs". In: ApJ 859.1, 11, p. 11. DOI: 10.3847/1538-4357/aabf3c. arXiv: 1804.05850 [astro-ph.GA].

Salim, Samir et al. (Dec. 2007). "UV Star Formation Rates in the Local Universe". In: ApJS 173.2, pp. 267–292. DOI: 10.1086/519218. arXiv: 0704.3611 [astro-ph].

Salim, Samir et al. (Nov. 2016). "GALEX-SDSS-WISE Legacy Catalog (GSWLC): Star Formation Rates, Stellar Masses, and Dust Attenuations of 700,000 Low-redshift Galaxies". In: ApJS 227.1, 2, p. 2. DOI: 10.3847/0067-0049/227/1/2. arXiv: 1610.00712 [astro-ph.GA].

Salpeter, Edwin E. (Jan. 1955). "The Luminosity Function and Stellar Evolution." In: ApJ 121, p. 161. DOI: 10.1086/145971.

Sanders, J. S. and A. C. Fabian (Oct. 2008). "Sound waves in the intracluster medium of the Centaurus cluster". In: MNRAS 390.1, pp. L93–L97. DOI: 10.1111/j.1745-3933.2008.00549.x. arXiv: 0808.2384 [astro-ph].

Sanders, J. S. et al. (Feb. 2010). "Deep high-resolution X-ray spectra from cool-core clusters". In: MNRAS 402.1, pp. 127–144. DOI: 10.1111/j.1365-2966.2009.15902.x. arXiv: 0910.3793 [astro-ph.CO].

Sartori, Lia F. et al. (May 2018). "A model for AGN variability on multiple time-scales". In: MNRAS 476.1, pp. L34–L38. DOI: 10.1093/mnrasl/sly025. arXiv: 1802.05717 [astro-ph.GA].

Satyapal, Shobita et al. (June 2014). "Galaxy pairs in the Sloan Digital Sky Survey - IX. Merger-induced AGN activity as traced by the Wide-field Infrared Survey Explorer". In: MNRAS 441.2, pp. 1297–1304. DOI: 10.1093/mnras/stu650. arXiv: 1403.7531 [astro-ph.GA].

Schawinski, Kevin et al. (May 2014). "The green valley is a red herring: Galaxy Zoo reveals two evolutionary pathways towards quenching of star formation in early- and late-type galaxies". In: MNRAS 440.1, pp. 889–907. DOI: 10.1093/mnras/stu327. arXiv: 1402.4814 [astro-ph.GA].

Schaye, Joop et al. (Jan. 2015). "The EAGLE project: simulating the evolution and assembly of galaxies and their environments". In: MNRAS 446.1, pp. 521–554. DOI: 10.1093/mnras/stu2058. arXiv: 1407.7040 [astro-ph.GA].

Schmidt, Maarten (Mar. 1959). "The Rate of Star Formation." In: ApJ 129, p. 243. DOI: 10.1086/146614.

Schmidt, R. W., S. W. Allen, and A. C. Fabian (Nov. 2001). "Chandra observations of the galaxy cluster Abell 1835". In: MNRAS 327.4, pp. 1057–1070. DOI: 10.1046/j.1365-8711.2001.04809.x. arXiv: astro-ph/0107311 [astro-ph].

Schulze, S. et al. (Jan. 2018). "Cosmic evolution and metal aversion in superluminous supernova host galaxies". In: MNRAS 473.1, pp. 1258–1285. DOI: 10.1093/mnras/stx2352. arXiv: 1612.05978 [astro-ph.GA].

Schulze, Steve et al. (Aug. 2021). "The Palomar Transient Factory Core-collapse Supernova Host-galaxy Sample. I. Host-galaxy Distribution Functions and Environment Dependence of Core-collapse Supernovae". In: ApJS 255.2, 29, p. 29. DOI: 10.3847/1538-4365/abff5e. arXiv: 2008.05988 [astro-ph.GA].

Shen, Yue et al. (Apr. 2019). "The Sloan Digital Sky Survey Reverberation Mapping Project: Sample Characterization". In: ApJS 241.2, 34, p. 34. DOI: 10.3847/1538-4365/ab074f. arXiv: 1810.01447 [astro-ph.GA].

Sheth, Kartik et al. (Oct. 2005). "Secular Evolution via Bar-driven Gas Inflow: Results from BIMA SONG". In: ApJ 632.1, pp. 217–226. DOI: 10.1086/432409. arXiv: astro-ph/0505393 [astro-ph].

Sheth, Kartik et al. (Mar. 2008). "Evolution of the Bar Fraction in COSMOS: Quantifying the Assembly of the Hubble Sequence". In: ApJ 675.2, pp. 1141–1155. DOI: 10.1086/524980. arXiv: 0710.4552 [astro-ph].

Simard, Luc et al. (Sept. 2011). "A Catalog of Bulge+disk Decompositions and Updated Photometry for 1.12 Million Galaxies in the Sloan Digital Sky Survey". In: ApJS 196.1, 11, p. 11. DOI: 10.1088/0067-0049/196/1/11. arXiv: 1107.1518 [astro-ph.CO].

Smee, Stephen A. et al. (Aug. 2013). "The Multi-object, Fiber-fed Spectrographs for the Sloan Digital Sky Survey and the Baryon Oscillation Spectroscopic Survey". In: AJ 146.2, 32, p. 32. DOI: 10.1088/0004-6256/146/2/32. arXiv: 1208.2233 [astro-ph.IM].

Smethurst, R. J. et al. (Aug. 2017). "Galaxy Zoo: the interplay of quenching mechanisms in the group environment". In: MNRAS 469.3, pp. 3670–3687. DOI: 10.1093/mnras/stx973. arXiv: 1704.06269 [astro-ph.GA].

Smethurst, R. J. et al. (Nov. 2022). "Evidence for non-merger co-evolution of galaxies and their supermassive black holes". In: *arXiv e-prints*, arXiv:2211.13677, arXiv:2211.13677. DOI: 10.48550/arXiv.2211.13677. arXiv: 2211.13677 [astro-ph.GA].

Smith, K. W. et al. (Jan. 2019). "Lasair: The Transient Alert Broker for LSST:UK". In: *Research Notes of the American Astronomical Society* 3.1, 26, p. 26. DOI: 10.3847/2515-5172/ab020f.

Smith, K. W. et al. (Aug. 2020). "Design and Operation of the ATLAS Transient Science Server". In: PASP 132.1014, 085002, p. 085002. DOI: 10.1088/1538-3873/ab936e. arXiv: 2003.09052 [astro-ph.IM].

Smith, K. W. et al. (Mar. 2022). "ePESSTO+ Transient Classification Report for 2022-03-02". In: *Transient Name Server Classification Report* 2022-583, p. 1.

Smith, Krista Lynne et al. (Apr. 2018a). "The Kepler Light Curves of AGN: A Detailed Analysis". In: ApJ 857.2, 141, p. 141. DOI: 10.3847/1538-4357/aab88d. arXiv: 1803.06436 [astro-ph.HE].

Smith, Mathew et al. (Aug. 2012). "The SDSS-II Supernova Survey: Parameterizing the Type Ia Supernova Rate as a Function of Host Galaxy Properties". In: ApJ 755.1, 61, p. 61. DOI: 10.1088/0004-637X/755/1/61. arXiv: 1108.4923 [astro-ph.CO].

Smith, Matthew C., Debora Sijacki, and Sijing Shen (July 2018b). "Supernova feedback in numerical simulations of galaxy formation: separating physics from numerics". In: MNRAS 478.1, pp. 302–331. DOI: 10.1093/mnras/sty994. arXiv: 1709.03515 [astro-ph.GA].

Smith, Nathan and Richard McCray (Dec. 2007). "Shell-shocked Diffusion Model for the Light Curve of SN 2006gy". In: ApJ 671.1, pp. L17–L20. DOI: 10.1086/524681. arXiv: 0710.3428 [astro-ph].

Smith, R. et al. (Dec. 2015). "The sensitivity of harassment to orbit: mass loss from early-type dwarfs in galaxy clusters". In: MNRAS 454.3, pp. 2502–2516. DOI: 10.1093/mnras/stv2082. arXiv: 1509.02537 [astro-ph.GA].

Smith, Russell J. et al. (Feb. 2009). "A spectroscopic survey of dwarf galaxies in the Coma cluster: stellar populations, environment and downsizing". In: MNRAS 392.4, pp. 1265–1294. DOI: 10.1111/j.1365-2966.2008.14180.x. arXiv: 0810.5558 [astro-ph].

Smith, Russell J. et al. (Nov. 2010). "Ultraviolet tails and trails in cluster galaxies: a sample of candidate gaseous stripping events in Coma". In: MNRAS 408.3, pp. 1417–1432. DOI: 10.1111/j.1365-2966.2010.17253.x. arXiv: 1006.4867 [astro-ph.CO].

Springel, Volker (Jan. 2010). "E pur si muove: Galilean-invariant cosmological hydrodynamical simulations on a moving mesh". In: MNRAS 401.2, pp. 791–851. DOI: 10.1111/j.1365-2966.2009.15715.x. arXiv: 0901.4107 [astro-ph.CO].

Springel, Volker et al. (Mar. 2018). "First results from the IllustrisTNG simulations: matter and galaxy clustering". In: MNRAS 475.1, pp. 676–698. DOI: 10.1093/mnras/stx3304. arXiv: 1707.03397 [astro-ph.GA].

Srivastav, S. et al. (Mar. 2022). "ePESSTO+ Transient Classification Report for 2022-03-09". In: *Transient Name Server Classification Report* 2022-667, p. 1.

Strateva, Iskra et al. (Oct. 2001). "Color Separation of Galaxy Types in the Sloan Digital Sky Survey Imaging Data". In: AJ 122.4, pp. 1861–1874. DOI: 10.1086/323301. arXiv: astro-ph/0107201 [astro-ph].

Sullivan, M. et al. (Sept. 2006). "Rates and Properties of Type Ia Supernovae as a Function of Mass and Star Formation in Their Host Galaxies". In: ApJ 648.2, pp. 868–883. DOI: 10.1086/506137. arXiv: astro-ph/0605455 [astro-ph].

Swinbank, A. M. et al. (Feb. 2012). "From star-forming spirals to passive spheroids: integral field spectroscopy of E+A galaxies". In: MNRAS 420.1, pp. 672–683. DOI: 10.1111/j.1365-2966.2011.20082.x. arXiv: 1110.5638 [astro-ph.CO].

Tabor, G. and J. Binney (July 1993). "Elliptical galaxy cooling flows without mass drop-out." In: MNRAS 263, pp. 323–334. DOI: 10.1093/mnras/263.2.323.

Tammann, G. A., W. Loeffler, and A. Schroeder (June 1994). "The Galactic Supernova Rate". In: ApJS 92, p. 487. DOI: 10.1086/192002.

Tasker, Elizabeth J. and Greg L. Bryan (Apr. 2006). "Simulating Star Formation and Feedback in Galactic Disk Models". In: ApJ 641.2, pp. 878–890. DOI: 10.1086/500567. arXiv: astro-ph/0512027 [astro-ph].

Terreran, G. (Sept. 2020). "Transient Classification Report for 2020-09-22". In: *Transient Name Server Classification Report* 2020-2902, p. 1.

Thomas, Daniel et al. (June 2010). "Environment and self-regulation in galaxy formation". In: MNRAS 404.4, pp. 1775–1789. DOI: 10.1111/j.1365-2966.2010.16427.x. arXiv: 0912.0259 [astro-ph.CO].

Tonry, J. L. et al. (June 2018). "ATLAS: A High-cadence All-sky Survey System". In: PASP 130.988, p. 064505. DOI: 10.1088/1538-3873/aabadf. arXiv: 1802.00879 [astro-ph.IM].

Toomre, A. (May 1964). "On the gravitational stability of a disk of stars." In: ApJ 139, pp. 1217–1238. DOI: 10.1086/147861.

Toomre, Alar and Juri Toomre (Dec. 1972). "Galactic Bridges and Tails". In: ApJ 178, pp. 623–666. DOI: 10.1086/151823.

Tremonti, Christy A. et al. (Oct. 2004). "The Origin of the Mass-Metallicity Relation: Insights from 53,000 Star-forming Galaxies in the Sloan Digital Sky Survey". In: ApJ 613.2, pp. 898–913. DOI: 10.1086/423264. arXiv: astro-ph/0405537 [astro-ph].

Tucker, Wallace and Laurence P. David (July 1997). "A Feedback Model for Radio Sources Fueled by Cooling Flows". In: ApJ 484.2, pp. 602–607. DOI: 10.1086/304345.

van den Bergh, S. (June 1976). "A new classification system for galaxies." In: ApJ 206, pp. 883–887. DOI: 10.1086/154452.

van den Bosch, Frank C. et al. (June 2008). "The importance of satellite quenching for the build-up of the red sequence of present-day galaxies". In: MNRAS 387.1, pp. 79–91. DOI: 10.1111/j.1365-2966.2008.13230.x. arXiv: 0710.3164 [astro-ph].

Veilleux, Sylvain, Gerald Cecil, and Joss Bland-Hawthorn (Sept. 2005). "Galactic Winds". In: ARA&A 43.1, pp. 769–826. DOI: 10.1146/annurev.astro.43.072103.150610. arXiv: astro-ph/0504435 [astro-ph].

Villalobos, Á. et al. (Aug. 2012). "Simulating the evolution of disc galaxies in a group environment - I. The influence of the global tidal field". In: MNRAS 424.4, pp. 2401–2428. DOI: 10.1111/j.1365-2966.2012.20667.x. arXiv: 1202.0550 [astro-ph.CO].

Villforth, C. et al. (Apr. 2014). "Morphologies of z $\sim$ 0.7 AGN host galaxies in CANDELS: no trend of merger incidence with AGN luminosity". In: MNRAS 439.4, pp. 3342–3356. DOI: 10.1093/mnras/stu173. arXiv: 1401.5477 [astro-ph.GA].

Vulcani, Benedetta et al. (Apr. 2020). "GASP XXIV. The History of Abruptly Quenched Galaxies in Clusters". In: ApJ 892.2, 146, p. 146. DOI: 10.3847/1538-4357/ab7bdd. arXiv: 2003.02274 [astro-ph.GA].

Ward, Charlotte et al. (Sept. 2022). "Variability-selected Intermediate-mass Black Hole Candidates in Dwarf Galaxies from ZTF and WISE". In: ApJ 936.2, 104, p. 104. DOI: 10.3847/1538-4357/ac8666. arXiv: 2110.13098 [astro-ph.GA].

Weigel, Anna K. et al. (Aug. 2017). "Galaxy Zoo: Major Galaxy Mergers Are Not a Significant Quenching Pathway". In: ApJ 845.2, 145, p. 145. DOI: 10.3847/1538-4357/aa8097. arXiv: 1708.00866 [astro-ph.GA].

Weil, K. E., B. M. Subrayan, and D. Milisavljevic (July 2021). "REFITT Transient Classification Report for 2021-07-01". In: *Transient Name Server Classification Report* 2021-2270, pp. 1–2270.

Wetzel, Andrew R., Jeremy L. Tinker, and Charlie Conroy (July 2012). "Galaxy evolution in groups and clusters: star formation rates, red sequence fractions and the persistent bimodality". In: MNRAS 424.1, pp. 232–243. DOI: 10.1111/j.1365-2966.2012.21188.x. arXiv: 1107.5311 [astro-ph.CO].

Wetzel, Andrew R. et al. (June 2013). "Galaxy evolution in groups and clusters: satellite star formation histories and quenching time-scales in a hierarchical Universe". In: MNRAS 432.1, pp. 336–358. DOI: 10.1093/mnras/stt469. arXiv: 1206.3571 [astro-ph.CO].

Whitmore, Bradley C., Diane M. Gilmore, and Christine Jones (Apr. 1993). "What Determines the Morphological Fractions in Clusters of Galaxies?" In: ApJ 407, p. 489. DOI: 10.1086/172531.

Wiseman, P. et al. (Sept. 2021). "Rates and delay times of Type Ia supernovae in the Dark Energy Survey". In: MNRAS 506.3, pp. 3330–3348. DOI: 10.1093/mnras/stab1943. arXiv: 2105.11954 [astro-ph.GA].

Woosley, S. E. (Aug. 2010). "Bright Supernovae from Magnetar Birth". In: ApJ 719.2, pp. L204–L207. DOI: 10.1088/2041-8205/719/2/L204. arXiv: 0911.0698 [astro-ph.HE].

Woosley, S. E. and J. S. Bloom (Sept. 2006). "The Supernova Gamma-Ray Burst Connection". In: ARA&A 44.1, pp. 507–556. DOI: 10.1146/annurev.astro.43.072103.150558. arXiv: astro-ph/0609142 [astro-ph].

Yan, L. et al. (June 2020a). "ZTF Transient Classification Report for 2020-06-09". In: *Transient Name Server Classification Report* 2020-1737, p. 1.

Yan, L. et al. (June 2020b). "ZTF Transient Classification Report for 2020-06-09". In: *Transient Name Server Classification Report* 2020-1736, p. 1.

Yang, Xiaohu et al. (Dec. 2007). "Galaxy Groups in the SDSS DR4. I. The Catalog and Basic Properties". In: ApJ 671.1, pp. 153–170. DOI: 10.1086/522027. arXiv: 0707.4640 [astro-ph].

Yao, Y. et al. (May 2021). "Transient Classification Report for 2021-05-13". In: *Transient Name Server Classification Report* 2021-1614, pp. 1–1614.

Yesuf, Hassen M. et al. (Sept. 2014). "From Starburst to Quiescence: Testing Active Galactic Nucleus feedback in Rapidly Quenching Post-starburst Galaxies". In: ApJ 792.2, 84, p. 84. DOI: 10.1088/0004-637X/792/2/84. arXiv: 1407.3834 [astro-ph.GA].

Zabludoff, Ann I. et al. (July 1996). "The Environment of "E+A" Galaxies". In: ApJ 466, p. 104. DOI: 10.1086/177495. arXiv: astro-ph/9512058 [astro-ph].

Zibecchi, L. et al. (Oct. 2020). "Microvariability in AGNs: study of different statistical methods - II. Light curves from simulated images". In: MNRAS 498.2, pp. 3013–3022. DOI: 10.1093/mnras/staa2544. arXiv: 2008.08137 [astro-ph.GA].

Ziparo, F. et al. (Jan. 2014). "Reversal or no reversal: the evolution of the star formation rate-density relation up to z ~ 1.6". In: MNRAS 437.1, pp. 458–474. DOI: 10.1093/mnras/stt1901. arXiv: 1310.1398 [astro-ph.CO].

Zurita, A. et al. (Jan. 2004). "Ionized gas kinematics and massive star formation in NGC 1530". In: A&A 413, pp. 73–89. DOI: 10.1051/0004-6361:20031049. arXiv: astro-ph/0307234 [astro-ph].